CHAPTER 3

Synthesis, Characterization and Structural assessment of biologically active square pyramidal Cu(II) acylpyrazolone complexes: DFT, Hirshfeld analysis

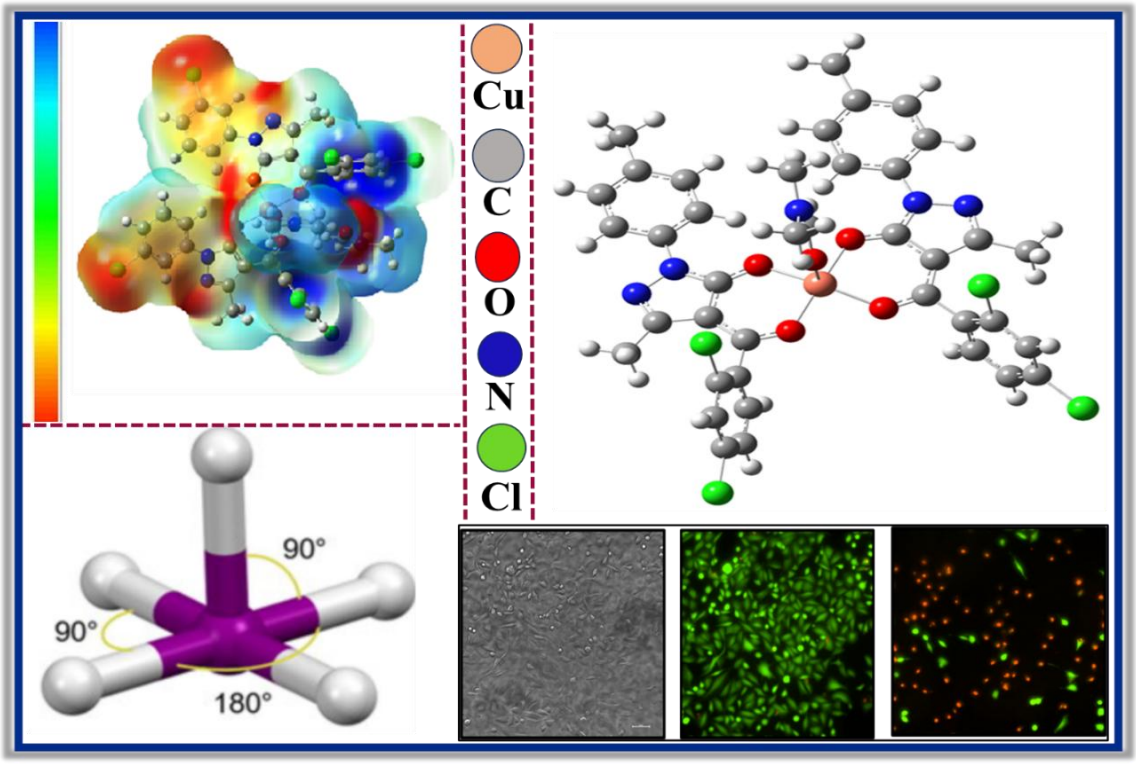

Chapter 3: Part (a)

Square pyramidal Cu(II) acylpyrazolone complexes: Synthesis, characterization, crystal structure, DFT and Hirshfeld analysis; *in-vitro* anti-cancer evaluation

3a.1 Introduction

The transition elements, also known as the d-block elements, take up most of the central space of the periodic table and are commonly utilized. Among various disciplines, bioinorganic chemistry, materials science and catalysis continue to be at the cutting edge of research [1]. Metals possess many distinctive qualities, such as Redox property, different manners of coordination, and responsiveness to organic substrates. Because of such properties and reactivity, metals are subjected to strict regulation in optimal conditions. Abnormal levels of metal ions are linked to several pathological illnesses, including cancer. Diseases including pernicious anaemia, growth retardation, and heart disease all occur from the lack of iron, zinc and copper metal ions. Transition metals exhibit a range of oxidation states and interact with negatively charged molecules. Transition metals having such characteristics encouraged the emergence of metal-based drugs with potential pharmacological applications. Metal complexes can now be used as medicinal agents efficiently owing to developments in inorganic chemistry [2].

Chemotherapy is a systemic cancer treatment recommended to patients—the discovery of platinum-based drugs that inhibit tumour cell proliferation as an anti-cancer agent. The clinical applications of cisplatin and its derivative drugs are used worldwide. The use of platinum derivatives can be limited due to harmful side effects such as liver, kidney, heart, and immune system toxicity, haemorrhage, and gastrointestinal problems. Transition metal copper-based complex is very favourable and very advantageous [3].

Cell migration fundamentally shapes and maintains the organization of multicellular organisms, whereas abnormal cell migration is seen in many clinical diseases such as cancer. Lung cancer is one of the leading causes of death worldwide. Individual cells and cell clusters can migrate from one place to another during cell migration. The most common technique for evaluating cell migration is the scratch or wound healing assay [4]. Pyrazolone is found in many active chemicals as a significant structural motif. Considering their diverse spectrum of biological actions, pyrazolone derivatives serve a special role in drug discovery [5]. Making physiologically relevant transition metal complexes is a key objective of this study. It is well known that the biological potency of the ligand is increased by the formation of the complexes [6]. 4-acyl-pyrazolone, a pyrazolone derivative, can develop a variety of coordination compounds because of the keto-enol tautomerism and multiple electron-rich donor centres [7]. Ligand selection during the synthesis and design of drug molecules has always become an important tool. Density functional theory (DFT), in addition to

experimental characterization, is a unique and innovative method for understanding the various chemical characteristics that arise in metal-ligand complexes [8].

We selected the biocompatible metal ion Cu from the group of metal ions because of its significance in biological living systems. Copper compounds exhibit a transition between copper(II) and copper(I) ions, which can generate superoxide and hydroxyl radicals and cause cell death; they are potentially cytotoxic [9]. This study looks into the spectroscopic, ESR, redox behaviour, X-ray single crystal and some characteristics of square pyramidal Cu^{2+} complexes. Cell death analysis of synthesized compounds was performed. *In vitro,* anti-cancer activity was done using hepatocellular carcinoma cell line (HepG2) for liver cancer, lung carcinoma cell line (NCI-H23) for lung cancer and SH-SY5Y cell line for neuroblastoma cancer which is found in infants and young children. Moreover, we compared the NCI-H23 and SH-SY5Y cancer cell proliferation inhibition by cisplatin, complex-**1** and complex-**2.**

3a.2 Experimental work

3a.2.1 Materials and Methods

The starting materials, pyrazolone and acyl chloride, were purchased from Sidhdhanath Industries, Sachin (Surat), India and Shiva Pharmachem Limited, Vadodara (Gujarat), India, respectively. AR-grade solvents were purchased from CDH − Central Drug House (P) Ltd. Copper salts were sourced from Sigma Aldrich Chemical Co. Pvt. Ltd. MTT and FBS were purchased from Himedia, India and Gibco, USA, respectively. The cytotoxicity kit was obtained from Invitrogen, USA. Lung adenocarcinoma (NCI-H23), hepatocellular carcinoma (HepG2) and neuroblastoma (SH-SY5Y) cancer cells were procured from the National Centre for Cell Science (NCCS), Pune. Cisplatin was acquired from Sigma-Aldrich. Calcein dye and Ethidium homodimer dye EthD-1) were purchased from Thermo Fisher Scientific (Applied Biosystems). These materials were crucial for the effective completion of the experiments and were obtained in alignment with the prescribed procurement guidelines. All the chemicals used in this study were purified using standard methods [10]. The synthesis and characterization of the Ligands HL^{II} and HL^{IX} were performed following the procedures outlined in Chapter **2**. A HL^{IX} ligand was synthesized, characterized and published in our laboratory's recent publication [11].

3a.2.2 Synthetic route of complex-1 and complex-2

The hot methanolic solutions of the HL^{II} ligand (0.762 g, 0.002 mol) and HL^{IX} ligand (0.646 g, 0.002 mol) were prepared in two different round-bottom flasks (RBF), each

equipped with a water condenser in a closed system. After getting clear solutions in both the RBFs, $CuSO_4.5H_2O$ (Copper sulphate pentahydrate) metal salt (0.249 g, 0.001 mol) was dissolved in 10 mL of methanol solvent and then gradually added to the ligand solutions. The resultant mixtures of RBFs were then subjected to reflux at a temperature of 70-80°C for 3-4 hours, forming green-coloured precipitates of two copper complexes (complex-**1** and complex-**2**). Both products were washed with hot methanol, dried and recrystallized from hot DMF and DMSO solvents, respectively. Thick green plate-shaped X-ray quality single crystals of complex-**1** and complex-**2** were obtained after a few days. Both complexes are stable at room temperature. As confirmed by single-crystal X-ray analysis, DMF and DMSO solvents occupy the apical position (**5th** coordination site) in complex-**1** and complex-**2**, respectively. The synthetic route of complex-**1** and complex-**2** are demonstrated in **Fig.3a.1**. The physical appearances of both complexes are pictured in **Fig.3a.2.**

Complex-1: **Colour**: Green, yield: 82%, M.P:> 200°C, Molecular formula: $C_{34}H_{20}CuCl_6N_4O_4$.DMF, **Crystal:** Thick green plate, **M.W:** 824.811, **Elemental analysis**: C (Exp. 53.10%, Calc.: 52.69%); H (Exp. 2.90%, Calc. 2.80%); N (Exp. 8.21%, Calc. 7.21%); Cu (Exp. 8.10%, Calc. 7.08%), **FTIR (KBr, cm^{-1}):** ν(C=O) of pyrazolone: (1606), ν(C=O) of 2,4-dichloro benzoyl chloride: (1512), cyclic ν(C=N): (1473).

Complex-2: **Colour**: Green, yield: 83%, M.P.: >200°C, Molecular formula: $C_{34}H_{24}CuN_6O_8$.DMSO, **Crystal:** Thick green plate, **M.W:** 708.136, **Elemental analysis**: C (Exp. 56.55%, Calc. 55.53%); H (Exp. 4.50%, Calc. 4.03%); N (Exp. 10.80%, Calc. 10.50%); S (Exp. 2.80%, Calc. 2.77%); Cu (Exp. 8.05%, Calc. 7.94 %), **FTIR(KBr, cm^{-1}):** ν(C=O) of pyrazolone: (1604), ν(C=O) of of 4-nitro benzoyl chloride: (1567), cyclic ν(C=N):1380.

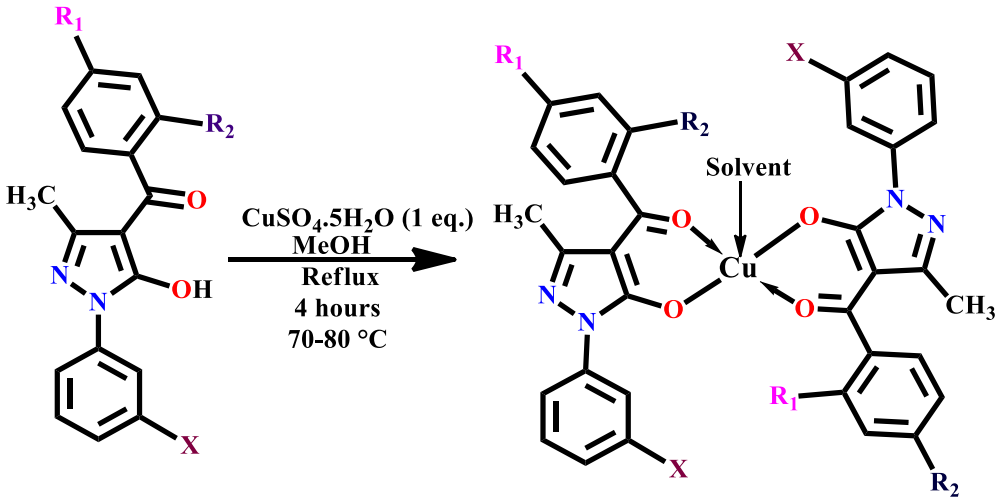

Complex-1: R_1= Cl, R_2= Cl, X= Cl

Complex-2: R_1= NO_2, R_2= H, X = H

Fig.3a.1. Synthetic route of complex-1 and complex-2

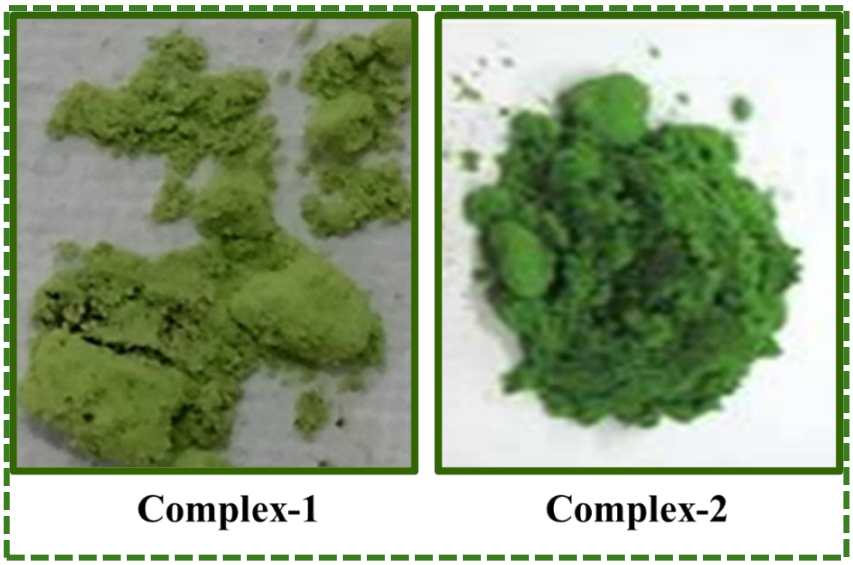

Fig.3a.2. Physical appearance of complex-1 and complex-2

3a.2.3 X-ray crystallographic study

The X-ray crystal structures of both complexes were determined using graphite-monochromatized Cu—Kα radiation (λ= 1.54178 Å). Complex-**1** and complex-**2** were recrystallized from hot DMF and DMSO solvents, yielding thick green plate-shaped single crystals. Data were collected on a Bruker APEX-II CCD diffractometer at 298(2) K and 293(2) K for complex-**1** and complex-**2**, respectively. Both structures were solved using SHELXT (G.M. Sheldrick) and refined with the SHELXL-2018/3 program [12][13]. Mercury software was employed for the ORTEP views of all three complexes [14].

3a.2.4 Physical measurements and Characteization

Both the synthesized complexes have been examined through analytical and spectroscopic techniques, including FTIR, UV-Vis spectroscopy, thermogravimetric analysis (TG-DTA), cyclic voltammetry (CV) and electron spin resonance (ESR). Elemental analysis was performed through Elemetar Analysensysteme GmbH, Germany, Unicube make. The infrared spectra (4000–400 cm^{-1}) were recorded using a Bruker Alpha instrument with KBr discs. In DMSO solvent, the electronic spectra of both complexes were recorded at 250-900 nm range using UV-Vis spectrophotometer model V-730. Simultaneous TG-DTA analysis was performed using the SII-EXSTAR6000 TG-DTA 6300 system. The experiments were

carried out under a nitrogen atmosphere, with a heating rate of 10 °C/min, over a temperature range of 30–550 °C. The magnetic property complex-**1** was examined through ESR JEOL analysis in a powder state at RT with tetracyanoethylene (TCNE) as a marker (g = 2.00277) at SAIF IIT Mumbai. The CV analysis of complex-**1** and complex-**2** was conducted with a CHI608E instrument at CSIR-CSMCRI, Bhavnagar. Molar conductivity was measured at room temperature in a 10^{-3} M DMF solution using an EQ-664A conductivity meter. Finally, copper content in the complexes was determined gravimetrically and volumetrically after sample decomposition with HNO_3.

3a.2.5 Computational analysis

Density Functional Theory (DFT) was employed for full geometry optimization of both complexes. B3LYP/6-31G level basis set was utlillized for the geometry optimization of complex-**1** [15][16] and B3LYP/LANL2DZ basis set was used for complex-**2** [17][18]**.** HOMO–LUMO energies were calculated and visualized with Gauss View 6.0, a molecular visualization software. This basis set simplifies the treatment of core electrons using effective core potentials (ECPs), which is particularly beneficial for transition metals and heavier elements like copper. Natural Bond Orbital (NBO) analysis was performed to investigate the interactions between occupied and unoccupied Lewis-type NBO orbitals. The MESP and spin density plots were created to analyze the electron distribution in the α and β spin states. The frontier orbital analysis and HOMO-LUMO energy gap were calculated using the same basis set.

3a.2.6 *In vitro* anti-cancer activity

The antiproliferative properties (*in vitro* anti-cancer activity) of both complexes have been analyzed via MTT assay [19]. The *in vitro* assessment of anti-cancer activity is an essential initial phase in the drug discovery process. This approach involves evaluating compounds on cancer cells grown in culture, outside of a living organism, to determine their effectiveness in reducing cell growth or disrupting key molecular pathways that drive cancer progression. In this analysis, three different cancer cell lines were used. Complex-**1** was tested against three cancer cell lines: NCI-H23 (lung adenocarcinoma), HepG2 (hepatocellular carcinoma), and SH-SY5Y (neuroblastoma). Among these, complex-**1** exhibited the most effective activity against the NCI-H23 lung cancer cell line, leading to further studies on this cell line. A ‘live-dead assay’ was conducted using complex-**1** to analyze the number of live and dead cells. A' scratch assay' was performed to assess cell migration and growth, which are important factors in cancer metastasis [20]. Complex-**2** was tested against SH-SY5Y (neuroblastoma) cancer cells. Cisplatin was taken as a reference

compound for the above analysis. A comparative study of complex-**1** and complex-**2** against cisplatin was also conducted.

3a.2.6.1 Cell culture conditions

NCI-H23 (Lung adenocarcinoma), HepG2 (Hepatocellular carcinoma) and SH-SY5Y (Neuroblastoma) cancer cell lines were procured from the National Centre for Cell Science (NCCS), Pune. NCI-H23 lung cancer cells were cultured in the RPMI-1640 medium (Himedia). In contrast, HepG2 and SH-SY5Y cells were cultured in MEM medium supplemented with 10% fetal bovine serum and 1% penicillin-streptomycin solution (Gibco) at 37 °C in 5% CO_2 condition.

3a.2.6.2 MTT- Cell viability assay

Cell viability was evaluated using the MTT assay. Cells were cultured in 96-well plates (ThermoFisher Scientific) for 24 hours in a cell culture medium at 7,000 cells per well for adhesion. The seeded cells were treated with various concentrations of complex-**1** and complex-**2** for 24 hours at 37 °C in a 5% CO_2 incubator [21][19]. NCI-H23 cells were also treated with cisplatin at various concentrations for 24 hours. After incubation, the media were removed, and the cells were washed with PBS. MTT (0.5 mg/mL) was added to each well, and the plates were incubated at 37 °C with 5% CO_2 for 4 hours. The resulting formazan crystals were dissolved in 100 µL of DMSO. Absorbance was measured using an ELISA plate reader (iMark, Bio-Rad, USA) at 540 and 660 nm. The IC_{50} was determined using GraphPad Prism 6 software. Images were taken using an inverted microscope (Olympus EK2) and a 10 MP Aptima CMOS digital camera (AmScope). The percentage of cell viability was calculated using the following formula **(1):**

% Cell viability = (OD of treatment / OD of control) × 100 **(1)**

3a.2.6.3 Live/Dead assay

A Live/Dead assay is frequently employed to assess the cytotoxic impact of anti-cancer agents by differentiating between living (viable) and non-living (non-viable) cells. This assay offers a rapid and efficient method to evaluate the effectiveness of anti-cancer treatments by measuring the proportion of feasible versus dead cells. It is a cell staining procedure in which cells are stained with specific dyes, such as **'calcein** and **Ethidium homodimer'**. As explained in Section **3a.2.6**, complex-**1** was used for this analysis on the NCI-H23 cell line. For this analysis, 25×10^3 cells were seeded per well in 8-well chamber slides (ThermoFisher Scientific) and incubated for 24 hours. The cells were then treated with a copper complex for 24 hours. After the treatment, the cells were stained with a cytotoxicity

kit (Invitrogen), using 2 mM calcein dye and 4 mM Ethidium homodimer dye (EthD-1), for 30 minutes following the manufacturer's protocol. Photographs were taken using a fluorescence microscope (Nikon-Ti2E). The percentage of dead cells was calculated using ImageJ software [22].

3a.2.6.4 Scratch assay/wound healing assay

The scratch (or wound healing) assay is valuable for studying cell migration. To measure migration, a monolayer of cells was grown to 100% confluence in a 6-well culture plate. A scratch was created using a 200 µL pipette tip, and the cells were then treated with the synthesized copper complex. Photographs of the scratch were taken at 0 hours, 24 hours, and 48 hours. Wound closure (%) was calculated using ImageJ software [4][20].

3a.3 Results and Discussion

A general method was used to synthesize two square-pyramidal Cu(II) acyl pyrazolone complexes **1** & **2**. The stability of both complexes was observed at room temperature. The complexes were characterized by FT-IR, UV–Vis, CV, ESR, TGA and X-ray crystallography techniques. Elemental analysis and molar conductance measurements were also carried out. Geometry optimization was performed using Density Functional Theory (DFT). Hirshfeld surface analysis was utilized to investigate intermolecular interactions and crystal packing in solid-state structures. Both complexes are soluble in methanol (MeOH), ethanol (EtOH), dimethylformamide (DMF), and dimethyl sulfoxide (DMSO). Copper acylpyrazolone complexes exhibit potent anti-cancer effects by suppressing cancer cell proliferation and promoting apoptosis. Their activity is linked to interactions with cellular components and the generation of reactive oxygen species, which interfere with critical processes in cancer cells. Therefore, the *in vitro* anticancer activity of complex-**1** and complex-**2** was evaluated using three different cancer cell lines: 'NCI-H23 (lung cancer), HePG2 (Liver cancer) and SH-SY5Y (neuroblastoma)'. The IC_{50} (half maximal inhibitory concentration) of both complexes has been determined. Live-dead and wound-healing assays were performed against NCI-H23 (lung adenocarcinoma cells) using complex-**1**. Crystal structures and other characteristics of complex-**1** and complex-**2** are displayed below.

3a.3.1 FTIR spectral studies

Fourier Transform Infrared Spectroscopy (FTIR) is a vital analytical method that identifies and characterizes chemical compounds by examining their molecular vibrations. The FTIR analysis reveals critical information about the compound's functional groups and

molecular structures by analyzing how a sample absorbs infrared light. The IR absorption bands for the ν(C=O) group in benzoyl chloride and pyrazolone are observed at 1524 cm^{-1} and 1591 cm^{-1}, respectively, in complex-**1**. In contrast, complex-**2** shows the ν(C=O) frequencies for benzoyl chloride and pyrazolone at 1567 cm^{-1} and 1604 cm^{-1}, respectively. The formation of the metal complex results in a notable shift in IR frequencies attributed to establishing the M-O bond. During the complexation process, electron density from the oxygen atom of the C=O group in pyrazolone is transferred to the metal ion, which enhances the strength of the M-O bond while weakening the C=O bond. This interaction ultimately increases the bond length of the C=O bond (lower IR frequencies) in the complex as compared to free ligand [23][7]. Additional FTIR frequencies are detailed in the table below, while **Table 3a.1** presents the FTIR frequencies for complexes **1** and **2**. **Figs. 3a.3-3a.4** display the FTIR spectra of these complexes.

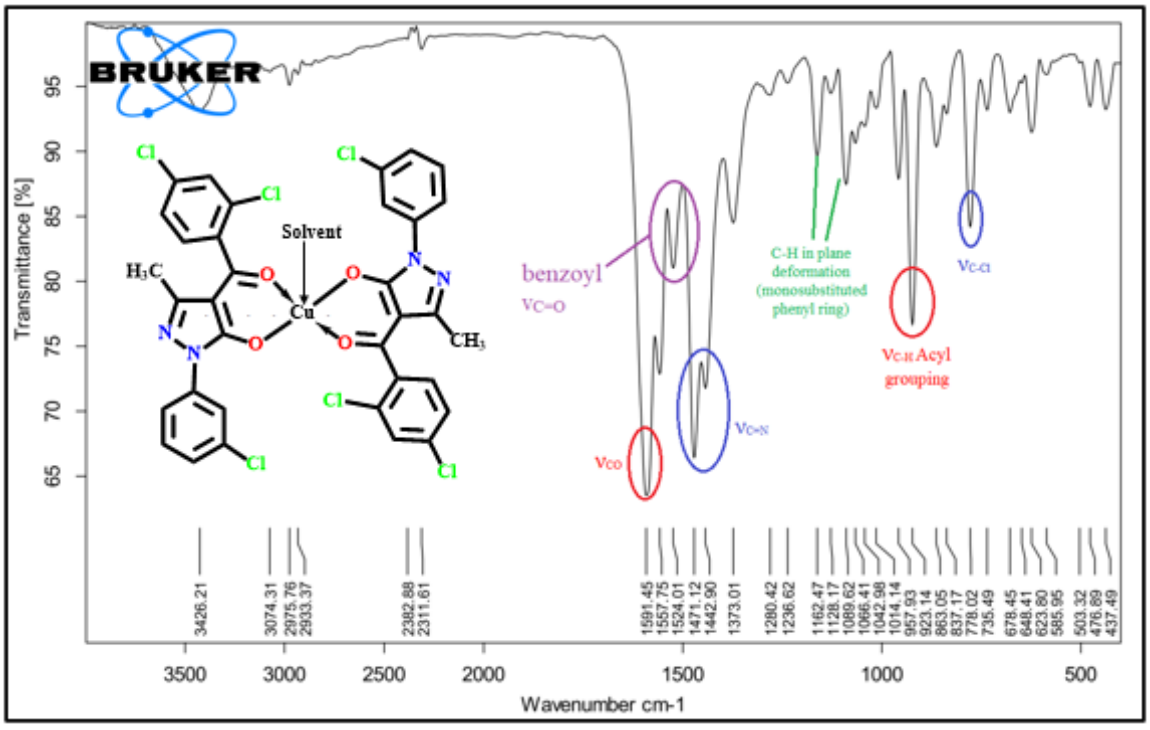

Fig.3a.3. FTIR spectrum of complex-1

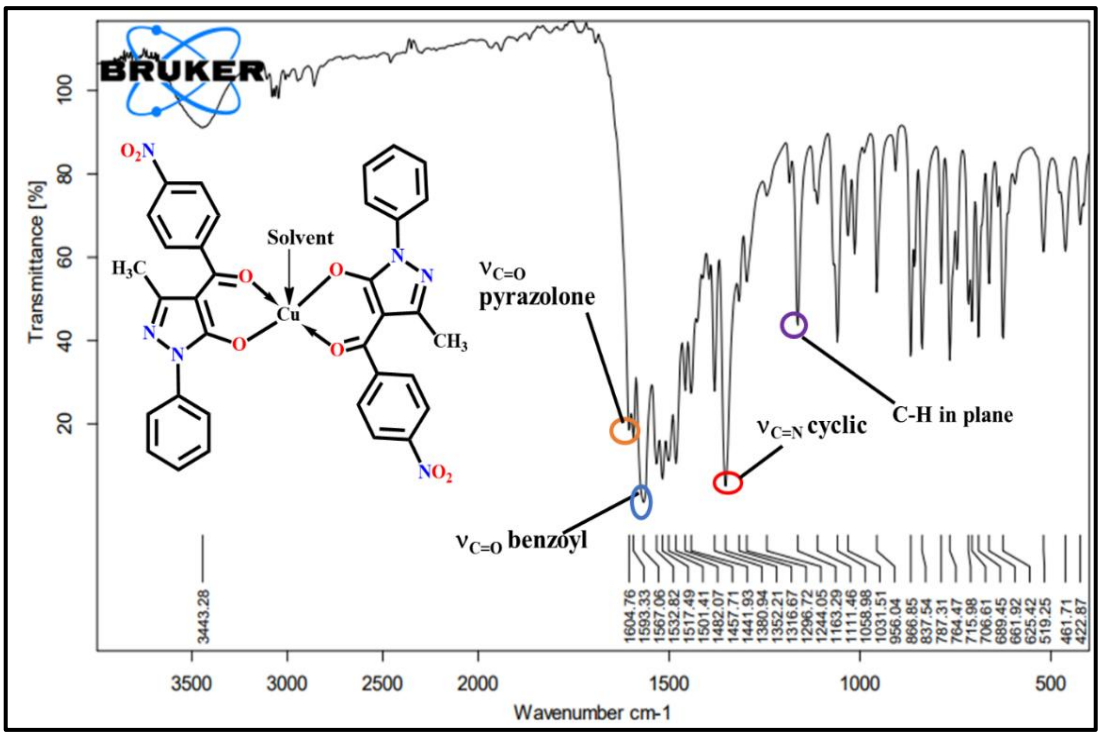

Fig.3a.4. FTIR spectrum of complex-2

Table 3a.1. FTIR spectral data of ligands, complexes 1 and 2

Code	HL^{II} ligand	Complex-1	HL^{IX} ligand	Complex-2
ν(C=O) of benzoyl chloride	1550	1524	1519	1567
ν(C=O) of Pyrazolone	1594	1591	1622	1604
Cyclic ν(C=N)	1482	1471	1393	1380
C–H in-plane deformation	1062	1162	1210	1244

3a.3.2 Molar conductivity measurements

The molar conductivity measurements of both complexes were measured in a 10^{-3} M DMF solution. Molar conductivity Λ^{o}_{M} values for complex-**1** and complex-**2** were found to be 2.18 $ohm^{-1}cm^{2}mol^{-1}$ and 3.90 $ohm^{-1}cm^{2}mol^{-1,}$ respectively. Such lower molar conductivity values suggest the non-electrolytic behaviour of both complexes and an absence of charged species in the coordination sphere [24]**.**

3a.3.3 Thermogravimetric analysis

Thermogravimetric analysis (TGA) provides insight into a material's mass change as a temperature function. The mass loss and thermal stability of the material were evaluated using TGA. The three-step decomposition of the five-coordinated complexes (complex-**1** and complex-**2**) was examined through this analysis. The copper complexes decompose thermally between 100°C and 550°C, demonstrating remarkable thermal stability for both complexes. In complex-**1**, the first decomposition of the ligand moiety occurs up to 280°C,

with a 3.4% mass loss. A significant change of 1.094 mg/min at 317.3°C was recorded in the DTG curve. Complete degradation of both ligands is observed between 280°C and 500°C. At 338.9°C, a shift of 1.054 mg/min is observed in the DTG curve. Up to 550°C, the final product, copper oxide (CuO), remains stable. In complex-**2**, a total weight loss of 57.8% is shown in the TG graph (blue spectrum), occurring in two stages: (i) a 43.5% weight loss and (ii) a 14.3% weight loss, primarily due to the loss of two ligands between 300°C and 380°C. The green and red spectra represent the DTA and DTG graphs, respectively. A significant reduction of 0.160 mg/min was observed at 340.7°C in the DTG curve. The remaining CuO residue remains stable up to 550°C. TG-DTA plots of complex-**1** and complex-**2** are shown in **Fig.3a.5-3a.6.**

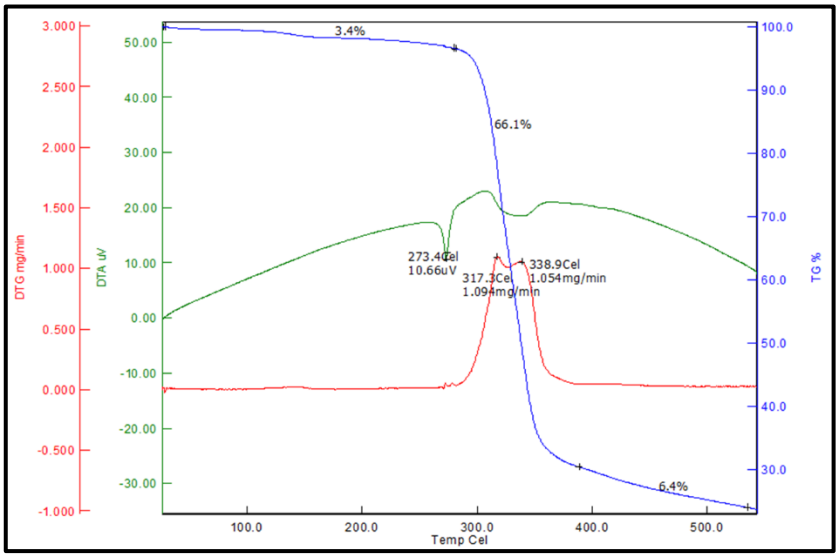

Fig.3a.5. TG-DTA plot of complex-1

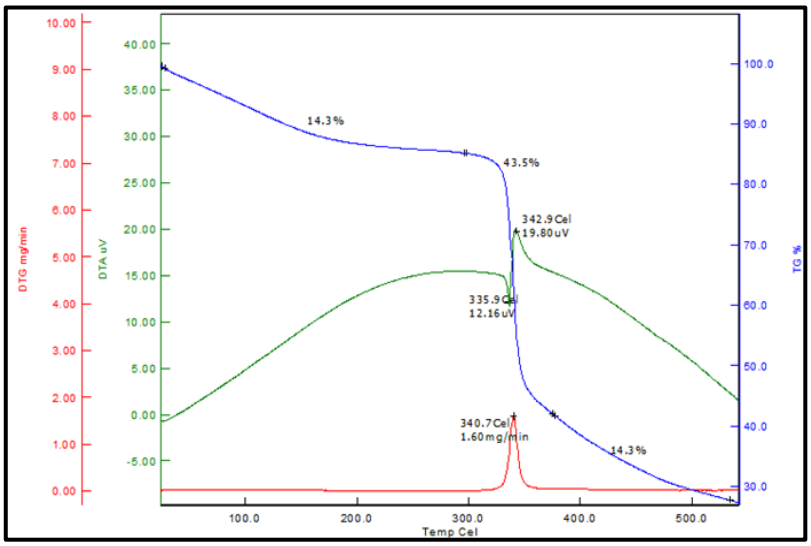

Fig.3a.6. TG-DTA plot of complex-2

3a.3.4 Electronic spectral analysis

The beneficial method, UV-visible absorption spectroscopy, has been extensively investigated to provide the structural information of a compound [8]. To determine the energy gap of the compounds, the crystal samples were analyzed using UV-visible absorption spectroscopy up to 950 nm (10526 cm^{-1}). In a DMSO solution, the electronic spectra were recorded. A complex-**1** exhibited a sharp transition at 277 nm (36101cm^{-1}), whereas a complex-**2** exhibited n-π* transitions at 363 nm (27548 cm^{-1}) and π-π* transitions at 280 nm (35714 cm^{-1}) within the ultraviolet range due to intra-ligand charge transfer (ILCT) transitions. The broad bands are also observed at 800 nm (12500 cm^{-1}) and 768 nm (13020 cm^{-1}) in complex-**1** and complex-**2**, respectively. In the visible spectrum is attributed to a d-d transition. These transitions can be assigned to the $d_{x^2-y^2} \rightarrow d_{xz}$, d_{yz} or $d_{x^2-y^2} \rightarrow d_{z^2}$ transitions [25]. which are indicative of Jahn-Teller distortion in these complexes [26][27][28]. **Figs.3a.7-3a.8** illustrates the UV-Vis spectrum of both complexes.

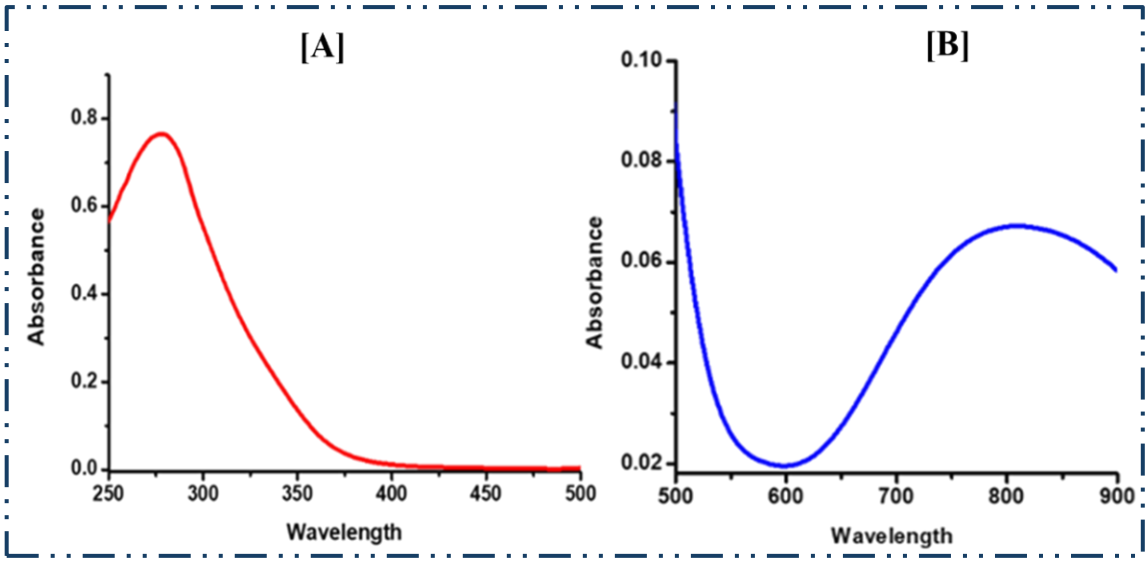

Fig.3a.7. Complex-1: [A] Intra-ligand charge transfer in a diluted solution of DMSO and [B] d-d transition in a $1x10^{-3}$ M solution of DMSO

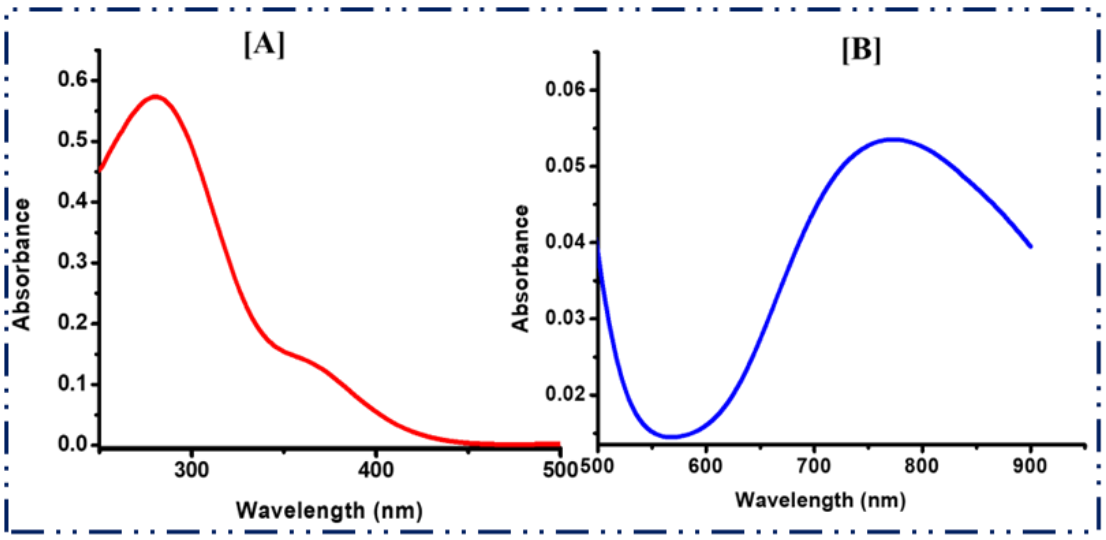

Fig.3a.8. Complex-2: [A] Intra-ligand charge transfer in a diluted solution of DMSO and [B] d-d transition in a $1x10^{-3}$ M solution of DMSO

3a.3.5 Single crystal X-ray diffraction analysis

The molecular crystal structure of both copper complexes appeared as green-coloured, thick, plate-shaped crystals. The geometry of both complexes is square pyramidal (penta-coordinated), where four oxygen atoms [O(1), O(2), O(3), O(4)] from the ligands occupy the equatorial positions, and the O(5) atom from the DMF or DMSO solvent occupies the apical position. Complex-**1** crystallizes in the '**Triclinic crystal system**' with the ***P*-1** space group and contains only an inversion centre as its symmetry element. It has a primitive lattice and no rotational symmetry, making it one of the simplest space groups for describing crystal structures. While complex-**2** has a '**Monoclinic crystal system**' with the $P2_{1/c}$ space group. This space group features a primitive lattice, a 2-fold screw axis along the b-axis and a c-glide plane. These symmetry elements shape the packing and arrangement of molecules in the crystal. In complex-**1**, the four donor oxygen atoms at the equatorial positions have bond lengths of 1.93(2) Å, 1.96(2) Å, 1.93(2) Å, and 1.97(2) Å for Cu-O1, Cu-O2, Cu-O3, and Cu-O4, respectively. In complex-**2**, these bond lengths are 1.94(3) Å, 1.95(3) Å, 1.93(3) Å, and 1.95(3) Å for Cu-O1, Cu-O2, Cu-O3, and Cu-O4. The apical position is occupied by an oxygen atom from a solvent molecule: DMF (O_5 atom) in complex-**1** and DMSO (O5 atom) in complex-**2**. The Cu-O5 bond lengths are 2.31(2) Å in complex-**1** and 2.27(5) Å in complex-**2.** The coordination geometry around the copper centres is best described as square pyramidal, with a **τ** (tau) value ranging from **0.15 to 0.3**, based on the equatorial and axial bond angles of the complexes [29]. In the context of Jahn-Teller distortion, the elongation of the apical bond lengths (2.31 Å and 2.27 Å for Cu-O5) in comparison to the equatorial bonds

points to a z-out distortion. This elongation occurs along the z-axis, which relieves electronic strain in both complexes. The shorter equatorial bond lengths, ranging from 1.93 Å to 1.97 Å, indicate stronger equatorial bonds. This difference arises because the $d_{x^2-y^2}$ orbital is more destabilized, while the dz^2 orbital becomes stabilized due to the longer apical bonds. Therefore, the extended apical Cu-O_5 bond lengths relative to the equatorial ones are characteristic of this z-out Jahn-Teller effect. In complex-**1**, a HL^{II} ligand coordinates the Cu(II) metal with chelating angles of 94.1(8)° and 93.6(8)° and in complex-**2** a HL^{IX} ligand coordinates the Cu(II) metal with chelating angles of 93.90(12)°-94.30(12)° with pyrazolone oxygens. The thermal ellipsoid plot (ORTAP diagram) and perspective view of the packing configuration of complex-**1** are demonstrated in **Fig.3a.9.** While **Fig.3a.10** shows the thermal ellipsoid plot (ORTAP diagram) and perspective view of the packing configuration of complex-**2.** The symmetry elements of both complexes are depicted in **Fig.3a.11.** A 2D representation of the single crystal structures of both complexes is shown in **Fig.3a.12.** The graphical illustration of C–O···π and off-set π···π stacking interactions are shown in **Fig.3a.13.** Bond lengths and bond angles parameters and symmetry transformations of complex-**1** are listed in **Tables 3a.2-3a.3,** respectively. Similar data for complex-**2** are provided in **Table 3a.4-3a.5**, respectively. All the refinement parameters and crystal data of both complexes are listed in **Table 3a.6.**

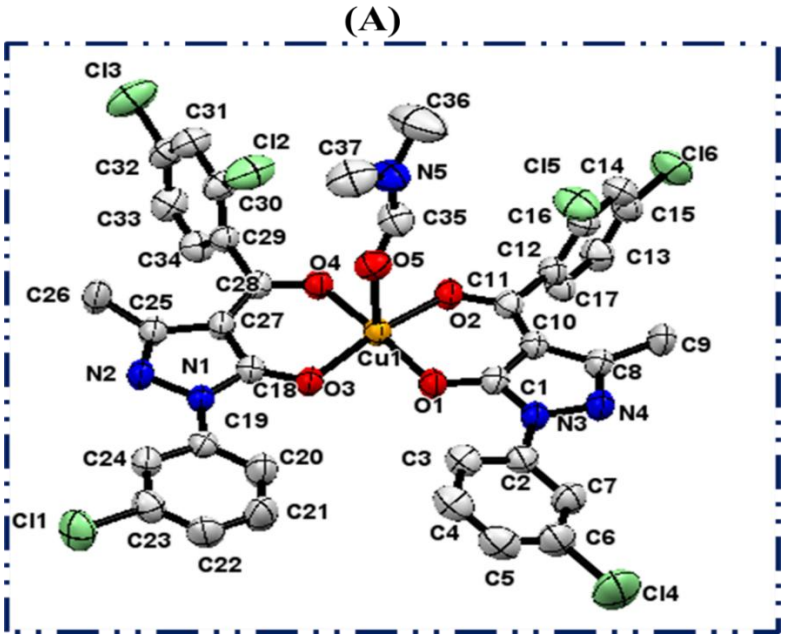

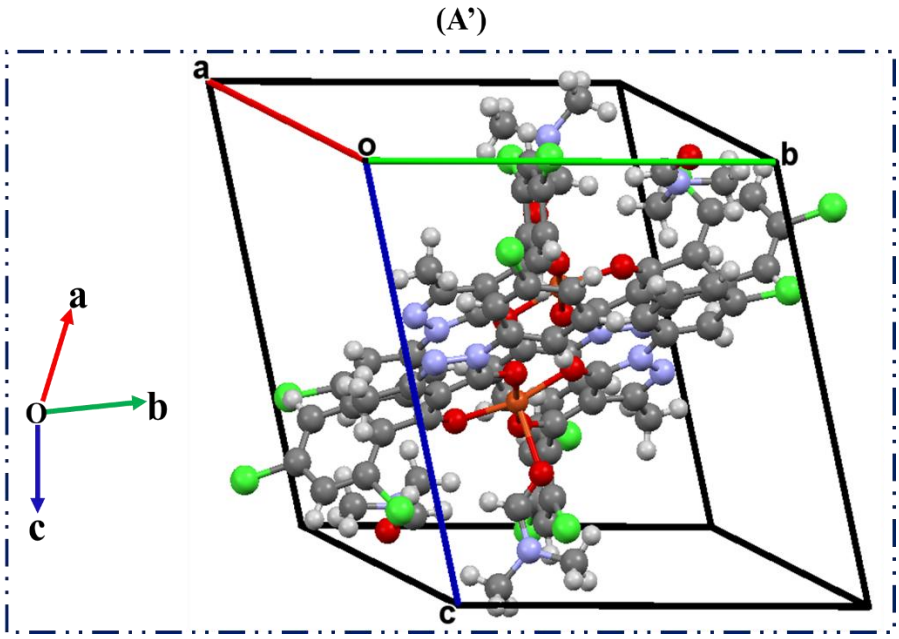

Fig.3a.9. Complex-1: (A)= Thermal ellipsoid plot with 50% probability of complex-1 (Hydrogen atoms omitted for clarity) and (A')= A perspective view of crystal packing plot of complex-1 along a-axis

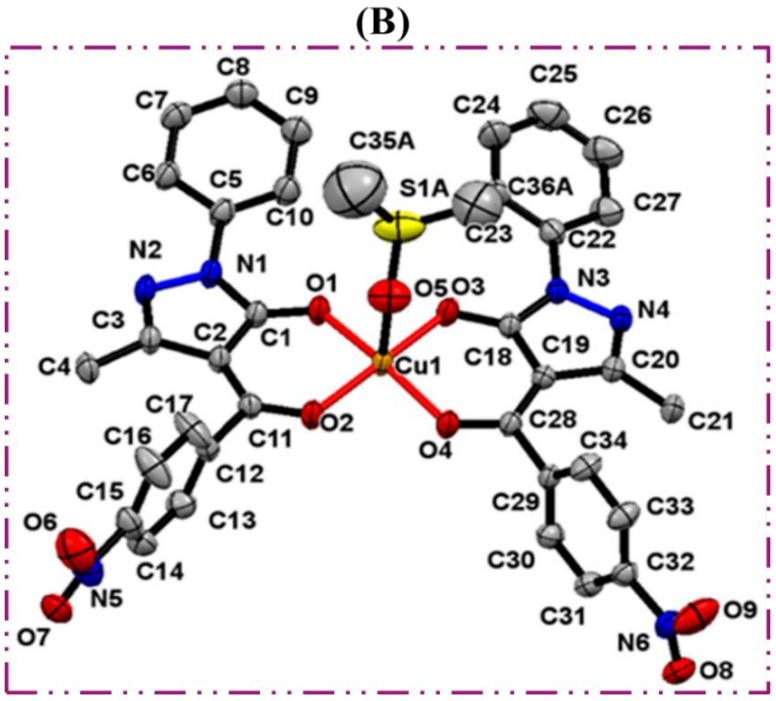

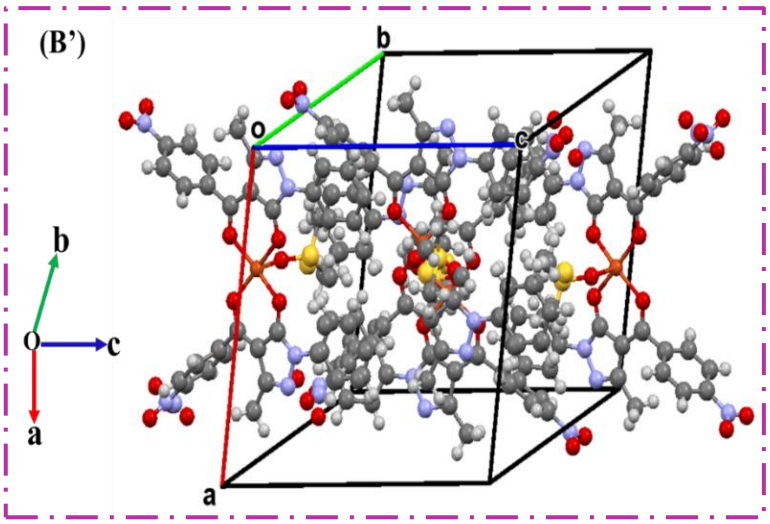

Fig.3a.10. Complex-2: (B)= Thermal ellipsoid plot with 50% probability of complex-1 (Hydrogen atoms omitted for clarity) and (B')= A perspective view of crystal packing plot of complex-2 along B-axis

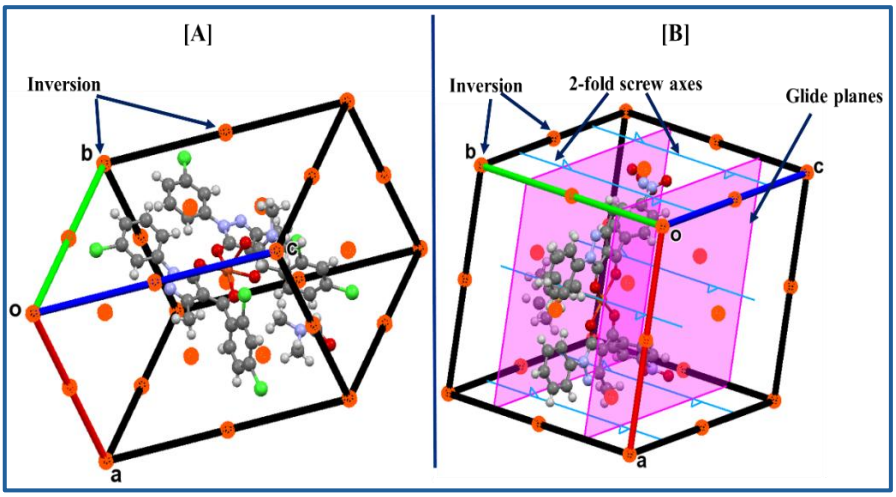

Fig.3a.11. [A] & [B] Symmetry elements present in complex-1 and complex-2

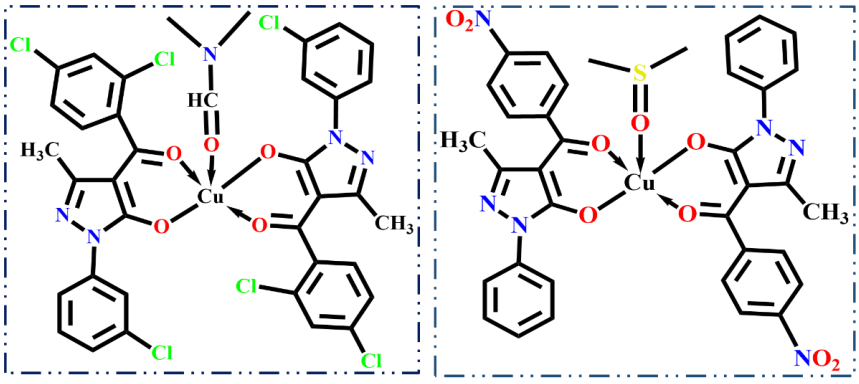

$[Cu(HL^{II})_2(DMF)]$ complex-1

$[Cu(HL^{IX})_2(DMSO)]$ complex-2

Fig.3a.12. 2D representation of the single crystal structures of complex-1 and complex-2

Table 3a.2 Bond lengths & Bond angles parameters of complex-1

Atoms	Bond lengths (Å)	Atoms	Bond lengths (Å)	Atoms	Bond angles (°)	Atoms	Bond angles (°)
Cu(1)-O(1)	1.93(2)	C(18)-N(1)	1.36(4)	O(1)-Cu-O(2)	94.1(8)	C(1)-N(3)-C(2)	131(2)
Cu(1)-O(2)	1.96(2)	C(19)-N(1)	1.43(4)	O(1)-Cu-O(4)	174.9(10)	C(1)-N(3)-N(4)	112(2)
Cu(1)-O(3)	1.93(2)	C(25)-N(2)	1.30(4)	O(1)-Cu-O(5)	97.4(9)	N(4)-N(3)-C(2)	118(3)
Cu(1)-O(4)	1.97(2)	C(1)-N(3)	1.35(4)	O(2)-Cu-O(4)	87.6(8)	C(8)-N(4)-N(3)	106(3)
Cu(1)-O(5)	2.31(2)	C(2)-N(3)	1.42(4)	O(2)-Cu-O(5)	82.95(9)	C(35)-N(5)-C(36)	122(4)
N(1)-N(2)	1.40(3)	C(8)-N(4)	1.30(4)	O(3)-Cu-O(1)	83.6(8)	C(35)-N(5)-C(37)	121(4)
N(3)-N(4)	1.41(3)	C(35)-N(5)	1.31(5)	O(3)-Cu-O(2)	166.3(10)	C(36)-N(5)-C(37)	117(4)
Cl(1)-C(23)	1.73(3)	C(36)-N(5)	1.45(6)	O(3)-Cu-O(4)	93.6(8)	C(1)-O(1)-Cu	121.5(19)
Cl(2)-C(30)	1.73(3)	C(1)-O(1)	1.28(3)	O(3)-Cu-O(5)	101.4(9)	C(11)-O(2)-Cu	127(2)
Cl(3)-C(32)	1.73(3)	C(11)-O(2)	1.28(3)	O(4)-Cu-O(5)	87.2(9)	C(18)-O(3)-Cu	121.8(19)
Cl(4)-C(6)	1.74(4)	C(18)-O(3)	1.27(3)	C(18)-N(1)-C(19)	130(2)	C(28)-O(4)-Cu	126.1(19)
Cl(5)-C(13)	1.73(3)	C(28)-O(4)	1.28(3)	C(18)-N(1)-N(2)	112(2)	C(35)-O(5)-Cu	120(2)
Cl(6)-C(15)	1.74(3)	C(35)-O(5)	1.22(4)	N(2)-N(1)-C(19)	118(2)	O(4)-C(28)-C(27)	124(3)
C(1)-C(10)	1.41(4)	C(13)-C(14)	1.39(5)	C(25)-N(2)-N(1)	106(2)	O(4)-C(28)-C(29)	115(2)
C(2)-C(3)	1.38(5)	C(19)-C(24)	1.38(4)	C(1)-N(3)-C(2)	131(2)	C(30)-C(29)-C(28)	122(3)

Table 3a.3. Complex-1: Symmetry transformations used to generate equivalent atoms

	Symmetry transformations
1	x, y, z
2	-x, -y, -z

Table 3a.4 Bond lengths & Bond angles parameters of complex-2

Atoms	Bond lengths (Å)	Atoms	Bond lengths (Å)	Atoms	Bond angles (°)	Atoms	Bond angles (°)
Cu(1)-O(1)	1.941(3)	C(1)-N(1)	1.362(5)	O(1)-Cu-O(3)	82.95(12)	S(1)-O(5)-Cu	113.4(3)
Cu(1)-O(2)	1.952(3)	C(5)-N(1)	1.469(11)	O(2)-Cu-O(3)	174.26(16)	O(7)-N(5)-O(6)	119.1(7)
Cu(1)-O(3)	1.932(3)	C(3)-N(2)	1.296(6)	O(1)-Cu-O(2)	93.90(12)	O(7)-N(5)-C(15)	125.5(7)
Cu(1)-O(4)	1.959(3)	C(18)-N(3)	1.358(5)	O(3)-Cu-O(4)	94.30(12)	O(6)-N(5)-C(15)	114.3(7)
Cu(1)-O(5)	2.270(5)	C(22)-N(3)	1.418(6)	O(1)-Cu-O(4)	167.11(16)	C(1)-N(1)-N(2)	111.2(3)
C(1)-O(1)	1.258(5)	C(20)-N(4)	1.288(6)	O(2)-Cu-O(4)	87.70(13)	C(1)-N(1)-C(5)	129.4(6)
C(11)-O(2)	1.252(5)	C(15)-N(5)	1.474(8)	O(3)-Cu-O(5)	91.41(17)	N(2)-N(1)-C(5)	118.6(6)
C(18)-O(3)	1.267(5)	C(32)-N(6)	1.473(6)	O(1)-Cu-O(5)	96.62(18)	C(3)-N(2)-N(1)	106.2(3)
C(28)-O(4)	1.263(5)	O(6)-N(5)	1.274(10)	O(2)-Cu-O(5)	93.73(17)	C(18)-N(3)-N(4)	110.9(3)
S(1)-O(5)	1.507(6)	O(7)-N(5)	1.136(6)	O(4)-Cu-O(5)	96.04(17)	C(18)-N(3)-C(22)	130.0(4)
N(1)-N(2)	1.405(5)	O(8)-N(6)	1.213(6)	C(1)-O(1)-Cu	121.5(3)	N(4)-N(3)-C(22)	119.0(3)
N(3)-N(4)	1.397(5)	O(9)-N(6)	1.205(6)	C(11)-O(2)-Cu	126.6(3)	C(20)-N(4)-N(3)	107.1(3)
S(1)-C(35)	1.812(10)	C(31)-C(32)	1.368(7)	C(18)-O(3)-Cu	121.7(3)	O(9)-N(6)-O(8)	123.7(4)
S(1)-C(36)	1.645(10)	C(2)-C(11)	1.395(6)	C(28)-O(4)-Cu	126.6(3)	O(9)-N(6)-C(32)	118.1(4)

Table 3a.5. Complex-2: Symmetry transformations used to generate equivalent atoms

	Symmetry transformations
1	x+1,y,z
2	x+2,-y+1,-z+2

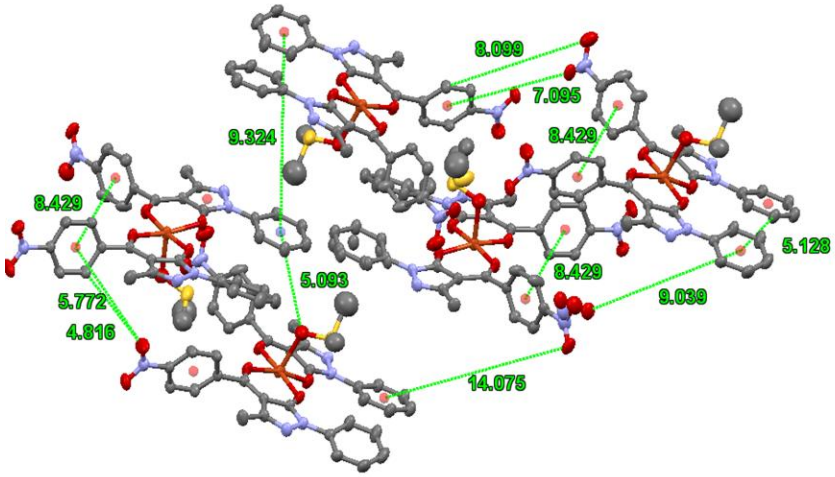

Fig.3a.13. Graphical illustration of C–O···π and off-set π···π stacking interactions in the crystal strucrure of complex-2 (Hydrogen atoms are omitted for clarity

Table 3a.6. Refinement parameters of complex-1 and complex-2

CODE	$[Cu(HL^{II})_2DMF]$ Complex-1	$[Cu(HL^{IX})_2DMSO]$ Complex-2
CCDC number	2263581	2281709
Chemical formula	$C_{37}H_{27}CuCl_6N_5O_5$	$C_{38}H_{30}CuN_6O_9S$
Formula weight	897.90	786.26
Crystal system	Triclinic	Monoclinic
Space group	*P*-1	$P2_1/c$
Temperature	298(2) K	293(2) K
Wavelength	1.54178 Å	1.54184 Å
Z	2	4
Density	1.489 Mg/m^3	1.518 Mg/m^3
Volume	2165.80(8) $Å^3$	3559.72(12) $Å^3$
Unit cell dimension	a=7.44180(10) Å b=11.3843(2) Å c=19.8633(4) Å	a= 14.4627(2) Å b= 17.1573(4) Å c= 14.7104(3) Å
	α,γ = 90° β=97.5520(10)°	α,γ = 90° β= 102.787(2)°
F (0 0 0)	776	1620
Theta range	66.706 to 4.487°	4.017 to 78.988°
R(int)	0.0791	0.0521
Absorption Correction	Multi-scan	Semi-empirical from equivalents
Index ranges	-18<=h<=13, -21<=k<=21, -18<=l<=18	-18<=h<=13, -21<=k<=21, -18<=l<=18
Refinement method	Multi-scan	Full-matrix least-squares on F^2
Goodness-of-fit on F^2	1.040	1.067
Final R indices [I>2sigma(I)]	R1= 0.1935, wR2= 0.2007	R1= 0.1000, wR2= 0.2643
Data/restraints/parameters	7537 / 0 / 530	3418 / 0 / 226
Largest diff. Peak and hole	0.578 and -0.810 $e.Å^{-3}$	0.952 and -0.825 $e.Å^{-3}$

3a.3.6 DFT based computational analysis

Density Functional Theory (DFT) is a computational method frequently employed in quantum chemistry to analyze the electronic structure of molecular systems. By focusing on electron density rather than wave functions, DFT enables precise calculations of molecular bonding, energy levels, and structural geometries. It serves as a valuable tool alongside experimental methods, providing deeper insights into various compounds' stability, reactivity, and properties. DFT is especially useful for investigating complex systems involving metal-ligand interactions and transition metal complexes. The B3LYP/6-31G level basis set is used to compute the geometry of complex-**1** [16][15]; in contrast, the B3LYP/ LANL2DZ level basis set is used to calculate the geometry of complex-**2** with Gauss View 6.0 software employed for processing the input files [17]. The optimization energies for complex-**1** and complex-**2** were found to be -182.454 keV and -125.564 keV, respectively. The calculated optimization energies for the copper complexes show notable variations depending on the selected basis set. The B3LYP/LANL2DZ basis set, which employs effective core potentials (ECPs), simplifies the treatment of core electrons, particularly for heavier elements such as copper. This basis set is especially useful for accurately modelling transition metals and other heavy elements [18].

Conversely, the 6-31G basis set does not incorporate ECPs, which may limit its ability to reflect the electronic behaviour of transition metals accurately. The B3LYP/LANL2DZ basis set excels in its accuracy for modelling transition metals, whereas the 6-31G basis set showcases the versatility and effectiveness of alternative computational methods in yielding valuable insights. These distinctions emphasize the importance of comprehensive computational analyses. The optimization energy value of both copper complexes is highly negative compared to that of respective ligands (Chapter **2**), which shows the stability of complexes over ligands. DFT analysis of ligands has already been stated in Chapter **2**. **Fig.3a.14** represents the optimized geometry of both complexes **1** & **2.**

The energy gap between the HOMO and LUMO significantly impacts a molecule's kinetic stability, chemical reactivity, optical polarizability, and hardness or softness. By examining the composition of these orbitals, we can predict molecular properties that influence a compound's reactivity and selectivity. These properties can be approximated using Koopmans' theorem, which links HOMO and LUMO energies to ionization energy and electron affinity [30]. The distribution of frontier orbital can be used to analyze active sites and reactivity of a compound. Frontier orbitals have been studied because they are

essential for determining chemical stability, energy value, and chemical behaviour [31]. The highest occupied molecular orbitals (HOMOs) are primarily located near the acylpyrazolone ligand, with energy values of -8.376 eV, -8.426 eV, and -9.056 eV for HOMO, HOMO-1, and HOMO-2, respectively. Similarly, the lowest unoccupied molecular orbitals (LUMOs) have energy levels of -2.060 eV, -2.277 eV, and -2.405 eV for LUMO, LUMO+1, and LUMO+2, respectively, for complex-**1**. In contrast, for complex-**2**, the HOMO, HOMO-1, and HOMO-2 energy values are -5.963 eV, -6.135 eV, and -6.456 eV, while the LUMO, LUMO+1, and LUMO+2 energy values are -3.040 eV, -3.018 eV, and -1.857 eV, respectively. The band gap (ΔE) for complex-**1** is 6.315 eV, and for complex-**2**, it is 2.922 eV. The HOMO-LUMO energy gap determines a molecule's electrical transport properties. A large gap suggests a stable molecule with low chemical reactivity [32]. The energy gap (ΔE) for complex-**1** is 6.315eV, and for complex-**2**, it is 2.922 eV. Therefore, complex-**1** is more stable due to its higher ΔE value, while complex-**2** is more reactive because of its lower ΔE value. The stability order is,

complex-1 > complex-2

The presence of an unpaired electron in the HOMO supports the paramagnetic nature of the square pyramidal copper complex. The global properties of the copper acylpyrazolone complex can also be further predicted by the energy gap (ΔE). The six frontier molecular orbitals (FMOs) and HOMO-LUMO energy diagram of complex-**1** and complex-**2** are shown in **Fig.3a.15.** The global parameters for complex-**1** and complex-**2** are presented in **Tables 3a.7-3a.8**, respectively. **Table 3a.9** shows a comparison of the practical and theoretical bond parameters**.**

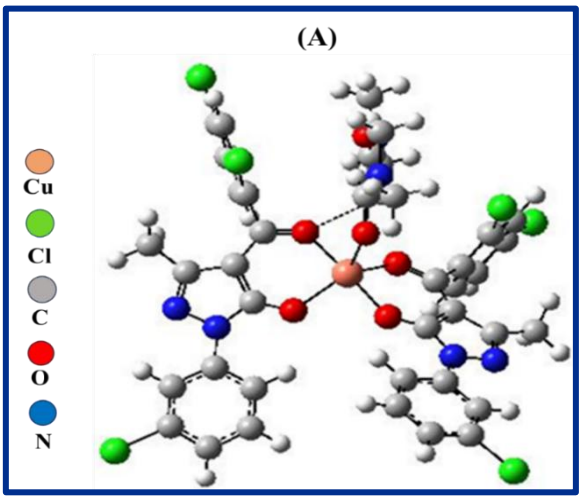

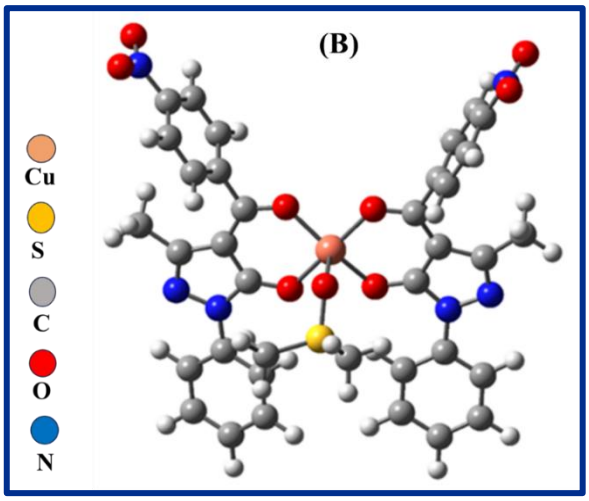

Fig.3a.14. DFT optimized Structures of (A) complex-1 and (B) complex-2

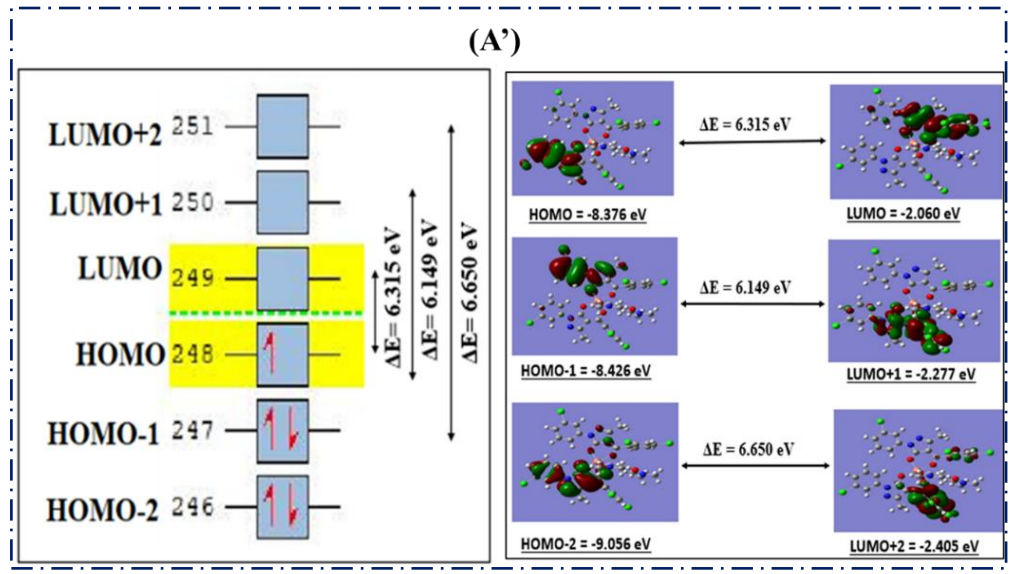

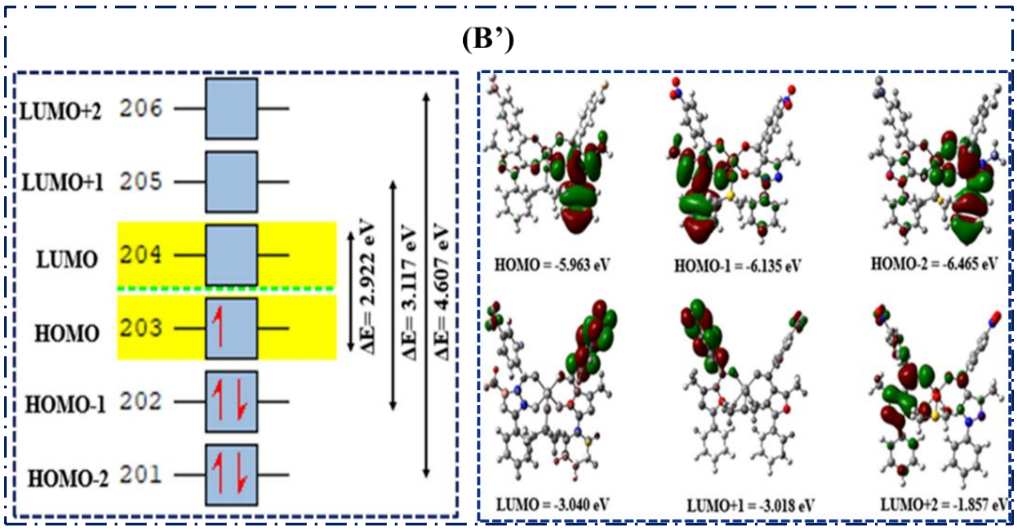

Fig.3a.15. HOMO–LUMO frontier orbital analysis energy diagram of (B) complex-1 and (B') complex-2

Table 3a.7. Global parameters of complex-1

Properties	Mathematical Formula	Complex-1
E_{HOMO}	E_{HOMO}	-8.376
E_{LUMO}	E_{LUMO}	-2.060
ΔE	$\Delta E = E_{LUMO}-E_{HOMO}$	6.316
Ionization potential (IP)	$IP = -E_{HOMO}$	8.376
Chemical Potential (μ)	$\mu = 1/2 (E_{HOMO} + E_{LUMO})$	-5.218
Electron affinity (EA)	$EA = -E_{LUMO}$	2.060
Electronegativity (EN)	$EN = -1/2 (E_{HOMO} + E_{LUMO})$	5.218
Global Hardness (Ƞ)	$\eta = -1/2 (E_{HOMO} - E_{LUMO})$	3.158
Softness (S)	$S = 1/2\eta$	0.158
Electrophilicity index (ω)	$\omega = \mu^2/2\eta$	4.310

Table 3a.8. Global parameters of complex-2

Properties	Mathematical Formula	Complex-2
E_{HOMO}	E_{HOMO}	-5.963
E_{LUMO}	E_{LUMO}	-3.040
ΔE	$\Delta E = E_{LUMO} – E_{HOMO}$	2.923
Ionization potential (IP)	$IP = -E_{HOMO}$	5.963
Chemical Potential (μ)	$\mu = 1/2 (E_{HOMO} + E_{LUMO})$	-4.501
Electron affinity (EA)	$EA = -E_{LUMO}$	3.040
Electronegativity (EN)	$EN = -1/2 (E_{HOMO} + E_{LUMO})$	4.501
Global Hardness (Ƞ)	$\eta = -1/2 (E_{HOMO} - E_{LUMO})$	1.461
Softness (S)	$S = 1/2\eta$	0.342
Electrophilicity index (ω)	$\omega = \mu^2/2\eta$	6.933

Table 3a.9. A comparison of the practical and theoretical bond parameters

Atoms	Practical bond length (Å)	Theoretical bond length (Å)	Atoms	Practical bond angles (°)	Theoretical bond angles (°)
$[Cu(HL^{II})_2DMF]$ complex-1					
Cu(1)-O(1)	1.93(2)	1.96	O(1)-Cu-O(2)	94.1(8)	91.5
Cu(1)-O(2)	1.96(2)	2.13	O(1)-Cu-O(4)	174.9(10)	174.1
Cu(1)-O(3)	1.93(2)	2.00	O(1)-Cu-O(5)	97.4(9)	91.40
Cu(1)-O(4)	1.97(2)	1.97	O(2)-Cu-O(4)	87.6(8)	93.28
Cu(1)-O(5)	2.31(2)	2.05	O(2)-Cu-O(5)	82.95(9)	90.20
N(1)-N(2)	1.40(3)	1.40	O(3)-Cu-O(1)	83.6(8)	86.0
N(3)-N(4)	1.41(3)	1.40	O(3)-Cu-O(2)	166.3(10)	165.1
Cl(1)-C(23)	1.73(3)	1.81	O(3)-Cu-O(4)	93.6(8)	95.46
Cl(2)-C(30)	1.73(3)	1.80	O(3)-Cu-O(5)	101.4(9)	104.1
Cl(3)-C(32)	1.73(3)	1.80	O(4)-Cu-O(5)	87.2(9)	90.5
Cl(4)-C(6)	1.74(4)	1.74	C(1)-O(1)-Cu	121.5(19)	125.9
Cl(5)-C(13)	1.73(3)	1.80	C(11)-O(2)-Cu	127(2)	128
Cl(6)-C(15)	1.74(3)	1.80	C(18)-O(3)-Cu	121.8(19)	122.97
C(1)-O(1)	1.28(3)	1.35	C(28)-O(4)-Cu	126.1(19)	129.03
C(11)-O(2)	1.28(3)	1.36	C(35)-O(5)-Cu	120(2)	125.05
$[Cu(HL^{IX})_2DMSO]$ complex-2					
Cu-O(1)	1.941(3)	1.952	O(3)-Cu(1)-O(1)	82.95(12)	85.45
Cu-O(2)	1.952(3)	1.985	O(3)-Cu(1)-O(2)	174.26(16)	175.36
Cu-O(3)	1.932(3)	1.943	O(1)-Cu(1)-O(2)	93.90(12)	95.45
Cu-O(4)	1.959(3)	1.967	O(3)-Cu(1)-O(4)	94.30(12)	98.76
Cu-O(5)	2.270(5)	2.278	O(1)-Cu(1)-O(4)	167.11(16)	169.25
O(1)-C(1)	1.258(5)	1.285	O(2)-Cu(1)-O(4)	87.70(13)	88.89
O(2)-C(11)	1.252(5)	1.262	O(3)-Cu(1)-O(5)	91.41(17)	94.43
O(5)-S(1A)	1.507(6)	1.512	O(1)-Cu(1)-O(5)	96.62(18)	99.15
N(5)-O(7)	1.136(9)	1.156	O(2)-Cu(1)-O(5)	93.73(17)	93.85
N(5)-O(6)	1.274(10)	1.289	O(4)-Cu(1)-O(5)	96.04(17)	96.10
N(5)-C(15)	1.474(8)	1.476	S(1A)-O(5)-Cu(1)	113.4(3)	117.54
O(8)-N(6)	1.213(6)	1.214	C(1)-O(1)-Cu(1)	121.5(3)	125.98
N(1)-N(2)	1.405(5)	1.415	C(11)-O(2)-Cu(1)	126.6(3)	130.12
O(7)-N(5)	1.136(6)	1.155	C(18)-O(3)-Cu(1)	121.7(3)	126.05

Theoretical vibrations can be used to investigate the changes which occur during complexation. Theoretical IR frequencies were obtained using DFT calculations after the complete optimization. According to the general observation, theoretical FTIR values are somewhat higher than practical FTIR values. Theoretical FTIR calculations typically model molecules in an isolated gas-phase state, overlooking external influences like hydrogen bonding and intermolecular interactions, which are common in practical experiments. These real-world factors and anharmonic vibrational behaviour tend to lower the frequencies observed in experimental FTIR measurements.

Furthermore, computational methods often approximate molecular vibrations using harmonic assumptions, resulting in predicted frequencies that are higher than those observed in experimental data. The nature of bonds, such as axial and equatorial, is primarily demonstrated by the relative impact of the complex's symmetric and asymmetric vibrations, resulting in a good connection [33]. Actual FTIR spectrum values and essential theoretical vibrations are summarised in **Table 3a.10.** The theoretical FTIR spectrum of complex-**1** is depicted in **Fig.3a.16.**

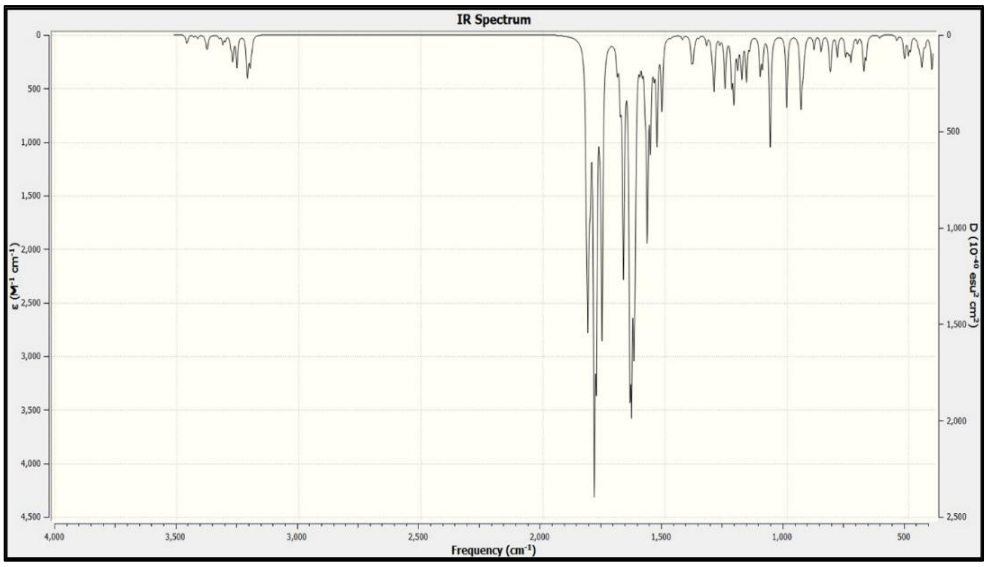

Fig.3a.16. FTIR spectrum of complex-1 through DFT computational analysis

Table 3a.10. comparison of theoretical and practical FTIR vibrational data of complex-1 and complex-2

IR Frequencies (cm^{-1})	Complex-1		Complex-2	
	TH	PR	TH	PR
ν(C=O) of benzoyl chloride	1558	1524	1610	1567
ν(C=O) of Pyrazolone	1655	1591	1687	1604
Cyclic ν(C=N)	1540	1471	1400	1380
C–H in-plane deformation	1164	1162	1250	1244

3a.3.6.1 Molecular electrostatic potential (MESP)

MESP (Molecular Electrostatic Potential) is a valuable descriptor for analyzing sites of electrophilic, nucleophilic, and hydrogen bonding interactions since it is closely related to electron density (ED). The reactive behaviour of a molecule can be studied using the MESP surface diagram, where a negative region indicates nucleophilic centres and a positive region indicates potential electrophilic sites. To analyze the reactivity of nucleophilic and electrophilic attacks on the synthesized copper complex, MESP was generated using the B3LYP/6-31G level of basis set. The MESP surface shows the molecular dimensions, size, and electrostatic potential of complex-**1**. The reddish region represents the most negative potential, while the bluish region indicates a moderate negative potential. In contrast, the green section represents a midpoint between the two extremes of red (most negative) and dark blue (most positive) on the MESP surface [8].

3a.3.6.2 Spin density plot analysis

Spin density is closely related to electron density and can be described as the difference between the total electron density of one spin and that of the other. When unpaired electrons are present in a system, spin density can provide more insightful information. Specifically, it refers to the difference between the α (alpha) and β (beta) electron densities. Spin density is positive in regions where electrons are more likely to be found in the α spin state, particularly around the metal centre, and negative in areas where electrons are more likely to be in the β spin state. Electron paramagnetic resonance (EPR) is an experimental technique that is particularly useful for determining the electronic spin density in a system. Like overall electron density, spin density can be computationally visualized using an isosurface. An isosurface is a three-dimensional representation of all points where a certain function such as spin density ρ(r) has a constant value, known as the isovalue. **Fig.3a.17** depicts the MESP and Spin density plots of complex-**1.** Mathematically, spin density is expressed as the following formula no **(2)** [34][35].

$$\rho s(r) = \rho\alpha(r) - \rho\beta(r) \qquad (2)$$

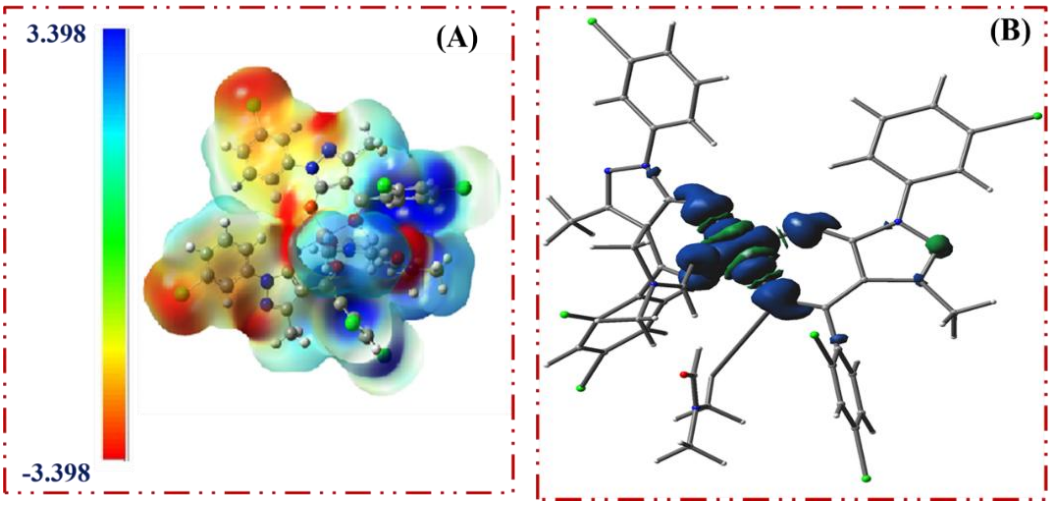

Fig.3a.17. Complex-1 : (A) MESP plot and (B) Spin density plot

3a.3.6.3 Natural bond orbital (NBO) analysis

It is possible to measure the delocalization of electron density between occupied Lewis-type NBOs (donor) and unoccupied non-Lewis-type NBOs (acceptor/Rydberg) through NBO analysis, which correlates to a stabilizing donor-acceptor interaction [8]. The synthesized complex was studied using the B3LYP/6-31G level basis set for NBO analysis. A coordination bond exists between the Cu(II) ion and oxygen atoms. This interaction allows the transfer of electron density from the lone pair orbital (LP) of the oxygen atom in the acylpyrazolone ligand or DMF solvent molecule to the antibonding orbital LP*(Cu). The highest negative charge is found on the oxygen atoms located at the axial positions. The natural atomic charges are: Cu^{+2} = +1.207, O(76)= -0.688, O(77)= -0.658, O(78)= -0.692, O(79)= -0.661. Copper has the natural electronic configuration: [core] 3d(9.11) 4s(0.29) 4p(0.38). The electron distribution includes 17.9977 core electrons, 9.7857 valence electrons (in the 4s, 3d, and 4p atomic orbitals), and 0.0092 Rydberg electrons (in the 4p, 4d, and 5p orbitals), resulting in a total of 27.7928 electrons. The natural atomic charge of copper (+1.2071) corresponds to the difference between the 27.7928 electrons in the complex and the total number of electrons in a free copper atom (29 electrons). Although the copper ion has a charge of +2 before complexation, the charge of the copper ion in the complex-**1** is reduced to +1.2072. An electronic cloud is present in the antibonding orbitals of the Cu^{2+} ion due to ligand-to-metal charge transfer (LMCT). All the findings from DFT computational analysis ultimately support the square pyramidal geometry of the synthesized copper acylpyrazolone complexes [36].

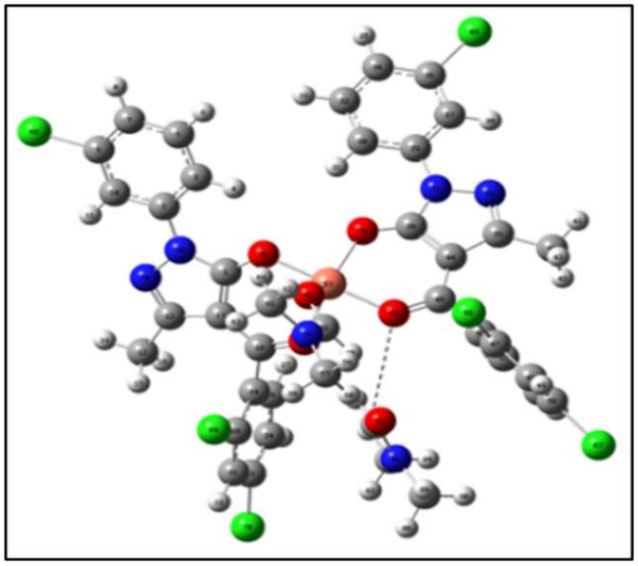

Fig.3a.18. DFT optimized geometry of complex-1 based on NBO analysis

3a.3.7 Hirshfeld surface area analysis

Hirshfeld surface analysis is a valuable technique for understanding interactions in crystal structures by examining the electron density surrounding a molecule. Hirshfeld surfaces are named in honour of F.L. Hirshfeld, whose "stockholder partitioning" method for assigning atomic contributions in molecules is inspired by characterizing a molecule within a crystal. The concept of the Hirshfeld surface was developed to delineate the spatial area occupied by a molecule in a crystal, allowing for the division of electron density into fragments corresponding to individual molecules. CrystalExplorer software was initially developed to facilitate Hirshfeld surface (HS) analysis, and it continues to serve as one of its primary functions [37]. This analysis utilized the crystal explorer 17.5 programme to visualize and investigate the intermolecular interactions and donor-acceptor interaction sites. This study has provided a thorough description of the immediate surroundings of the molecule [38]. Hirshfeld surfaces have been created over d_{norm}, d_e, d_i, shape index, curvedness and fragment patch. In copper complexes, the coordination with the Cu(II) ion is mainly achieved through interactions with four oxygen atoms derived from two acylpyrazolone ligands.

The molecular areas that calculate these surfaces can be visualized using transparent surfaces. The close-contact interactions are represented by the red, intense spots in the dnorm Hirshfeld surface that lead to the strong hydrogen bonding interactions [39]. The red portion indicates more intramolecular interactions or closeness to the nearby neighbouring molecule. The red and blue patches show how π … π stacking interaction occurs, such areas mapped across the shape index suggested not only intramolecular interactions but, in addition to this,

stacking interactions played a crucial role in stabilizing crystal packing. Such red-hot spots are usually absent, which indicates that the compound doesn't contain many significantly longer hydrogen bonds. The di (distance internal to the surface) and de (distance external to the surface) plots further support the interaction. The de parameter aids in determining the proximity of neighbouring molecules to the surface of the molecule being analyzed.

Meanwhile, the di value provides insight into how the molecule's internal atomic arrangement affects its interactions with surrounding external atoms. The shape index is especially sensitive to even the smallest changes. The concave regions of the shape index are represented by yellowish-orange triangles suggesting the atoms in the π···π stacked molecule [40]. The red-blue triangles indicate shorter non-covalent interactions. Analysis of the shape index suggests that intramolecular and stacking interactions play a significant role in stabilizing the crystal packing. Curvedness is a function of rms curvature, which indicates that the surface has a flat area and sharp surfaces, denoting low and high curvedness in packing [41]. The colours in fragment patches are utilized to illustrate various types of intermolecular interactions and their characteristics. Purple colour: usually signifies regions linked to hydrogen bonding interactions, indicating favourable contacts between hydrogen atoms and electronegative atoms, such as oxygen or nitrogen, in adjacent molecules. Blue represents weaker interactions or areas with lower contact density, suggesting reduced involvement in significant intermolecular interactions. Green colour denotes neutral or balanced regions where the strength of interactions is moderate, neither particularly strong nor weak. **Fig.3a.19** displays the 3D molecular hirshfeld surfaces of both complexes.

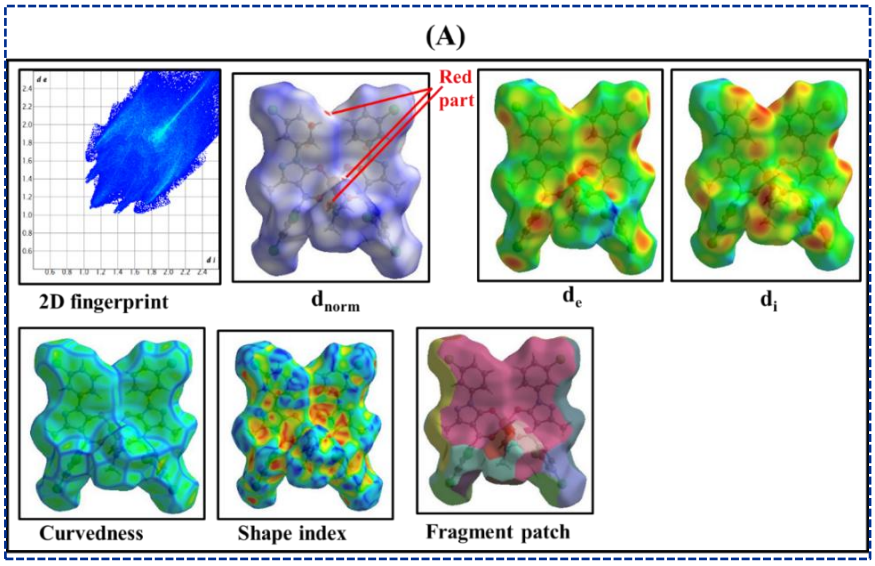

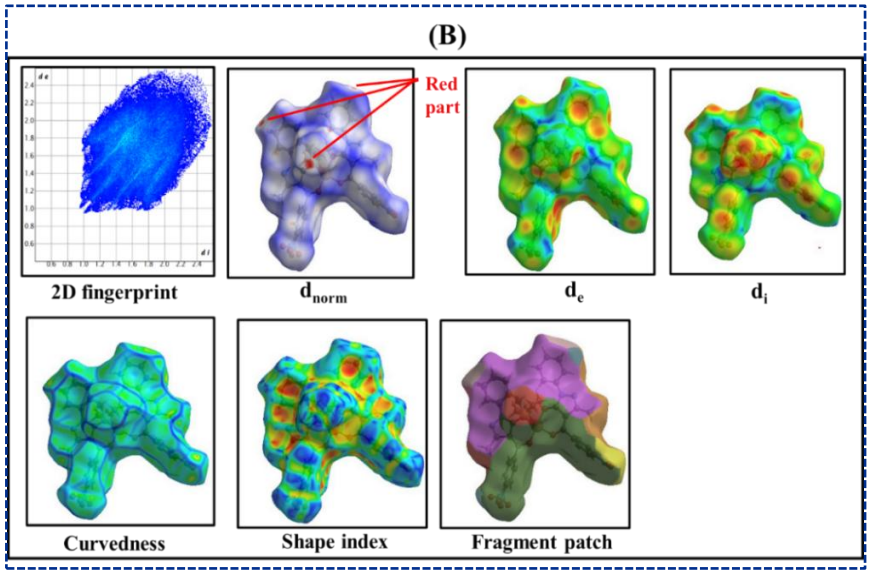

Fig.3a.19. The molecular Hirshfield (full FP diagram, dnorm, di, de, Curvedness, Shape index, and fragment patch) (A) complex-1 and (B) complex-2

In Hirshfeld surface analysis, 2D fingerprint plots offer visual and quantitative insight into intermolecular interactions within a crystal. With the aid of 2D fingerprint plots, non-covalent interactions that support the stability of crystal packing may be quantitatively studied. These plots display the distances between a molecule's surface and its neighbouring atoms, allowing the identification and differentiation of interaction types, including hydrogen bonding and van der Waals forces. As a result, fingerprint plots are essential for understanding how different interactions contribute to the overall stability and arrangement of the crystal structure. In 2D fingerprint plots from Hirshfeld surface analysis, blue and grey regions indicate varying frequencies of interactions and distances. Blue areas generally correspond to less frequent or weaker interactions, while grey regions show areas with minimal or no significant contributions to the molecular interactions. Two-dimensional fingerprint plots [42] of both complexes are displayed in **Fig.3a.20.**

Void analysis of both crystal structures was also performed using the same software. The voids are directly associated with the mechanical properties of the single crystals. A crystal with minimal voids generally exhibits good mechanical properties, such as stress response and a high melting point. From this perspective, we calculated voids by assuming spherical symmetry for all atoms and summing their electronic densities. Void analysis revealed that both complexes have void spaces of **9.00%** indicating a packing efficiency of 91.0% in both crystals. This high packing efficiency suggests that the molecules

in these compounds are tightly packed with minimal cavities. **Fig.3a.21** shows the voids present in the crystal structure of both complexes.

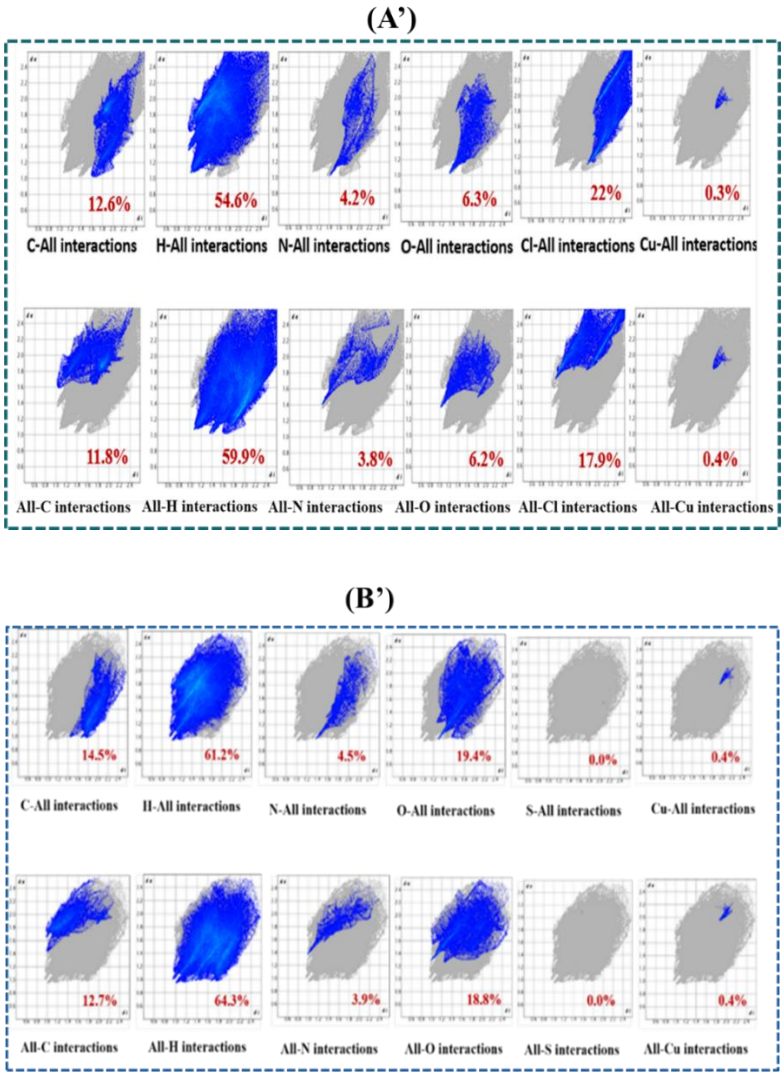

Fig.3a.20. Two-dimensional fingerprint plots of (A') complex-1 and (B') complex-2

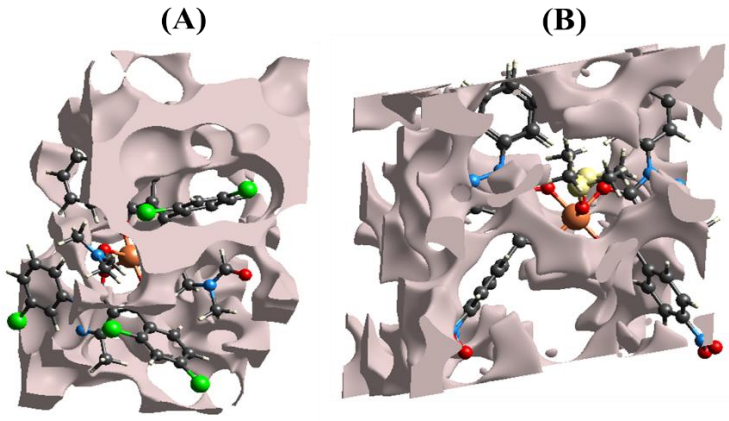

Fig.3a.21. Graphical representation of voids in the crystal structure (A) complex-1 & (B) complex-2

Two important concepts in this analysis are "atom-to-all" and "all-to-atom" interactions. This approach provides insights into how atoms engage with their neighbouring environment. The interaction of one atom within a molecule with another atom of its neighbours in the compound serves as another example of how molecules may pack efficiently [39]. The 'atom-to-all' interactions refer to how a single atom within a molecule contributes to the surrounding crystal lattice interactions. In contrast, 'all-to-atom' interactions describe how the overall environment influences a particular atom. These interactions are visualized through Hirshfeld surfaces, which offer a three-dimensional perspective on molecular packing and intermolecular forces. By studying these surfaces, one can gain crucial information about the strength and nature of interactions within the crystal structure. Due to the zero interactions in Cu-all and all-Cu in both complexes, There are no secondary interactions between copper metal and neighbouring atoms of surrounded molecules. There is significant interaction among the H atom(inside) and all atoms in both complexes, such as H-all interaction is 55% and 61% in complex-**1** and complex-**2**, respectively. Other interactions of O, N, Cl, etc, with all atoms and vice versa are demonstrated in **Fig.3a.22.**

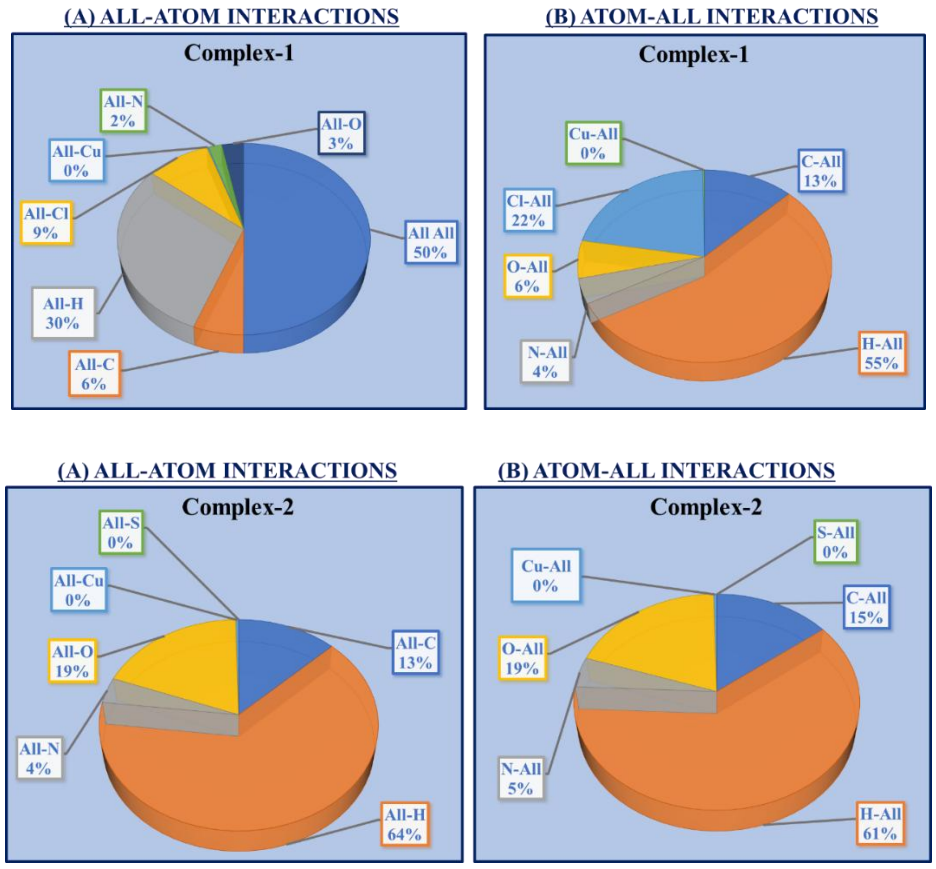

Fig.3a.22. Graphical presentation of percentage interactions between each inside and outside atom of complex-1 and complex-2, respectively

3a.3.8 ESR analysis (magnetic behaviour)

Electron Spin Resonance (ESR) spectroscopy is an essential analytical method for examining paramagnetic species, including Cu(II) complexes, characterized by their unpaired electrons. Cu(II) ions play a significant role in various biological and industrial applications due to their unique electronic characteristics, which can be effectively analyzed using ESR techniques [43]. This study focuses on determining the electronic environment surrounding the Cu(II) ion, revealing the coordination geometry, and enhancing our understanding of the ligand field effects that impact the properties of the complex. The ESR spectral analysis was conducted using a JEOL ESR spectrometer in powder form at room temperature, with tetracyanoethylene (TCNE) as a marker (g = 2.00277) to elucidate the geometry of the copper complexes. The Cu(II) complexes exhibit four lines. The value of $g_{\parallel}$ is 2.361, and $g_{\perp}$ is 2.050. The g tensor values, where $g_{\parallel} > g_{\perp} > 2.0023$, indicate the presence of an unpaired electron in a $dx^2\text{-}y^2$ orbital. The analysis showed that $g_{\parallel\,(2.361)} > g_{\perp\,(2.050)} > 2.0023$, suggesting that the ground state results from the $dx^2\text{-}y^2$ orbital and that the complex is axially symmetrical with the $dx^2\text{-}y^2$ ground state. The average g value was calculated using the formula $|g|^a = 1/3\,(g_{\parallel} + 2g_{\perp})$, yielding a $|g|^a$ value of 2.287 for the copper complex [25][28][44]. Both complex-**1** and complex-**2** have enough similarities in their characteristics and composition; hence, only complex-**1** has been taken for the ESR spectral study. **Fig.3a.23** shows the ESR spectrum complex-**1** at RT in the solid state.

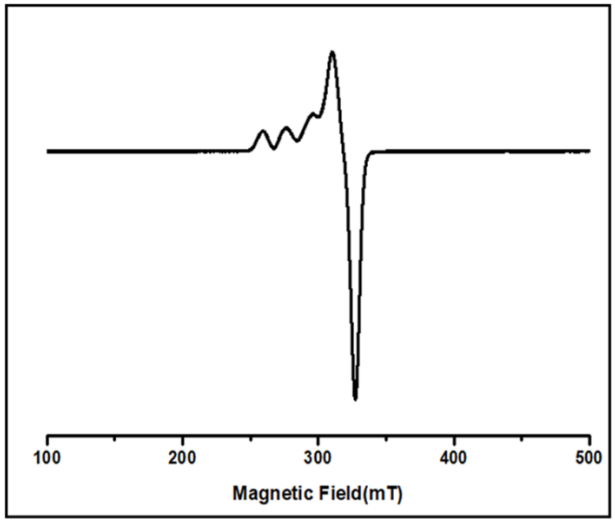

Fig.3a.23. X-band ESR spectra of complex-1 in the solid state at RT

3a.3.9 Electro-chemical analysis (CV)

Cyclic voltammetry is an electrochemical technique employed to investigate the redox behaviour of compounds by applying a variable potential to an electrochemical cell

and measuring the corresponding current. This method offers valuable insights into electron transfer processes' thermodynamic and kinetic aspects, making it an essential tool for characterizing electroactive species [45]. The redox behaviour of complex-**1** and complex-**2** was studied through CV analysis. The diagram shows the two oxidation and two reduction peaks. An anodic oxidation peak Epa(I) = -0.7981 V ($Cu^{0+} \rightarrow Cu^{1+}$) and Epa(II) = 1.3132 V($Cu^{1+} \rightarrow Cu^{2+}$) observed and reduction peak Epc(I) = -1.3936 V ($Cu^{2+} \rightarrow Cu^{1+}$) and Epc(II) = -0.3301 V ($Cu^{1+} \rightarrow Cu^{+0}$) observed for complex-**1.** For complex-**2,** Epa(I) = -0.6108 V (corresponding to the transition from $Cu^{0} \rightarrow Cu^{1+}$) and Epa(II) = 1.4150 V ($Cu^{1+} \rightarrow Cu^{2+}$). The reduction peaks appeared at Epc(I) = -1.3454 V ($Cu^{2+} \rightarrow Cu^{1+}$) and Epc(II) = -0.2196 V ($Cu^{1+} \rightarrow Cu^{0}$). For complex-**1,** the value of ΔEp_1 is 0.5955 V and ΔEp_2 is 1.6433 V for each redox couple. The ΔEp_1 (0.3912 V) and ΔEp_2 (1.5650 V) are potential differences for complex-**2** for each redox couple. These differences increased with the scan rate, suggesting the quasi-reversible nature of the redox process [46]. The ratio of the anodic peak to cathodic peak currents for the first redox couple is (Ipa_1/Ipc_1) -0.0031 amp and -0.0050 amp for complex-**1** and complex-**2**, respectively. Meanwhile, (Ipa_2/Ipc_2) is -2.0139 amp and -2.3347 amp, sequentially for complex-**1** and complex-**2.** The cyclic voltammograms of both complexes are shown in **Fig.3a.24.**

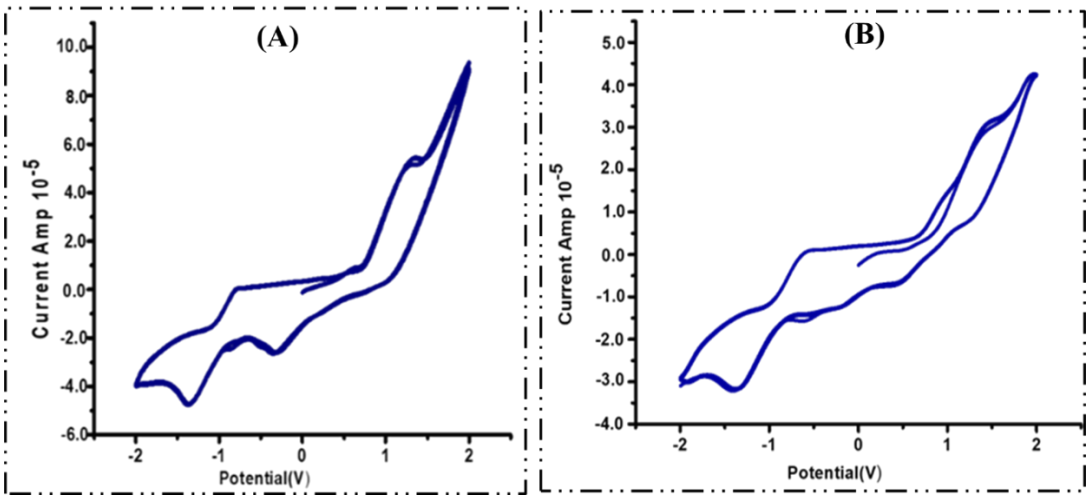

Fig.3a.24. Cyclic voltammograms of (A) complex-1 and (B) complex-2 in DMSO solution using 0.1 M TBAP at scan rate 100 mV and 50 mV, respectively

3a.3.10 *In vitro* Anti-cancer activity

The anti-cancer efficacy of both complexes was evaluated using a cytotoxicity assay, revealing a significant level of cytotoxic activity [16]. Both complexes were tested against three different cancer cell lines: NCI-H23 (lung cancer), HepG2 (liver cancer), and SH-SY5Y (neuroblastoma), with the half-maximal inhibitory concentration (IC_{50}) value

determined for each. The IC_{50} value represents the concentration at which 50% inhibition of cell growth occurs. Given the lower IC_{50} values of the synthesized compounds, they were compared to the well-known chemotherapeutic agent cisplatin to assess their effectiveness. Cisplatin was tested against the NCI-H23 and SH-SY5Y cancer cell lines. After 24 hours of exposure, the results indicated that the compounds investigated exhibited profound cytotoxic effects.

3a.3.10.1 MTT assay

Cell viability was assessed using the MTT assay. Complex-**1** and complex-**2** effectively inhibited the viability of NCI-H23, SH-SY5Y and HepG2 cancer cells. Complex-**1** demonstrated high efficacy across all three cancer cell lines, while complex-**2** was particularly effective against the SH-SY5Y cell line. The IC_{50} values for both complexes are listed in **Table 3a.11**. Cisplatin, a chemotherapy drug commonly used to treat various cancers, including lung cancer, was also evaluated. The IC_{50} value for cisplatin was determined against the NCI-H23 and SH-SY5Y cell lines. **Fig. 3a.25** shows the percentage of cell viability for NCI-H23, SH-SY5Y and HepG2 cancer cells exposed to varying doses of complex-**1**. The comparative effects of complex-**1** versus cisplatin on the NCI-H23 cell line are presented in **Fig.3a.26**. Additionally, **Fig.3a.27** depicts the comparison of % cell viability on SH-SY5Y cells exposed to complex-**2** and cisplatin. Cisplatin serves as a reference compound for contrast due to its established efficacy in treating various cancers; however, it often results in considerable side effects and the development of resistance. The synthesized two complexes have been demonstrated to have superior *in vitro* anti-cancer activity, indicating that they may serve as a more effective and safer alternative to cisplatin.

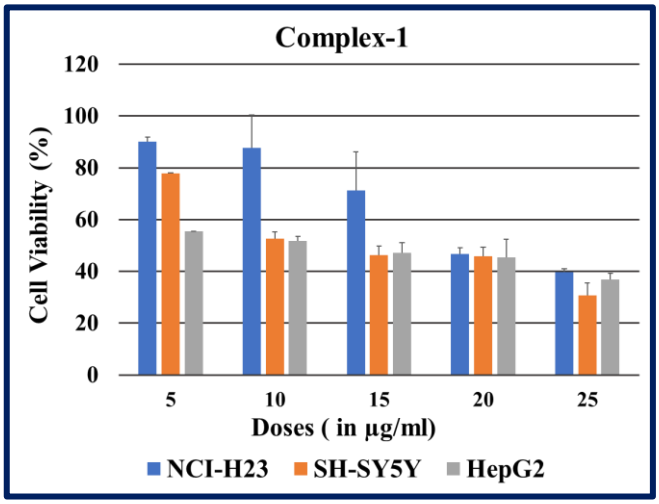

Fig.3a.25. Percent cell viability of NCI-H23, SH-SY5Y and HepG2 cancer cells exposed to indicated doses of complex-1

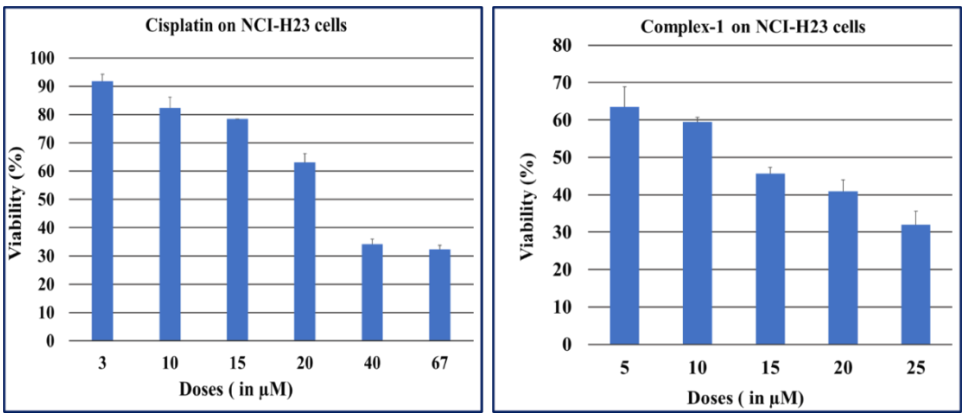

Fig.3a.26. A comparison of % cell viability on NCI-H23 cells exposed to complex-1 and cisplatin

Table 3a.11. Percent inhibition (IC_{50} values) of complex-1 and complex-2 against NCI-H23, SH-SY5Y and HepG2 cancer cells

Percent inhibition (IC_{50} values)			
Compounds	**Complex-1**	**Complex-2**	**Cisplatin**
NCI-H23	14.3 µM	-	17.65 µM
SH-SY5Y	7.2 µM	36.74 µM	44.94 µM
HepG2	7.1 µM	-	-

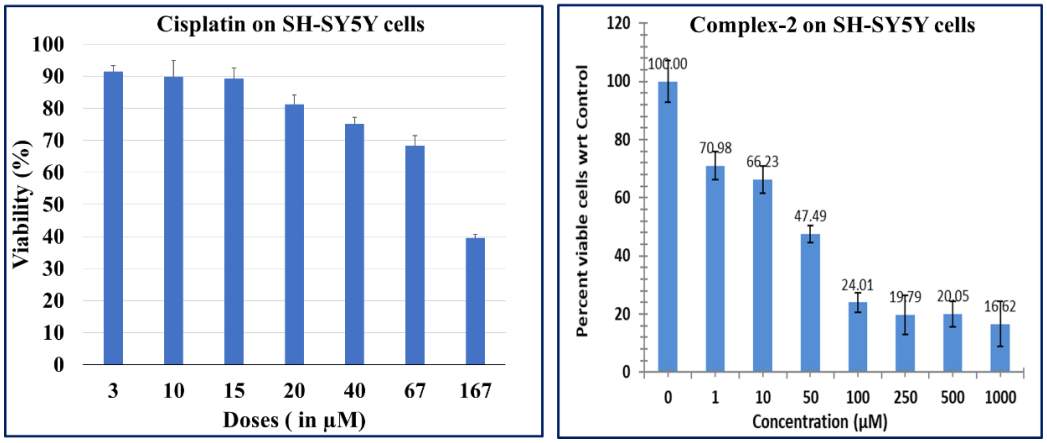

Fig.3a.27. A comparison of % cell viability SH-SY5Y cells exposed to complex-2 and cisplatin

3a.3.10.2 Cell death analysis

Lung cancer remains a leading cause of cancer-related deaths worldwide, characterized by a high propensity for rapid metastasis. This underscores the importance of early diagnosis for improved treatment outcomes, so this study focuses primarily on lung cancer [22]. The results indicate that complex-**1** exhibits greater efficacy against NCI-H23 cells, leading to its selection for further analysis against the lung cancer cell line. A Live/Dead assay assessed cell viability, distinguishing between live and dead cells. Calcein

dye generates green fluorescence to indicate live cells, while Ethidium homodimer-1 (EthD-1) emits red fluorescence, denoting dead and apoptotic cells [47]. The results revealed significant cell death, as evidenced by the predominant red fluorescence. In contrast, negligible cell death was observed in the control medium, highlighting the substantial apoptotic effects induced by treatment with the synthesized copper complex. A live-dead assay analysis of complex-**1** is shown in **Figs.3a.28-3a.29.**

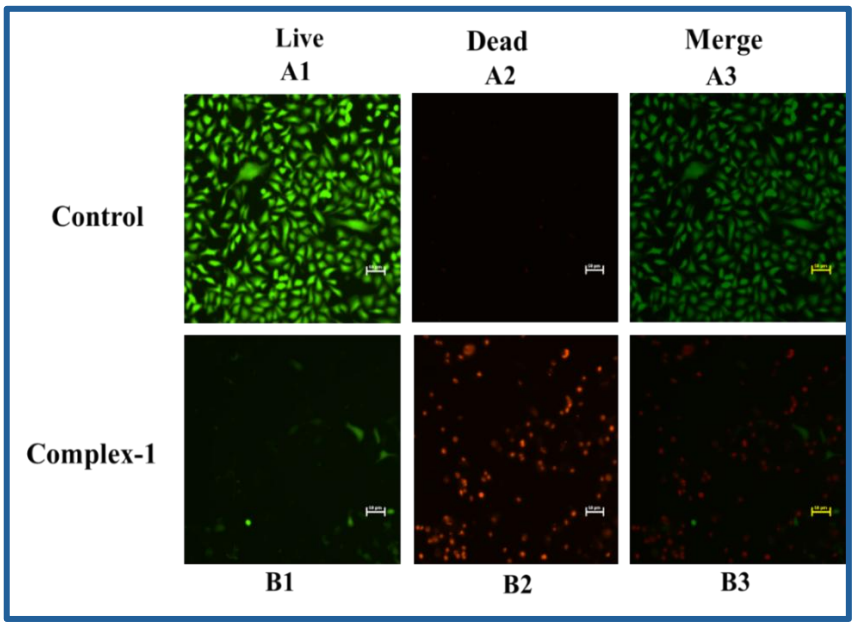

Fig.3a.28. Dual staining of NCI-H23 cells exposed to complex-1 for 24h

(A1&A2) = Untreated cells stained by Calcein and EthD-1 dyes, respectively

(B1&B2) = Treated cells stained by Calcein and EthD-1 dyes, respectively

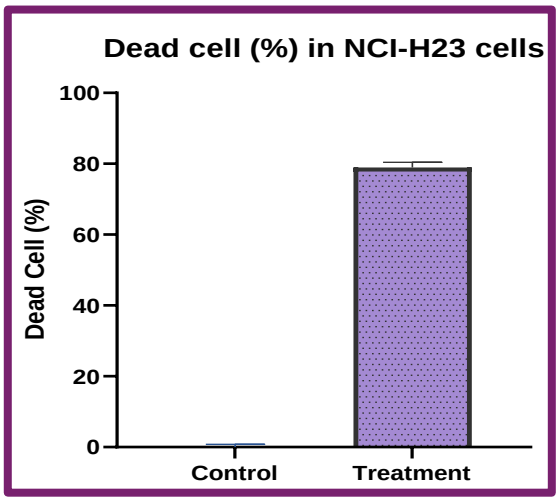

Fig.3a.29. Percentage of dead cells of NCI-H23 exposed to complex-1, calculated by ImageJ Analysis

3a.3.10.3 Scratch Assay/Wound closure assay

The observed enhanced efficacy of the compound prompted further investigation, leading to the performance of a scratch assay to evaluate cell migration dynamics. In this study, cells (3×10^5 cells/well) were cultured in 24-well plates for 24 hours to form a monolayer. A sterile pipette tip (20–200 µL) was then used to create a cross-shaped scratch in each well. The wells were washed with 500 µL of PBS and shaken at 500 rpm for 5 minutes to remove detached cells. Following this, 500 µL of fresh medium, either with or without diluted samples, was added, and the cells were incubated for additional hours. Before image acquisition, the plates were washed again with 500 µL of pre-warmed PBS and gently shaken for 30 seconds. Fresh pre-warmed medium or sample was then added, and images were captured. Scratch closure was monitored and imaged at 24-hour intervals using an automated imaging system [20]. Wound closure was quantitatively assessed using ImageJ analysis at three distinct time points: 0 hours, 24 hours and 48 hours, under both untreated and treated conditions. At the 24-hour interval, approximately 41% of wound closure was recorded in the control group, while a reduction to 29% was noted in the treated condition.

Similarly, at 48 hours, the untreated group demonstrated approximately 75% wound closure, in contrast to 45% in the treated group. These findings indicate that the synthesized copper pyrazolone complex-**1** effectively inhibits the migratory capacity of NCI-H23 lung cancer cells. A scratch assay analysis of complex-**1** is pictured in **Fig.3a.30.**The wound closer (%) of NCI-H23 cells in untreated and treated conditions at 24 h and 48 h is shown in **Fig.3a.31.**

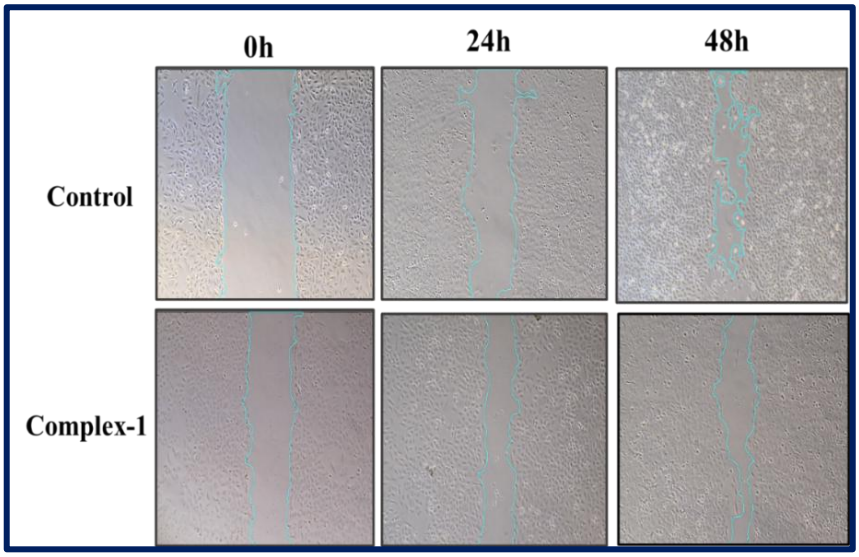

Fig.3a.30. Scratch assay of NCI-H23 cells exposed to complex-1 in the control and treated conditions at 0h, 24h and 48h

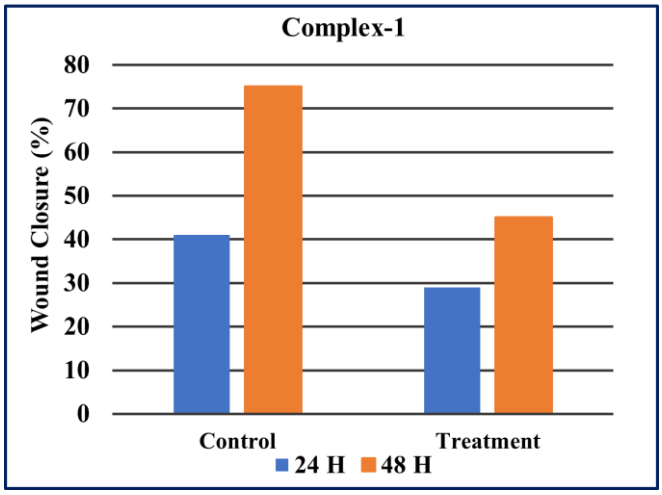

Fig.3a.31. Complex-1: Wound closer (%) of NCI-H23 cells in untreated and treated conditions at 24 h and 48 h, calculated by ImageJ software

3a.4 Conclusion

In this chapter, we synthesized two Cu(II) complexes based on heterocyclic pyrazolone derivatives. Two complexes, complex-**1** and complex-**2,** were synthesized and thoroughly characterized using a range of analytical and spectroscopic techniques. Single-crystal X-ray diffraction analysis confirmed the square pyramidal geometry of both complexes. The data revealed the binding sites, where four oxygen atoms from the ligands coordinated to the central Cu(II) metal at equatorial positions. Meanwhile, an oxygen atom from DMF and DMSO coordinated at the axial position in complex-**1** and complex-**2**, respectively. Both complexes were stable at room temperature, and their structures were further optimized using DFT analysis. The theoretical bond lengths and bond angles showed good agreement with experimental values. ESR studies indicated the paramagnetic nature of a compound. At the same time, cyclic voltammetry (CV) revealed the quasi-reversible redox behaviour of both complexes. Additionally, Hirshfeld surface analysis was performed to investigate intermolecular interactions. The void analysis revealed minimal void spaces in the crystal structure, indicating efficient packing. This suggests enhanced mechanical stability *In vitro*, anti-cancer activity demonstrated promising activity of the synthesized compounds. A complex-**1** effectively inhibits cell viability and lung adenocarcinoma (NCI-H23) cell migration. Future research could explore the *in vivo* therapeutic potential of these copper-based compounds to improve lung cancer patient outcomes.

References

[1] E. C. Constable, Evolution and understanding of the d-block elements in the periodic table, Dalt. Trans. (2019). https://doi.org/10.1039/C9DT00765B.

[2] R.K. Sodhi, Metal Complexes in Medicine: An Overview and Update from Drug Design Perspective, Cancer Ther. Oncol. Int. J. 14 (2019). https://doi.org/10.19080/ctoij.2019.14.555883.

[3] C. Molinaro, A. Martoriati, L. Pelinski, K. Cailliau, Copper Complexes as Anticancer Agents Targeting, (2020) 1–27.

[4] A.V.P. Bobadilla, J. Arévalo, E. Sarró, H.M. Byrne, P.K. Maini, T. Carraro, S. Balocco, A. Meseguer, T. Alarcón, In vitro cell migration quantification method for scratch assays, J. R. Soc. Interface. 16 (2019). https://doi.org/10.1098/rsif.2018.0709.

[5] K.M. Vyas, R.N. Jadeja, D. Patel, R. V. Devkar, V.K. Gupta, A new pyrazolone based ternary Cu(II) complex: Synthesis, characterization, crystal structure, DNA binding, protein binding and anti-cancer activity towards A549 human lung carcinoma cells with a minimum cytotoxicity to non-cancerous cells, Polyhedron. 65 (2013) 262–274. https://doi.org/10.1016/j.poly.2013.08.051.

[6] A.K. Patel, R.N. Jadeja, R.J. Butcher, M.K. Kesharwani, J. Kästner, M. Muddassir, mimetic activity, Polyhedron. (2020) 114969. https://doi.org/10.1016/j.poly.2020.114969.

[7] R.N. Jadeja, K.M. Vyas, V.K. Gupta, R.G. Joshi, C. Ratna Prabha, Syntheses, characterization and molecular structures of calcium(II) and copper(II) complexes bearing O2-chelate ligands: DNA binding, DNA cleavage and anti-microbial study, Polyhedron. 31 (2012) 767–778. https://doi.org/10.1016/j.poly.2011.11.004.

[8] J.M.M. and R.C.M. PRADEEP KUMAR VISHWAKARMA, Pyrone-based Cu (II) complexes , their characterization , DFT based conformational drift from square planar to square pyramidal geometry, 128 (2016) 511–522. https://doi.org/10.1007/s12039-016-1048-6.

[9] A.K. Patel, R.N. Jadeja, H. Roy, R.N. Patel, S.K. Patel, R.J. Butcher, M. Cortijo, S. Herrero, Copper(II) hydrazone complexes with different nuclearities and geometries: Synthesis, structural characterization, antioxidant SOD activity and antiproliferative properties, Polyhedron. 186 (2020) 114624.

https://doi.org/10.1016/j.poly.2020.114624.

[10] R.C.D. G.H.Jeffery, J.Baddett, J.Mendham, Vogel's textbook of quantitative chemical analysis, n.d. https://doi.org/10.1085/jgp.25.4.523.

[11] G. Vala, A.A. Puranik, R.N. Jadeja, D. Choquesillo-Lazarte, Solvent Free, Selective Oxidation of Styrene Catalyzed by Cobalt Acylpyrazolone Supported onto Neutral Alumina: Synthesis and Spectral Characterization, ChemistrySelect. 9 (2024). https://doi.org/10.1002/slct.202304086.

[12] G.M. Sheldrick, Crystal structure refinement with SHELXL, Acta Crystallogr. Sect. C Struct. Chem. 71 (2015) 3–8. https://doi.org/10.1107/S2053229614024218.

[13] G.M. Sheldrick, SHELXT - Integrated space-group and crystal-structure determination, Acta Crystallogr. Sect. A Found. Crystallogr. 71 (2015) 3–8. https://doi.org/10.1107/S2053273314026370.

[14] C.F. Macrae, P.R. Edgington, P. McCabe, E. Pidcock, G.P. Shields, R. Taylor, M. Towler, J. Van De Streek, Mercury: Visualization and analysis of crystal structures, J. Appl. Crystallogr. 39 (2006) 453–457. https://doi.org/10.1107/S002188980600731X.

[15] E. Aljuhani, M.M. Aljohani, A. Alsoliemy, R. Shah, H.M. Abumelha, F.A. Saad, A. Hossan, Z.A. Al-Ahmed, A. Alharbi, N.M. El-Metwaly, Synthesis and characterization of Cu(II)-pyrazole complexes for possible anti-cancer agents; conformational studies as well as compatible in-silico and in-vitro assays, Heliyon. 7 (2021) e08485. https://doi.org/10.1016/j.heliyon.2021.e08485.

[16] D. Shoba, S. Periandy, M. Karabacak, S. Ramalingam, Vibrational spectroscopy (FT-IR and FT-Raman) investigation, and hybrid computational (HF and DFT) analysis on the structure of 2,3-naphthalenediol, Spectrochim. Acta - Part A Mol. Biomol. Spectrosc. 83 (2011) 540–552. https://doi.org/10.1016/j.saa.2011.09.002.

[17] P.J. Hay, W.R. Wadt, Ab initio effective core potentials for molecular calculations. Potentials for the transition metal atoms Sc to Hg, J. Chem. Phys. 82 (1985) 270–283. https://doi.org/10.1063/1.448799.

[18] L. Chen, T. Liu, J.-Z. Chen, A density functional theory study on the electronic structures and properties of methylenediaminetetraacetate complexes (M=Co, Ni, Cu,

Zn, Cd), Acta Chim. Sin. 66 (2008) 1187–1195.

[19] T. Mosmann, Rapid Colorimetric Assay for Cellular Growth and Survival: Application to Proliferation and Cytotoxicity Assays, RSC Adv. 65 (1983) 55–63. https://doi.org/10.1039/c6ra17788c.

[20] X. Wang, C.C. Decker, L. Zechner, S. Krstin, M. Wink, In vitro wound healing of tumor cells: Inhibition of cell migration by selected cytotoxic alkaloids, BMC Pharmacol. Toxicol. 20 (2019) 1–12. https://doi.org/10.1186/s40360-018-0284-4.

[21] S.P.C. Cole, Rapid chemosensitivity testing of human lung tumor cells using the MTT assay, Cancer Chemother. Pharmacol. 17 (1986) 259–263. https://doi.org/10.1007/BF00256695.

[22] C. Hu, S. He, Y.J. Lee, Y. He, E.M. Kong, H. Li, M.A. Anastasio, G. Popescu, Live-dead assay on unlabeled cells using phase imaging with computational specificity, Nat. Commun. 13 (2022). https://doi.org/10.1038/s41467-022-28214-x.

[23] S. Parihar, S. Pathan, R.N. Jadeja, A. Patel, V.K. Gupta, Synthesis and Crystal Structure of an Oxovanadium(IV) Complex with a Pyrazolone Ligand and Its Use as a Heterogeneous Catalyst for the Oxidation of Styrene under Mild Conditions, Inorg. Chem. 51 (2012) 1152–1161. https://doi.org/10.1021/ic202396q.

[24] W.J. Geary, The use of conductivity measurements in organic solvents for the characterization of coordination compounds, Coord. Chem. Rev. 7 (1971) 81–122. https://doi.org/10.1016/S0010-8545(00)80009-0.

[25] S. Roy, P. Mitra, A.K. Patra, Cu(II) complexes with square pyramidal (N2S)CuCl2 chromophore: Jahn-Teller distortion and subsequent effect on spectral and structural properties, Inorganica Chim. Acta. 370 (2011) 247–253. https://doi.org/10.1016/j.ica.2011.01.068.

[26] W. Maalej, P. Guionneau, Z. Elaoud, A new square pyramidal copper(II) complex [Cu(C10H24N4)Br]Br: Crystal structure, thermal analysis, Hirschfeld surfaces, electrical and semiconducting properties, J. Mol. Struct. 1241 (2021) 130630. https://doi.org/10.1016/j.molstruc.2021.130630.

[27] L. Tong, L.-L. Gan, H.-W. Zhang, Y.-X. Sun, H.-Y. Niu, W.-K. Dong, Synthesis, structure, theoretical studies, and properties of dinuclear Cu(II) and novel trinuclear

Co(II) complexes with a more flexible 3-MeOsalamo-like ligand, J. Mol. Struct. 1294 (2023) 136465. https://doi.org/https://doi.org/10.1016/j.molstruc.2023.136465.

[28] DR. S. VALARSELVAN, Electronic Spectra of Transition metal complexes Spectroscopic ground states , spectral terms , R-S coupling and J-J couplings- term symbol – selection rules — microstates — Pigeon hole diagram for p2 and d2 configuration . Orgel and Tanabe – sugano diagr, n.d.

[29] S.J. Munshi, J.K. Saini, S. Ingle, S.B. Kumar, Metal(II) chloride complexes containing a tridentate N-donor Schiff base ligand: syntheses, structures and antimicrobial activity, J. Coord. Chem. 74 (2021) 2004–2016. https://doi.org/10.1080/00958972.2021.1940157.

[30] O. V Gritsenko, Koopmans’ theorem and its density-functional-theory analog assessed in evaluation of the red shift of vertical ionization potential upon complexation, Chem. Phys. Lett. (2017). https://doi.org/10.1016/j.cplett.2017.11.019.

[31] A.K. Patel, R.N. Jadeja, H. Roy, R.N. Patel, S.K. Patel, R.J. Butcher, Pseudo-tetrahedral copper(II) complex derived from N'-[(2E,3Z)-4-hydroxy-4-phenylbut-3-en-2-ylidene]acetohydrazide: Synthesis, molecular structure, quantum chemical investigations, antioxidant and antiproliferative properties, J. Mol. Struct. 1185 (2019) 341–350. https://doi.org/10.1016/j.molstruc.2019.03.004.

[32] Y.P. Singh, R.N. Patel, Y. Singh, Crystal structure, configurational and DFT study of nickel(II) complexes with N2O-donor type Schiff base ligand, Indian J. Chem. - Sect. A Inorganic, Phys. Theor. Anal. Chem. 57A (2018) 44–51.

[33] E.B. Elkaeed, E.U. Mughal, S. Kausar, H.A. Al-ghulikah, N. Naeem, A.A. Altaf, A. Sadiq, Theoretical vibrational spectroscopy (FT-IR), PED and DFT calculations of chromones and thiochromones, J. Mol. Struct. 1270 (2022) 133972. https://doi.org/https://doi.org/10.1016/j.molstruc.2022.133972.

[34] M. Savarese, É. Brémond, I. Ciofini, C. Adamo, Electron Spin Densities and Density Functional Approximations: Open-Shell Polycyclic Aromatic Hydrocarbons as Case Study, J. Chem. Theory Comput. 16 (2020) 3567–3577. https://doi.org/10.1021/acs.jctc.0c00059.

[35] C. Ravi, S. Kumar, Approach of Density Functional Theory to Molecules Using Gaussian, Int. J. Pure Appl. Phys. 15 (2019) 1–13. http://www.ripublication.com.

[36] M. Sithambaresan, M.R.P. Kurup, G. Serdaroğlu, S. Kaya, Copper(II) chelates derived from an N,N,O-tridentate 2-pyridinecarboxaldehyde-N4-phenylsemicarbazone: Synthesis, spectral aspects, crystal structure, FMO and NBO analysis, J. Mol. Struct. 12[1] M. S (2023) 134866. https://doi.org/https://doi.org/10.1016/j.molstruc.2022.134866.

[37] M.A. Spackman, D. Jayatilaka, Hirshfeld surface analysis, CrystEngComm. 11 (2009) 19–32. https://doi.org/10.1039/b818330a.

[38] J.H. Pandya, M. Travadi, R.N. Jadeja, R.N. Patel, V.K. Gupta, Synthesis, crystal feature and spectral characterization of paeonol derived Schiff base ligands and their Cu(II) complexes with antimicrobial activity, J. Indian Chem. Soc. 99 (2022) 1–8. https://doi.org/10.1016/j.jics.2022.100403.

[39] M. Travadi, R.N. Jadeja, R.J. Butcher, Synthesis, Covalency Sequence, and Crystal Features of Pentagonal Uranyl Acylpyrazolone Complexes along with DFT Calculation and Hirshfeld Analysis, ACS Omega. 7 (2022) 34359–34369. https://doi.org/10.1021/acsomega.2c03923.

[40] Qiong Wu, Q. Zi, Y. Qiao, Copper(II) Coordination Complex Constructed from Halogenated Tetradentate Schiff Base Ligand: Synthesis, Crystal Structure, and Hirshfeld Surface Analysis, Crystallogr. Reports. 64 (2019) 905–909. https://doi.org/10.1134/S1063774519060166.

[41] M. Travadi, R.N. Jadeja, R.J. Butcher, Synthesis, covalency parameters, energy calculations and crystal features of acylpyrazolone derived pentavalent Uranyl complex along with DFT and Hirshfeld analysis, Polyhedron. 223 (2022) 1–15. https://doi.org/10.1016/j.poly.2022.115956.

[42] V.K. Dakua, A. Datta, D. Roy, D. Biswas, B. Ghosh, K. Roy, S. Paul, P. Das, S. Mishra, B. Sinha, M. Das, S. Barman, M.N. Roy, Synthesis, crystal structure, Hirshfeld surface, and DFT studies of a Copper(II) complex of 5,5′-dimethyl-2,2′-bipyridine and 1,2,2-trimethylcyclopentane-1,3-dicarboxylic acid, Results Chem. 6 (2023) 101050. https://doi.org/10.1016/j.rechem.2023.101050.

[43] Philips H Rieger, Electron spin resonance analysis and interpretation, The Royal Society of Chemistry 2007 All, 2015.

[44] V. Baliram T, P. Sanjay K, P. Arvind M, Synthesis, Spectral Characterization and

Antitubercular Study of Novel Quinoline Schiff Base and Its Metal Complexes, Anal. Chem. Lett. 11 (2021) 523–538. https://doi.org/10.1080/22297928.2021.1921616.

[45] P. Chooto, Cyclic Voltammetry and Its Applications, Voltammetry. (2019). https://doi.org/10.5772/intechopen.83451.

[46] A. Abayneh, T. Gebretsadik, S. Tadesse, M. Thomas, Synthesis, Spectroscopic, Structural Characterization, Conductivity and Electrochemical Studies of a Schiff Base Ligand and Its Copper Complexes, Adv. Chem. Eng. Sci. 08 (2018) 241–254. https://doi.org/10.4236/aces.2018.84017.

[47] P.N. Tawakoli, A. Al-Ahmad, W. Hoth-Hannig, M. Hannig, C. Hannig, Comparison of different live/dead stainings for detection and quantification of adherent microorganisms in the initial oral biofilm, Clin. Oral Investig. 17 (2013) 841–850. https://doi.org/10.1007/s00784-012-0792-3.

Published Papers

Contents lists available at ScienceDirect

Journal of Molecular Structure

journal homepage: www.elsevier.com/locate/molstr

Square pyramidal Cu(II) acylpyrazolone complex: Synthesis, characterization, crystal structure, DFT and Hirshfeld analysis, *in-vitro* anti-cancer evaluation

Sapna Barad [a], Kaushalkumar Chaudhari [b], R.N. Jadeja [a,*], H. Roy [b], Duane Choquesillo-Lazarte [c]

[a] Department of Chemistry, Faculty of Science, The Maharaja Sayajirao University of Baroda, Vadodara 390002, India
[b] Department of Zoology, Faculty of Science, The Maharaja Sayajirao University of Baroda, Vadodara 390002, India
[c] Laboratorio de Estudios Cristalograficos, IACT, CSIC Universidad de Granada, Av. De las palmeras 4, Armilla, Granada E 18100, Spain

ARTICLE INFO

Keywords:
HLIB(4-(2,4-dicholoro benzoyl)meta-chloro-phenyl 3-methyl 5-pyrazolone)
MTT(3 [4,5 dimethylthiazol 2 yl] 2–5 Diphenyl tetrazolium bromide
fetal bovine serum(FBS)
Copper(II)complex
DFT(density functional theory)
Electron spin resonance
Anticancer activities
Apoptosis

ABSTRACT

Copper complexes are renowned for their efficiency in the treatment of cancer because of their cytotoxic effect on tumour cells. Using a variety of techniques, including ESI-Mass, NMR, FT-IR, UV–Vis, TG-DTA plots, CV, ESR, Molar conductance, DFT, and Hirshfeld surface analysis, Pyrazolone based HL^1B ligand and $[Cu(HL^1B)_2(DMF)]$ complex were synthesised and characterized. The synthesized copper complex is square pyramidal in nature in which four oxygens of ligand coordinated to central copper metal at an axial position and one oxygen from DMF solvent bind at an equatorial position which can be proved by single crystal analysis. UV–Visible spectroscopy to identify charge transfer and d-d transition in the complex. To evaluate and obtain an excellent correlation with all experimental findings, DFT calculations have been done using the B3LYP/6–31 G basis set. The HOMO-LUMO energy gap, NBO charges, and MESP are useful to confirm the characteristics theoretically and to know the physical and chemical properties of such system. Hirshfeld surface analysis has been done to know the hydrogen bonding and secondary interaction in molecule. Electrochemical analysis such as cyclic voltammograms (CV) provides an idea about the redox behaviour of synthesized copper complexes. To prove the paramagnetic behaviour of a complex ESR/EPR was done at room temperature in a solid state. Using Lung adenocarcinoma (NCI-H23), Hepatocellular carcinoma (HepG2), and Neuroblastoma (SH-SY5Y) cell lines the anticancer activity of a synthesized complex was examined. Scratch assay, Calcein and EthD-1 staining were also used. Moreover, the Inhibition of cell migration using synthesized compound has been evaluated by scratch assay. Apoptotic cell death has been observed by differential staining.

1. Introduction

The transition elements also known as the d-block elements, take up most of the central space of the periodic table those are commonly utilized. Bioinorganic chemistry, materials science, and catalysis, amongst various disciplines, continue to be at the cutting edge of research [1]. So many distinctive qualities that metals possess such as Redox property, different manners of coordination and responsiveness to organic substrates, because of such properties and reactivity, metals are subjected to strict regulation in optimal conditions. Abnormal levels of metal ions are linked to several pathological illnesses, including cancer. Diseases including pernicious anaemia, growth retardation, and heart disease all occur from the lack of iron, zinc, and copper metal ions. Transition metals exhibit a range of oxidation states and interact with the few molecules those are negatively charged. Transition metals having such characteristics encouraged the emergence of metal-based drugs with potential pharmacological applications. Metal complexes can now be used as medicinal agents efficiently owing to developments in inorganic chemistry. Despite having several drawbacks they continue to be used very significantly in medical therapeutics [2].

Chemotherapy is a systemic cancer treatment that is recommended to patients. The discovery of platinum-based drugs which inhibit tumour cell proliferation in the 1960s marked a turning point in the medical development of anticancer drugs. The clinical applications of cisplatin and its derivative drugs are used worldwide. The use of platinum derivatives can be limited due to harmful side effects such as liver, kidney,

* Corresponding author.
E-mail address: rjadeja-chem@msubaroda.ac.in (R.N. Jadeja).

https://doi.org/10.1016/j.molstruc.2023.136345
Received 27 June 2023; Received in revised form 24 July 2023; Accepted 2 August 2023

Inorganica Chimica Acta 576 (2024) 122467

Contents lists available at ScienceDirect

Inorganica Chimica Acta

journal homepage: www.elsevier.com/locate/ica

Research paper

Crystal structure, DFT and Hirshfeld surface analysis of acylpyrazolone based square pyramidal Cu(II) complex: *In-vitro* anticancer activity

Sapna V. Barad [a], Rajendra N. Jadeja [a,*], Ray J. Butcher [b]

[a] Department of Chemistry, Faculty of Science, The Maharaja Sayajirao University of Baroda, Vadodara 390002, India
[b] Department of Inorganic & Structural Chemistry, Howard University, Washington, DC 22031, USA

ARTICLE INFO

Keywords:
Acylpyrazolone-based ligand
Square pyramidal Cu(II) complex
Anticancer activity
Hirshfeld surface analysis
Quantum analysis

ABSTRACT

This study reports the synthesis and comprehensive characterization of a novel Cu(II) complex, [Cu $(HL)_2$(DMSO)], featuring an acylpyrazolone ligand known for its strong σ-donating capability. Extensive structural and spectroscopic analyses were conducted to elucidate the complex's properties and potential applications. Single-crystal X-ray diffraction revealed that the complex adopts a square pyramidal geometry, with the central copper ion coordinated by four oxygen atoms from the acylpyrazolone ligand in a bischelating arrangement, involving both carbonyl and benzoyl carbonyl oxygen atoms. An oxygen atom from a DMSO molecule occupies the apical position, providing additional stabilization. The complex crystallizes in the **monoclinic** crystal system with the $P2_1/c$ space group, offering insights into the ligand arrangement around the copper centre and the electronic environment of the complex. To further support and validate experimental findings, DFT calculations were performed using the B3LYP functional and the LANL2DZ basis set. The optimized geometries showed strong alignment with the experimental structural data. The synthesized complex was characterized through FTIR, UV–Vis, TGA, elemental analysis and cyclic voltammetry techniques, each contributing detailed insights into the complex's electronic structure, thermal behaviour and redox properties. Hirshfeld surface analysis was also employed to examine intermolecular and non-covalent interactions within the crystal lattice. Biological evaluation included *in vitro* cytotoxicity assays against SH-SY5Y (neuroblastoma) cells, where the complex demonstrated significant cytotoxicity, effectively inducing cell death. Comparison with cisplatin, a well-known anticancer drug, revealed that the synthesized compound exhibited superior anticancer activity, underscoring its potential as a more effective therapeutic agent in cancer treatment.

1. Introduction

Copper is essential for bone growth and maintenance, supports the development of connective tissues and plays a crucial role in various enzymatic reactions [1]. After zinc and iron, copper ranks as the third most abundant trace element in the human body. This essential trace element plays a critical role as a catalyst in heme synthesis and iron absorption [1]. Copper-based coordination complexes are promising compounds with potential uses in creating functional materials that exhibit catalytic, optical, conductive, and magnetic properties. Transition metal complexes, including those with copper, are essential in numerous fields including photochemistry, materials science, biological systems, and catalysis [2,3]. Copper compounds exhibit a transition between copper(II) and copper(I) ions, which can generate superoxide and hydroxyl radicals and cause cell death, they are potentially cytotoxic [4].

Coordination complexes have gained a great deal of attention in recent years, where active drugs serve as ligands, particularly within inorganic and medicinal chemistry. Research has focused on exploring the structure-activity relationships of copper complexes with various ligands [5]. Transition metal complexes containing pyrazolone derivatives have garnered significant interest due to their intriguing chemical and physical properties. The study of tautomerism in these compounds is particularly important, as it plays a crucial role in their chemical reactivity. Pyrazoles contain a keto group in position five and an amine group in position four. These compounds and their derivatives are used to produce dihydrotestosterone products that exhibit psychotoxic, antimicrobial, or analgesic properties, and show bioactivity

Abbreviations: DFT, density functional theory; MTT, 3-[4,5-dimethylthiazol-2-yl]-2-5, diphenyl tetrazolium bromide; RB, Round bottom flask.

* Corresponding author.
E-mail address: rjadeja-chem@msubaroda.ac.in (R.N. Jadeja).

https://doi.org/10.1016/j.ica.2024.122467
Received 3 September 2024; Received in revised form 29 October 2024; Accepted 22 November 2024
Available online 23 November 2024

Chapter 3: Part (b)

Acylpyrazolone based square pyramidal Cu(II) complexes: Synthesis, structural characterization, DFT and antiproliferative properties

3b.1 Introduction

Biological activities essential to life processes are linked to transition metals. Transition metals, such as copper, iron and manganese, have structural and functional roles in numerous biological processes, including electron transfer, catalysis and enzyme and protein active sites. Metal complexes can now be used as medicinal agents more effectively because of developments in inorganic chemistry [1]**.** Since the beginning, coordination chemistry has evolved for more than 300 years, establishing a vibrant new science. Its theory has also been consistently improved [2].

Inorganic substances have substantially contributed to the expansion and development of medical science and human health [3]. Complexes containing copper(II) have attracted much interest because of their exceptional biological and catalytic abilities. It has been noticed that copper(II) complexes are frequently more effective as anti-inflammatory medications than the parent ligands themselves [4][5]. Five-membered heterocycles known as pyrazoles are a type of molecule particularly helpful in synthesising organic compounds. They are one of the azole family's most explored categories of chemical substances. They are referred to precisely as antibacterial, antifungal, anticancer, antidepressant, anti-inflammatory, anti-tuberculosis, antioxidant, and antiviral drugs, as well as protein glycation inhibitors [6].

The advantages of pyrazolone-based metal complexes, including their stability, ease of synthesis, modification, and diverse bioactivity, have attracted significant attention [7]**.** Because of their selectivity, flexibility in synthesis and numerous biological uses, Schiff bases have been the subject of a wide range of studies. Multiple medicines and bioactive natural alkaloids contain pyrazolone scaffolds [8,9]. Numerous investigations have looked into the tautomerism of 4-acylpyrazolones. A quick (compared to the NMR timeframe) interconversion of the OH and NH forms in solution results in averaged sets of signals [10]. Due to their antioxidant, antifungal, and anti-HIV properties, these compounds are now often utilised in biochemistry, catalysis and medicine. Because of this, efforts have been undertaken over the past several decades to advance the synthesis and characterization of Cu(II) compounds to understand better the role of copper active sites in diverse catalytic biological processes. More study is being done on these complexes because of their significance in bioinorganic chemistry [11].

One of the areas of pharmaceutical research that is expanding the quickest is the establishment of pharmaceuticals for cancer treatment. It is undeniable that cancer cells are highly proliferative, and as a result, blocking proliferative pathways is seen as an effective

method of combating cancer. The research and discovery of novel, more targeted anticancer drugs have received much attention lately [12]. Cu(II) complexes are considered the most effective cisplatin substitutes currently available, according to many research publications documenting the synthesis [13].

In this study, we present a significant synthetic technique for preparing two acylpyrazolone square pyramidal Cu(II) complexes. The synthesized compounds were analyzed and characterized using various analytical and spectroscopic methods. Their pharmacological activity was evaluated against cancer cells, with both copper complexes exhibiting significant in vitro cytotoxicity.

3b.2 Experimental work

3b.2.1 Materials and Methods

Chapters **2** and **3 (Part a)** described that the required materials were purchased from the listed suppliers. These materials were essential for carrying out the experiments. The synthesis and characterization of the ligands HL^{III} and HL^{IV} were conducted according to the procedures detailed in Chapter **2.** Additionally, the synthesis and characterization of the HL^{IV} ligand were previously published in our laboratory's earlier work [14].

3b.2.2 Synthetic route of complex-3 and complex-4

Both copper complexes, complex-**3** and complex-**4**, were prepared using the same procedure described in Chapter **3a**. Complex-**3** and complex-**4** were recrystallized from hot DMF and DMSO solvents, correspondingly. X-ray quality single crystals of complex-**3** and complex-**4** were obtained in dark green prism-shaped and thick green plate-shaped crystals, respectively. Single-crystal X-ray analysis confirmed that DMF and DMSO solvents sequentially occupy the apical (**5th** coordination) position in complex-**3** and complex-**4**. The synthetic route of both complexes is demonstrated in **Fig.3b.1**. The physical appearances of both complexes are pictured in **Fig.3b.2.**

HL^{III} ligand (0.722g, 0.002 mol), HL^{IV} ligand (0.625g, 0.002 mol) and copper sulphate (0.249g of $CuSO_4.5H_2O$, 0.001mol).

Complex-3: **Colour**: Yellowish green, yield: 78%, M.P:> 200°C, Molecular formula: $C_{36}H_{26}CuCl_4N_4O_4$.DMF **Crystal:** Dark green prism-shaped, **M.W:** 783.974, **Elemental analysis**: C (Exp. 54.97%, Calc.: 54.65%); H (Exp. 3.98%, Calc. 3.88%); N (Exp. 8.90%, Calc. 8.71%); Cu (Exp. 8.00%, Calc.7.98 %), **FTIR (KBr, cm^{-1}):** ν(C=O) of pyrazolone: (1598), ν(C=O) of 2,4-dichloro benzoyl chloride: (1505), cyclic ν(C=N): (1363), **Molar conductance (10^{-3} M DMF):** 3.27 ohm^{-1}cm^{2}mol^{-1}.

Complex-4: **Colour**: Green, yield: 76%, M.P:> 200°C, Molecular formula: $C_{34}H_{24}CuCl_2N_4O_4$.DMSO, **Crystal:** Thick green plate-shaped, **M.W:** 687.031, **Elemental analysis**: C (Exp. 56.79%, Calc.: 56.51%); H (Exp. 4.10%, Calc. 3.95%); N (Exp. 7.56%, Calc. 7.32%); Cu (Exp. 8.04%, Calc. 8.01%), **FTIR (KBr, cm^{-1}):** ν(C=O) of pyrazolone: (1597), ν(C=O) of 4-chloro benzoyl chloride: (1575), cyclic ν(C=N): (1479), **Molar conductance (10^{-3} M DMF):** 3.87 $ohm^{-1}cm^2mol^{-1}$.

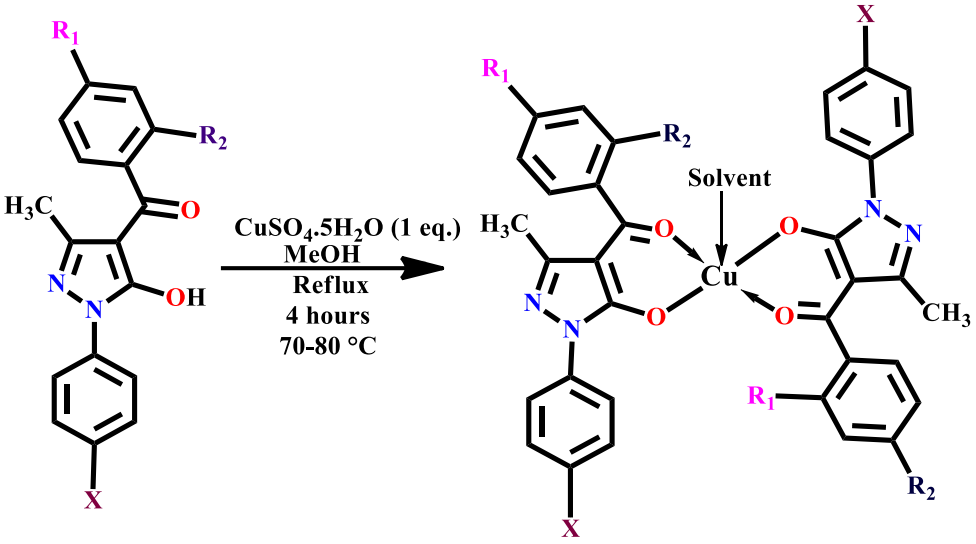

Complex-3: R_1= Cl, R_2= Cl, X= CH_3

Complex-4: R_1= Cl, R_2= H, X = H

Fig.3b.1. Synthetic route of complex-3 and complex-4

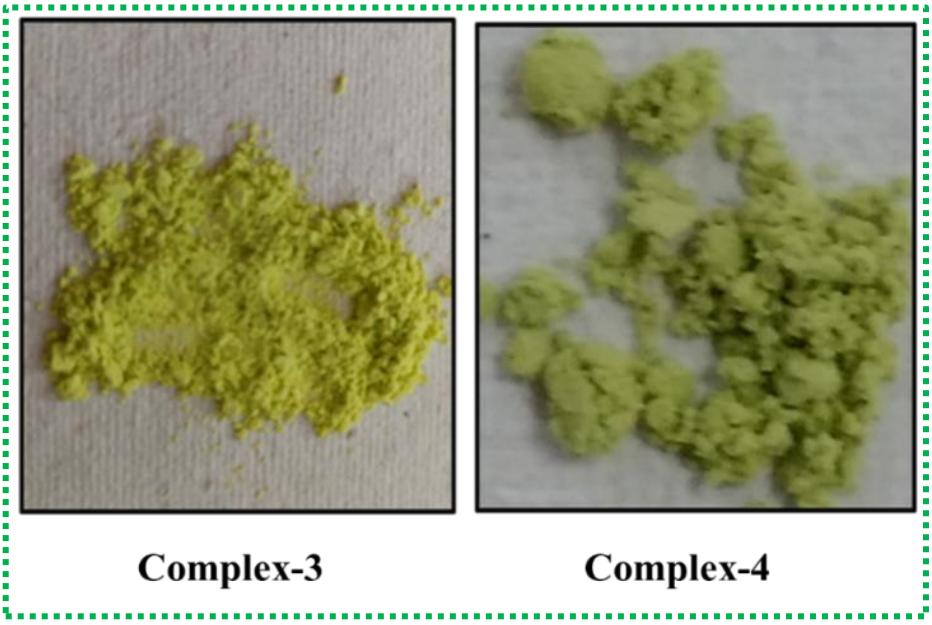

Fig.3b.2. Physical appearance of complex-3 and complex-4

3b.2.3 X-ray crystallographic study

X-ray diffraction data of two copper complexes were collected on the Bruker APEX-II CCD diffractometer. The X-ray crystal structure of both complexes was determined using graphite monochromatized Mo—Kα (λ = 0.71073 Å) radiation at 100(2) K. Recrystallization of complex-**3** and complex-**4** from hot DMF and DMSO correspondingly produced dark green prism-shaped and thick green plate-shaped crystals. The diffraction data were solved using the SHELXT programme [15]. Full-matrix least-squares refinement was carried out using the SHELXL-2018/3 program [16][17]. A micro-focus sealed X-ray tube was taken as a diffraction source. All non-hydrogen atoms of the molecules were located in the expected positions in the obtained structures. Mercury software was employed for the ORTEP views of all three complexes [18].

3b.2.4 Physical measurements and Characterization

Two synthesized copper complexes, complex-**3** and complex-**4,** were characterized using a range of spectroscopic and analytical techniques. Similar methodologies, models, and instruments were used to analyze the data for the synthesized compounds. Techniques such as FTIR, UV-Vis, TG-DTA and ESR were employed following the procedures outlined in Chapter **3a**.

3b.2.5 Computational analysis

Density functional theory (DFT) was utilised to fully optimize the geometry of both complexes by Gauss View 6.0 software. To optimize the structure of the molecules and determine the HOMO-LUMO energies of two complexes, DFT calculations were carried out theoretically. Both complexes underwent comprehensive geometry optimization using the B3LYP/LANL2DZ and B3LYP/6-31G basis sets. A basis set B3LYP/LANL2DZ was used to optimize the copper complexes [19][20][21]. The LANL2DZ basis set is a double-zeta set that does not include polarization functions but accounts for relativistic effects via pseudopotentials [22]. It simplifies the treatment of core electrons through effective core potentials (ECPs), making it particularly well-suited for heavier elements like copper. This basis set is especially advantageous for transition metals and other heavy elements. The HOMO-LUMO energy gap analysis was carried out using these two different basis sets for both complexes. NBO analysis was carried out to characterize the interaction between occupied and unoccupied NBO-type Lewis orbitals [23].

3b.2.6 Anti-cancer activity

The *in vitro* antiproliferative property of both complexes was investigated through the MTT assay, an essential *in vitro* method for evaluating anticancer activity during the early stages of drug discovery. This technique involves testing the compounds on cancer cells cultured outside the body to assess their ability to inhibit cell growth or disrupt crucial cancer-driving pathways. Three cancer cell lines were used in this study: NCI-H23 (lung adenocarcinoma), HepG2 (hepatocellular carcinoma), and SH-SY5Y (neuroblastoma). Complex-**3** was tested across three cell lines, showing the strongest effect against NCI-H23 cancer cells, leading to further focused studies on this line. A 'live/dead assay' was conducted using complex **3** to determine the number of viable and dead cells. A 'scratch assay' was also performed to analyze cell migration and proliferation. In contrast, complex-**4** was tested specifically against SH-SY5Y neuroblastoma cells. Cisplatin served as a reference compound for all assays, and a comparative study was performed to evaluate the efficacy of complex-**3** and complex-**4** compared to cisplatin.

3b.2.6.1 Cell culture conditions

We procured cancer cell lines, NCI-H23 (lung adenocarcinoma), HepG2 (hepatocellular carcinoma), and SH-SY5Y (neuroblastoma) from the National Centre for Cell Science (NCCS), Pune. NCI-H23 cells were cultured in RPMI-1640 medium (Himedia), HepG2 and SH-SY5Y cells were cultured in MEM medium (Himedia) supplemented with 10% fetal bovine serum and 1% penicillin-streptomycin solution (Gibco) at 37 °C under 5% CO_2 condition [24].

3b.2.6.2 MTT- Cell viability assay

Cell viability was assessed using the MTT assay. Cancer cells were seeded in 96-well plates at a density of 7,000 cells per well and allowed to adhere for 24 hours in a cell culture medium. The cells were then treated with various concentrations of Complex-**3** and Complex-**4** for 24 hours in a 37 °C, 5% CO_2 incubator. The SH-SY5Y and NCI-H23 cell lines were also treated with different doses of cisplatin for 24 hours. After the incubation, the cells were washed with PBS and MTT (5 mg/mL) was added to each well, followed by a 4-hour incubation [25]. Formazan crystals were dissolved in DMSO solvent and absorbance was measured at 570 nm using a 'Synergy H1 multi-mode microplate reader'. Optical density (OD) was estimated and used for IC_{50} calculation. The following formula was used to determine the percentage of viable cells: Cell viability is calculated as the following formula (1). IC_{50} values were determined using the GraphPad Prism Software.

Images were taken using an inverted microscope (Olympus EK2) and a 10 MP Aptima CMOS digital camera (AmScope) [26].

(OD of treatment/OD of control) x100 **(1)**

3b.2.6.3 Live/Dead assay

In this assay, a differential staining technique was used to assess cell viability, and the analysis was performed with complex-**3** on the NCI-H23 lung cancer cell line. NCI-H23 cells were seeded at a density of 25,000 cells per well in 8-well chamber slides (ThermoFisher Scientific) and incubated for 24 hr. After exposure to complex-**3** for 24 hr, the cells were stained for 30 minutes with a cytotoxicity kit (Invitrogen) containing 2 µM calcein dye and 4 µM Ethidium homodimer-1 dye (EthD-1). The stained cells were observed under the Nikon-Ti2E fluorescence microscope and ImageJ software quantified cell viability and apoptotic cell death [27][28].

3b.2.6.4 Scratch assay/wound healing assay

The scratch (or wound healing) assay is a widely used technique for studying cell migration. In this experiment, a monolayer of cells was grown to 100% confluence on a 6-well culture plate. A scratch was made using a 200 µL pipette tip. Complex-**3** was applied to NCI-H23 (lung cancer) cells for the study. Photographs of the scratch were taken at 0 hr, 24 hr and 48 hr. Wound closure (%) was calculated using ImageJ software [29].

3b.3 Results and Discussion

In this study, we have synthesized two square pyramidal copper complexes. Both synthesized complexes were characterized using all possible spectroscopic and analytical methods, such as FT-IR, UV-Vis, TGA, ESR, elemental analysis and molar conductance. A computational analysis (DFT) was performed for geometry optimization. Hirshfeld surface analysis was performed to investigate intermolecular interactions and crystal packing in the solid-state structures. Single crystal X-ray diffraction analysis revealed the square pyramidal geometry of complex-**3** and complex-**4**. Both complexes are stable at RT. The copper complexes frequently demonstrate notable anticancer effects attributed to their interaction with biomolecules. Hence, with the help of a cytotoxicity assay, the anticancer efficacy of both complex-**3** and complex-**4** was evaluated. The IC_{50} (half maximal inhibitory concentration) values of both complexes were calculated. Cell death analysis and scratch assay were performed against NCI-H23 (lung adenocarcinoma cells) using complex-**3**.

3b.3.1 FTIR spectral studies

FTIR is an instrumental technique which details the molecular properties of the synthesized copper complexes, providing insights into their chemical behaviour and potential applications. FTIR reveals critical information about the functional groups and molecular structures within the compound by analysing how a sample absorbs infrared light. The FTIR frequencies of the ν(C=O) group in benzoyl chloride and pyrazolone appear at 1505 cm^{-1} and 1598 cm^{-1}, respectively, for complex-**3**. For complex-**4**, the ν(C=O) frequencies of benzoyl chloride and pyrazolone are observed sequentially at 1575 cm^{-1} and 1597 cm^{-1}. A significant shift in IR frequencies occurs during the formation of the metal complex due to the formation of the M-O bond. During complexation, the charge from the O-atom of the C=O group in pyrazolone is transferred to the metal ion, which strengthens the M-O bond and weakens the C=O bond, leading to an increase in the bond length (lower IR frequency) of the pyrazolone C=O bond in the complex than free ligand [30][31]. Other FTIR frequencies are shown in the table below. The FTIR frequencies for complexes **3** and **4** are provided in **Table 3b.1** and the FTIR spectra of complex-**3** and complex-**4** are shown in **Figs.3b.3-3b.4.**

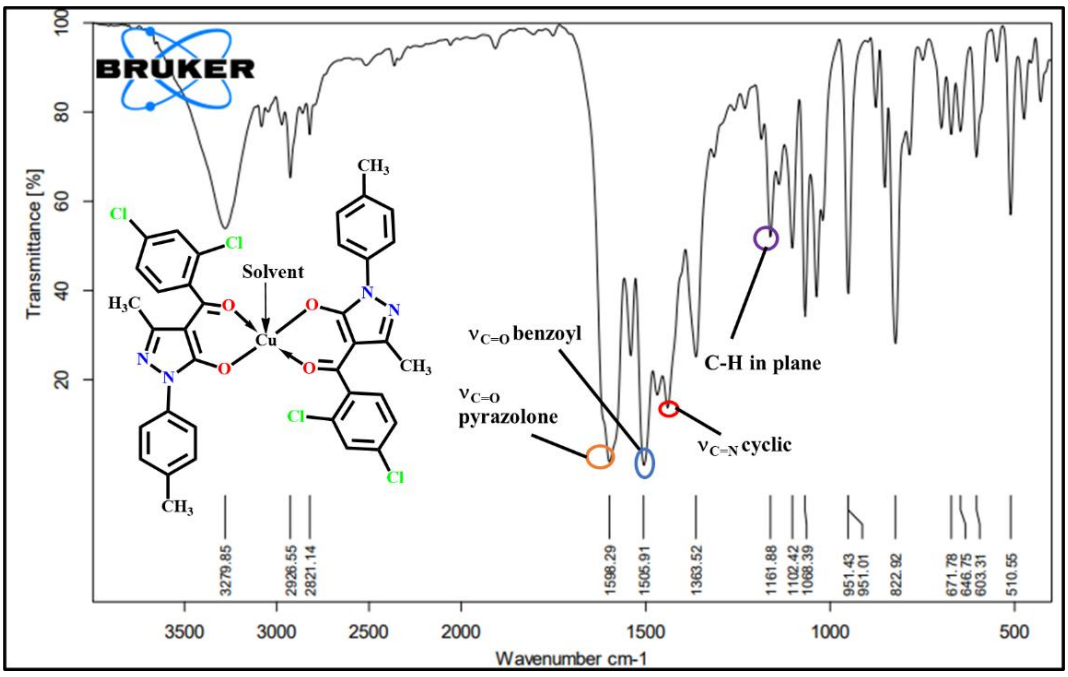

Fig.3b.3. FTIR spectrum of complex-3

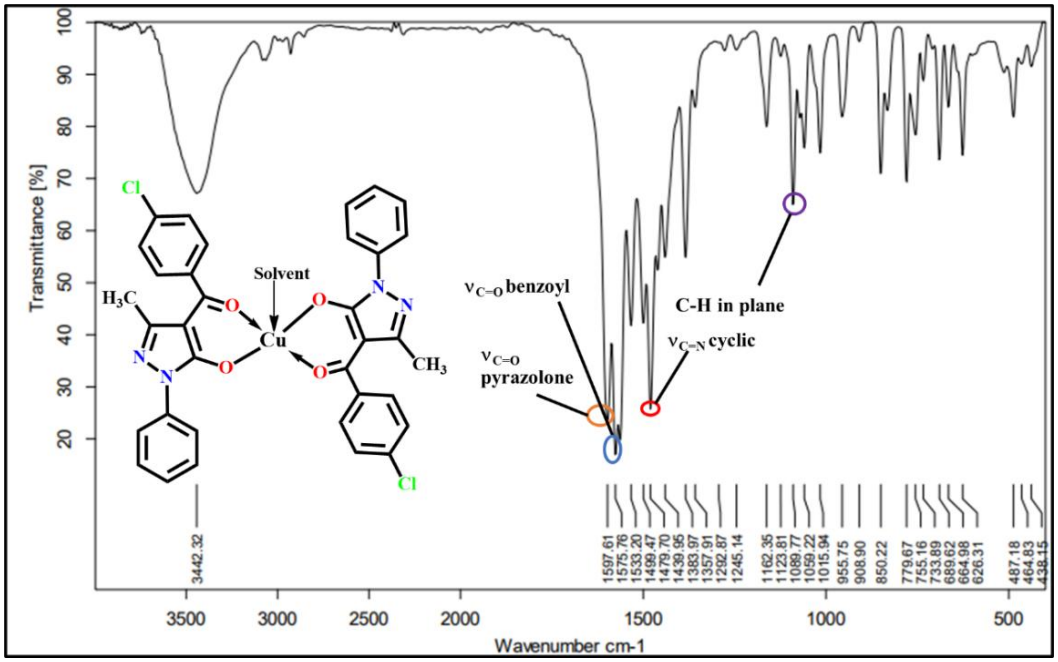

Fig.3b.4. FTIR spectrum of complex-4

Table 3b.1. FTIR spectral data of respective ligands, complexes-3 and complex-4

Code	HL^{III} ligand	Complex-3	HL^{IV} ligand	Complex-4
ν(C=O) of benzoyl chloride	1585	1505	1587	1575
ν(C=O) of Pyrazolone	1668	1598	1619	1597
Cyclic ν(C=N)	1472	1363	1557	1479
C–H in-plane deformation	1253	1161	1213	1162
ν_{M-O}	-	508	-	490

3b.3.2 Thermogravimetric analysis

TGA, or thermogravimetric analysis, explains how a material's mass changes with temperature. The method can evaluate the three-step decomposition of complex-**3** and complex-**4.** The remarkable thermal stability of the complexes can be demonstrated by the thermal decomposition between 100 and 550 °C. Solvent molecule breakdown from an axial position in complex-**3** occurs up to 130°C with a 9.5% loss. Due to the pyrolysis of two ligand molecules, the second degradation happened up to 360°C with a loss of 52.9%. A significant decrease of 0.690 mg/min at 303.4°C resulted in the DTG curve. The resulting CuO residue is stable till 550°C with a loss of 13.1%. Ligand degradation in complex-**4** occurs from 310 °C to 400 °C, with 55.55% loss and a significant decrease of 1.389 mg/min at 333.7°C. CuO residue is stable at 550°. TG-DTA plots of both complexes are depicted in **Figs.3b.5-3b.6.**

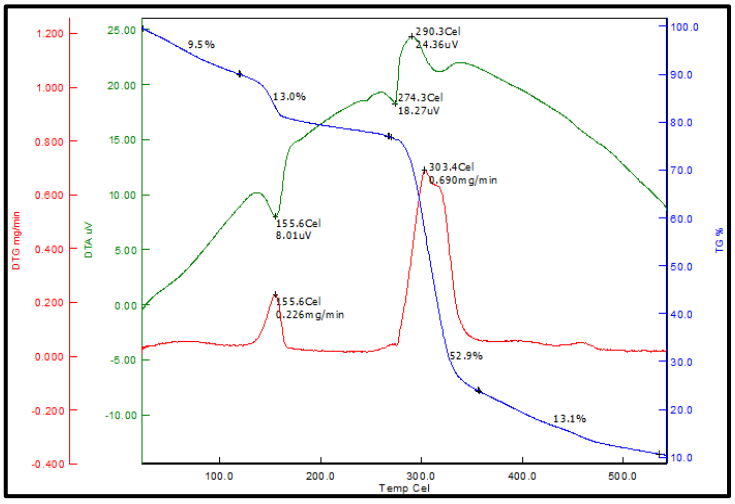

Fig.3b.5. TG-DTA plot of complex-3

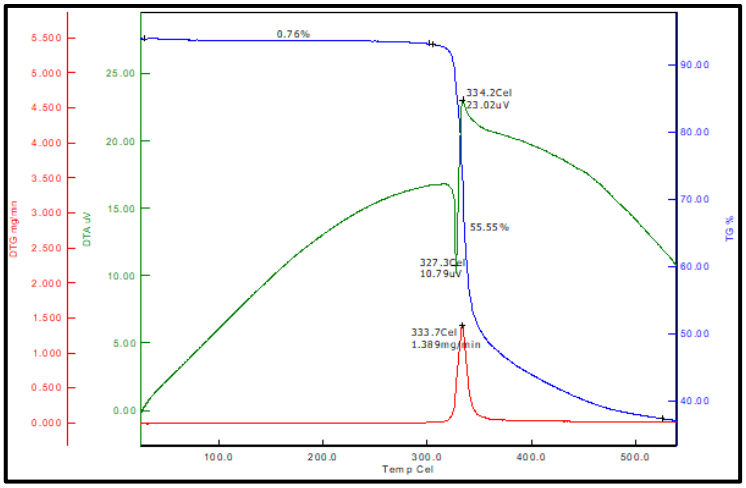

Fig.3b.6. TG-DTA plot of complex-4

3b.3.3 Electronic spectral analysis

UV-visible absorption measurements were conducted on the crystal samples up to 950 nm to determine the energy gap of the copper complexes [32]. The electronic spectra of complex-**3** and complex-**4** were recorded at a concentration of $1x10^{-3}$ M in DMSO solution. The charge transfer spectra were captured using a diluted solution of DMSO. For complex-**3,** the absorption spectra revealed two distinct bands in the ultraviolet region: one at 277 nm (π-π*) and another at 320 nm (n-π*). In contrast, complex-**4** showed absorption bands at 275 nm (π-π*) and 367 nm (n-π*), with the latter lying within the visible spectrum. This transition is due to intra-ligand charge transfer. Additionally, broad bands at 751 nm for complex-**3** and 768 nm for complex-**4** were observed, resulting from the Cu(II) d-d transitions. The molar absorptivity (ε) for complex-**3** at 751 nm was found to be 57.1 M^{-1} cm^{-1}, for complex-**4** at 768 nm, it was 89.1 M^{-1} cm^{-1}. These transitions can be assigned to the $d_{x^2-y^2} \rightarrow d_{xz}$, d_{yz}, and $d_{x^2-y^2} \rightarrow d_{z^2}$ transitions, which are indicative of Jahn-Teller distortion in these complexes [33].

[34][35]. **Figs.3b.7** and **3b.8** display the intra-ligand charge transfer and d-d spectra of both complexes, respectively.

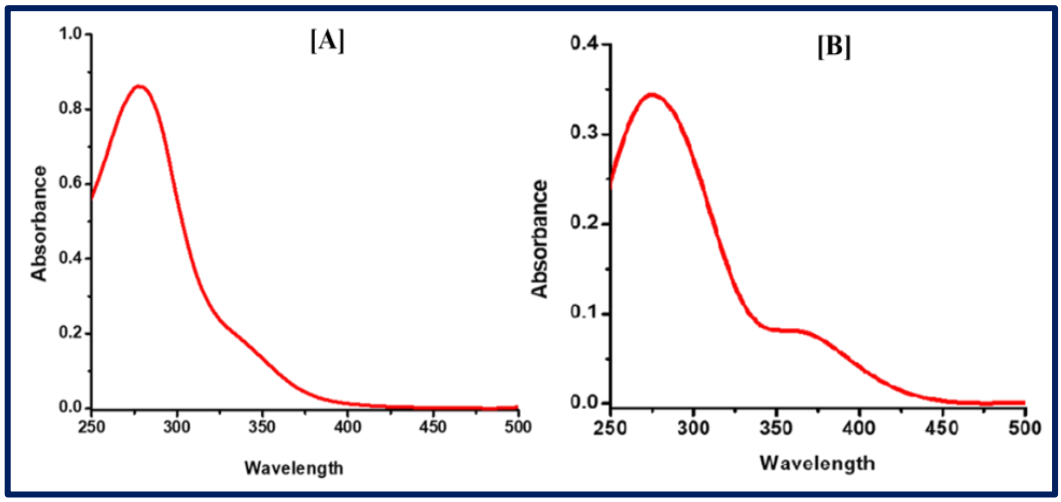

Fig.3b.7. Intra-ligand charge transfer of [A] complex-3 and [B] complex-4 in a diluted solution of DMSO

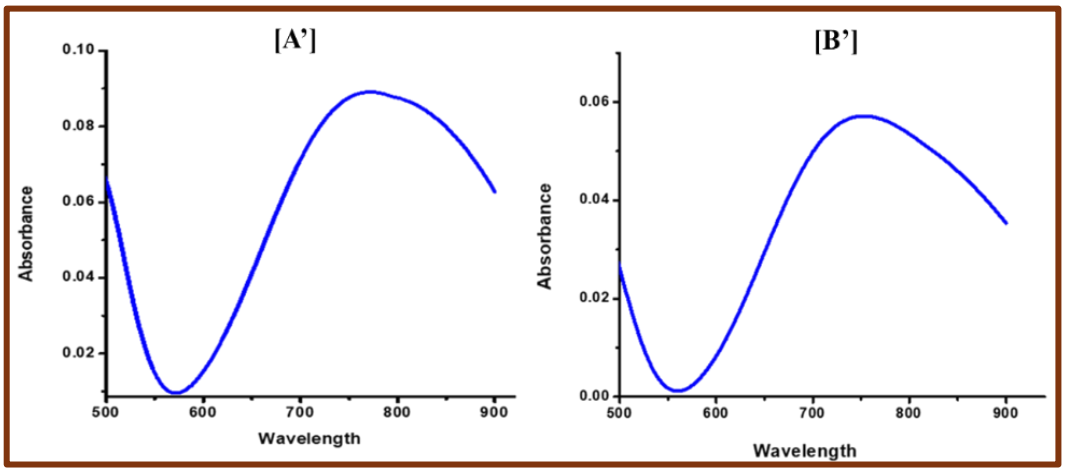

Fig.3b.8. d-d transition of [A'] complex-3 and [B'] complex-4 in a $1x10^{-3}$ M solution of DMSO

3b.3.4 Single crystal X-ray diffraction analysis

After the complexation reaction with acylpyrazolone ligands, the synthesized Cu(II) complexes labelled complex-**3** and complex-**4** were recrystallized in DMF and DMSO solvents, respectively. Thick green crystals of both complexes were obtained. The geometry of the synthesized complexes was determined to be square pyramidal (penta-coordinated), where four oxygen atoms from two ligands occupy the equatorial positions and the fifth position is coordinated by an oxygen atom from a DMF molecule (in complex-**3**) and a DMSO molecule (in complex-**4**). Both complexes crystallized in the '**Monoclinic crystal system**', with complex-**3** belonging to the space group $P2_1/n$ and complex-**4** to $P2_1/c$. Both

$P2_1/n$ and $P2_1/c$ space groups exhibit inversion symmetry because the interaction between their two-fold screw axis ($P2_1$) and their respective glide planes (n or c) leads to a centrosymmetric arrangement in the crystal structures. The symmetry elements of complex-**3** and complex-**4** are pictured in **Fig.3b.11.** The bond length of Cu-O5 in complex-**3** is 2.215(19) Å, while in complex-**4**, the Cu-O5 bond length is 2.243(9) Å. In complex-**3**, the equatorial Cu-O bond lengths are 1.924(17) Å, 1.944(17) Å, 1.927(17) Å, and 1.968(18) Å for Cu-O1, Cu-O2, Cu-O3, and Cu-O4, respectively. Similarly, in complex-**4**, the equatorial Cu-O bond lengths are 1.925(9) Å, 1.984(8) Å, 1.938(8) Å, and 1.948(9) Å for Cu-O1, Cu-O2, Cu-O3, and Cu-O4, respectively. The shorter equatorial bond lengths suggest these bonds are stronger than the apical ones. The coordination geometry around the copper centres is best described as square pyramidal, with a **τ** (tau) value ranging from **0.15 to 0.3**, based on the complexes' equatorial and axial bond angles [36]. According to Jahn-Teller distortion, the longer apical bond lengths (2.215 Å and 2.243 Å for Cu-O5) relative to the equatorial bonds suggest the presence of a z-out Jahn-Teller distortion.

This distortion results in an elongation of the bond along the z-axis. The shorter equatorial bond lengths (ranging from 1.924 Å to 1.984 Å) indicate that the equatorial bonds are stronger. This is due to the greater destabilization of the $d_{x^2-y^2}$ orbital, while the d_{Z^2} orbital becomes more stabilized due to the elongated apical bond [34]. Hence, longer apical bond lengths (Cu-O5) than equatorial bonds indicate this z-out Jahn-Teller effect. In complex-**3**, a HL^{III} ligand coordinates the Cu(II) metal with chelating angles of 93.1(7)° and 94.3(7)° and in complex-**4,** a HL^{IV} ligand coordinates the Cu(II) metal with chelating angles of 82.0(3)° 94.2(3)° with pyrazolone oxygens. Both complexes exhibit stability, attributed to the stronger equatorial bonds. No symmetrical intergrowths were observed during crystal growth, so crystal twinning was not detected. The thermal ellipsoid plot (ORTAP diagram) and perspective view of the packing configuration of complex-**3** are demonstrated in **Fig.3b.9.** While **Fig.3b.10** shows the thermal ellipsoid plot (ORTAP diagram) and perspective view of the packing configuration of complex-**4.** A 2D representation of the single crystal structures of both complexes is shown in **Fig.3b.12.** The bond lengths, bond angles parameters, hydrogen bond parameters and symmetry transformations of complex-**3** are listed in **Tables 3b.2-3b.4,** respectively. Similar data for complex-**4** are provided in **Table 3b.5-3b.7**, respectively. All the refinement parameters and crystal data of both complexes are listed in **Table 3b.8.**

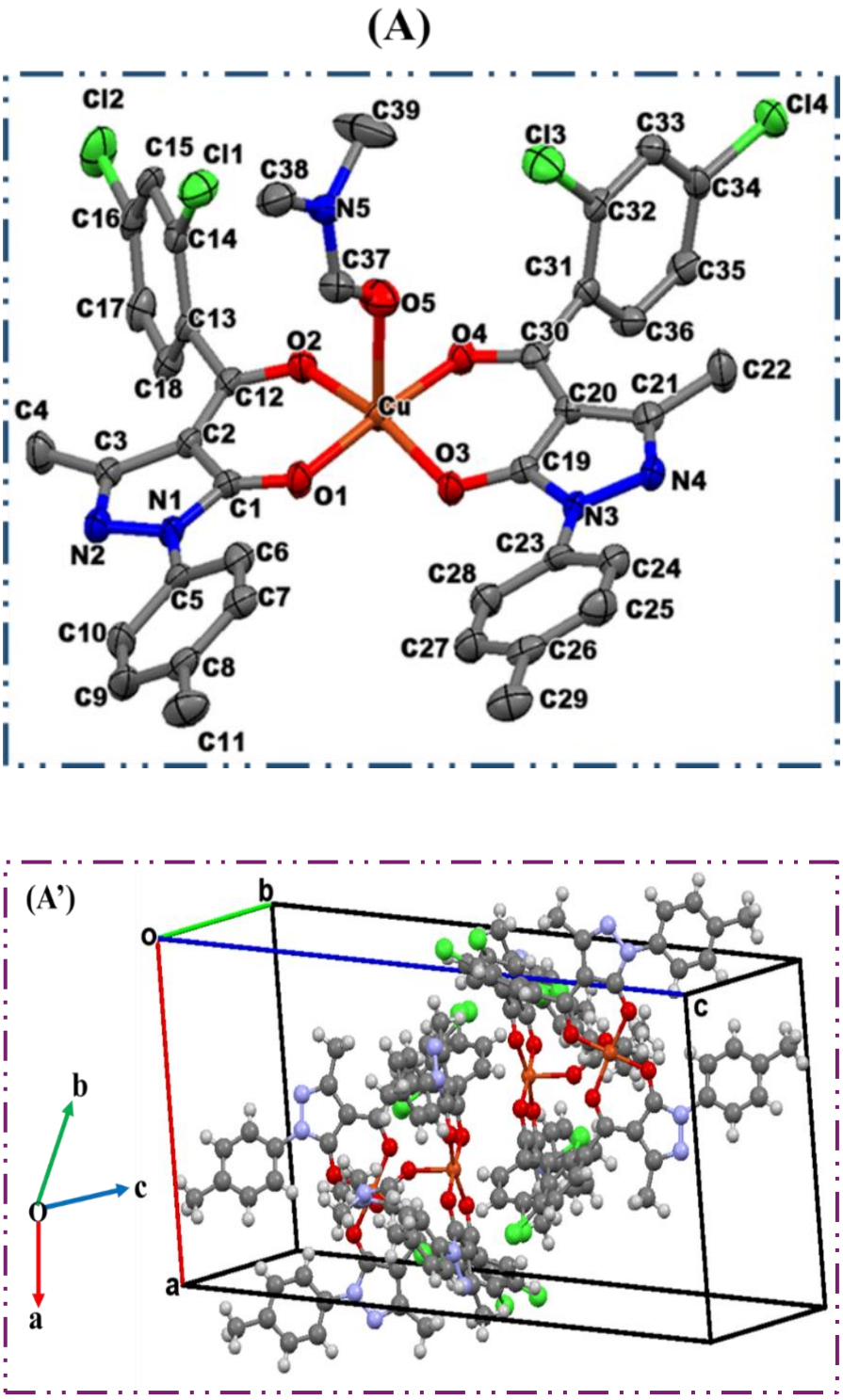

Fig.3b.9. Complex-3: (A)= Thermal ellipsoid plot with 50% probability of complex-3 (Hydrogen atoms omitted for clarity) and (A')= A perspective view of crystal packing plot of complex-3 along b-axis

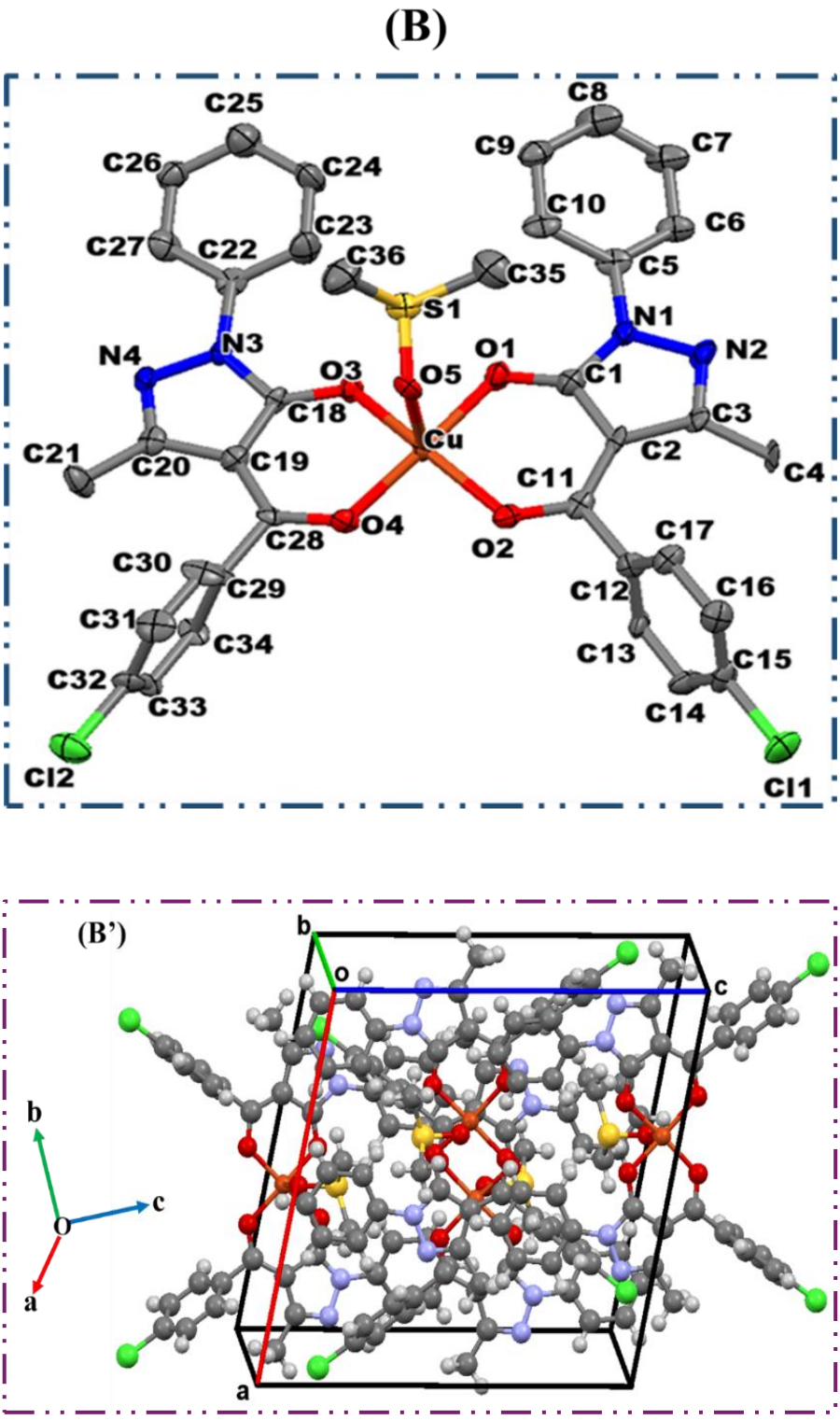

Fig.3b.10. Complex-4: (B)= Thermal ellipsoid plot with 50% probability of complex-4 (Hydrogen atoms omitted for clarity) and (B')= A perspective view of crystal packing plot of complex-4 along b-axis

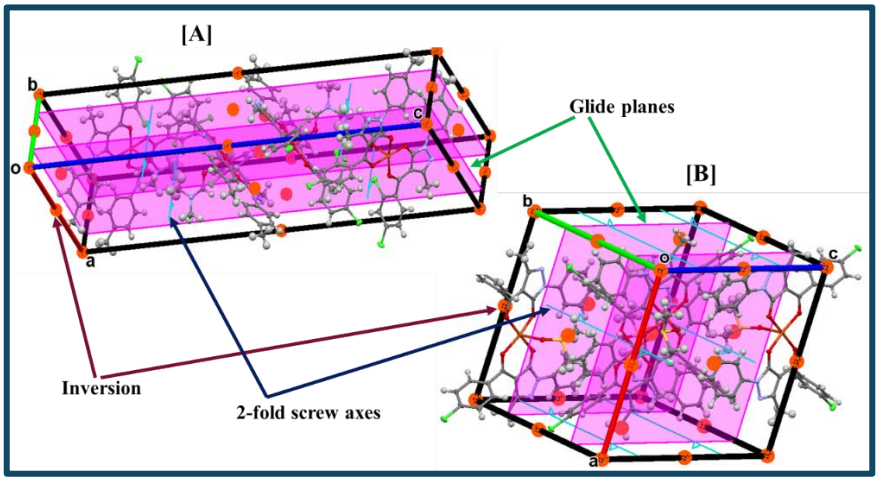

Fig.3b.11. Symmetry elements of [A] complex-3 and [B] complex-4

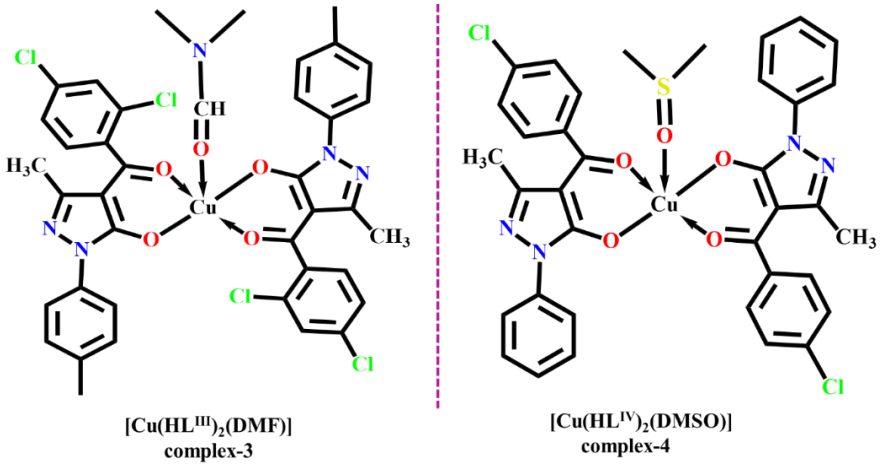

Fig.3b.12. 2D representation of the single crystal structures of complex-3 and complex-4

Table 3b.2 Bond lengths & Bond angles parameters of complex-3

Atoms	Bond lengths (Å)	Atoms	Bond lengths (Å)	Atoms	Bond angles (°)	Atoms	Bond angles (°)
Cu(1)-O(1)	1.924(1)	N(1)-C(1)	1.355(3)	O(1)-Cu-O(3)	83.86(7)	C(13)-C(14)-Cl(1)	119.9(2)
Cu(1)-O(2)	1.945(1)	N(1)-N(2)	1.410(3)	O(1)-Cu-O(2)	93.14(7)	C(15)-C(14)-Cl(1)	119.0(2)
Cu(1)-O(3)	1.927(1)	N(1)-C(5)	1.428(3)	O(3)-Cu-O(2)	166.84(8)	C(15)-C(16)-Cl(2)	119.1(2)
Cu(1)-O(4)	1.968(1)	N(2)-C(3)	1.310(3)	O(1)-Cu-O(4)	176.01(8)	C(17)-C(16)-Cl(2)	119.4(2)
Cu(1)-O(5)	2.215(1)	N(3)-C(19)	1.363(3)	O(3)-Cu-O(4)	94.35(7)	C(33)-C(32)-Cl(3)	119.0(2)
Cl(1)-C(14)	1.738(3)	N(3)-N(4)	1.403(3)	O(2)-Cu-O(4)	87.81(7)	C(31)-C(32)-Cl(3)	119.6(2)
Cl(2)-C(16)	1.741(3)	N(3)-C(23)	1.424(3)	O(3)-Cu-O(5)	97.99(8)	C(33)-C(34)-Cl(4)	119.4(2)
Cl(3)-C(32)	1.738(3)	N(4)-C(21)	1.308(3)	O(2)-Cu-O(5)	95.06(8)	C(35)-C(34)-Cl(4)	119.3(2)
Cl(4)-C(34)	1.736(3)	N(5)-C(37)	1.321(3)	O(4)-Cu-O(5)	88.10(7)	C(1)-N(1)-N(2)	111.7(2)
O(1)-C(1)	1.271(3)	N(5)-C(38)	1.446(4)	C(1)-O(1)-Cu	122.49(16)	C(1)-N(1)-C(5)	128.2(2)
O(2)-C(12)	1.274(3)	N(5)-C(39)	1.448(4)	C(12)-O(2)-Cu	128.31(17)	N(2)-N(1)-C(5)	119.9(2)
O(3)-C(19)	1.271(3)	C(1)-C(2)	1.427(3)	C(19)-O(3)-Cu	120.52(15)	C(3)-N(2)-N(1)	106.0(2)
O(4)-C(30)	1.271(3)	C(2)-C(3)	1.442(3)	C(30)-O(4)-Cu	124.93(16)	O(1)-C(1)-N(1)	123.5(2)
O(5)-C(37)	1.228(3)	C(8)-C(11)	1.508(4)	C(37)-O(5)-Cu	126.06(18)	O(1)-C(1)-C(2)	130.4(2)

Table 3b.3. Hydrogen bond parameters of complex-3

D-H...A	d(D-H)	d(H...A)	d(D...A)	<(DHA)
C(6)-H(6A)...O(1)	0.95	2.27	2.866(3)	120.1
C(15)-H(15A)...Cl(4)#1	0.95	2.88	3.730(3)	149.9
C(28)-H(28A)...O(3)	0.95	2.28	2.871(3)	120.0
C(38)-H(38A)...O(2)#2	0.98	2.34	3.298(3)	167.1
C(39B^b)-H(39F^b)...Cl(3)	0.98	2.91	3.707(17)	139.5

Table 3b.4. Complex-3: Symmetry transformations used to generate equivalent atoms

	Symmetry transformations
1	-x+3/2, y-1/2,-z+1/2
2	x, y-1, z

Table 3b.5. Bond lengths & Bond angles parameters of complex-4

Atoms	Bond lengths (Å)	Atoms	Bond lengths (Å)	Atoms	Bond angles (°)	Atoms	Bond angles (°)
Cu(1)-O(1)	1.926(9)	N(1)-C(1)	1.348(16)	O(1)-Cu-O(3)	82.0(3)	C(35)-S(1)-C(36)	96.5(7)
Cu(1)-O(2)	1.938(8)	N(1)-N(2)	1.408(15)	O(1)-Cu-O(4)	175.0(3)	C(1)-O(1)-Cu	122.4(8)
Cu(1)-O(3)	1.948(9)	N(1)-C(5)	1.423(15)	O(3)-Cu-O(4)	94.2(3)	C(11)-O(2)-Cu	126.6(8)
Cu(1)-O(4)	1.984(8)	N(2)-C(3)	1.339(16)	O(1)-Cu-O(2)	93.8(3)	C(18)-O(3)-Cu	120.5(7)
Cu(1)-O(5)	2.243(9)	N(3)-N(4)	1.390(14)	O(3)-Cu-O(2)	165.2(3)	C(28)-O(4)-Cu	127.0(7)
S(1)-O(5)	1.508(8)	N(3)-C(18)	1.392(14)	O(4)-Cu-O(2)	89.2(3)	S(1)-O(5)-Cu	114.6(5)
S(1)-O(35)	1.774(15)	N(3)-C(22)	1.413(14)	O(1)-Cu-O(5)	88.9(7)	O(1)-C(1)-N(1)	124.6(11)
S(1)-O(36)	1.793(14)	N(4)-C(20)	1.297(15)	O(3)-Cu-O(5)	94.8(7)	O(1)-C(1)-C(2)	130.1(12)
C(1)-O(1)	1.260(16)	C(1)-C(2)	1.442(17)	O(4)-Cu-O(5)	94.6(7)	N(2)-N(1)-C(5)	116.3(10)
C(11)-O(2)	1.248(15)	C(30)-C(31)	1.391(18)	O(2)-Cu-O(5)	99.4(7)	N(4)-N(3)-C(22)	120.1(10)
C(18)-O(3)	1.288(14)	Cl(1)-C(15)	1.735(12)	O(5)-S(1)-O(35)	108.4(6)	C(1)-N(1)-N(2)	113.6(10)

Table 3b.6. Hydrogen bonds of complex-4

D-H...A	d(D-H)	d(H...A)	d(D...A)	<(DHA)
C(10)-H(10A)...O(1)	0.95	2.37	2.951(16)	119.2
C(16)-H(16A)...N(2)#1	0.95	2.59	3.275(16)	129.4
C(23)-H(23A)...O(3)	0.95	2.26	2.899(15)	123.7
C(35)-H(35C)...O(2)#2	0.98	2.63	3.607(17)	172.5

Table 3b.7. Complex-4: Symmetry transformations used to generate equivalent atoms

	Symmetry transformations
1	x,-y+1/2,z+1/2
2	x,-y+1/2,z-1/2

Table 3b.8. Refinement parameters of complex-3 and complex-4

CODE	$[Cu(HL^{III})_2DMF]$ Complex-3	$[Cu(HL^{IV})_2DMSO]$ Complex-4
CCDC number	2281710	2281711
Chemical formula	$C_{39}H_{33}CuCl_4N_5O_5$	$C_{36}H_{30}CuCl_2N_4O_5S$
Formula weight	857.04	765.14
Crystal system	Monoclinic	Monoclinic
Space group	$P2_1/n$	$P2_1/c$
Temperature	100(2) K	100(2) K
Wavelength	0.71073 Å	0.71073 Å
Z	4	4
Density	1.495 Mg/m^3	1.518 Mg/m^3
Volume	3807.3(9) $Å^3$	3402.2(15) $Å^3$
Unit cell dimension	a= 13.9750(17) Å b= 6.8795(9) Å c= 39.669(5) Å	a= 14.415(4) Å b= 16.478(4) Å c= 14.620(4) Å
	α,γ = 90° β=93.355(6)°	α,γ = 90° β= 101.557(8)°
F (0 0 0)	1756	1572
Theta range	2.057 to 26.481°	2.193 to 25.252°
R(int)	0.0887	0.1950
Absorption Correction	None	None
Index ranges	-17<=h<=17, -8<=k<=8, -49<=l<=49	-14<=h<=17, -19<=k<=19, -17<=l<=17
Reflections collected	65361	46441
Refinement method	Full-matrix least-squares on F^2	Full-matrix least-squares on F^2
Goodness-of-fit on F^2	1.024	1.518
Final R indices [I>2sigma(I)]	R1 = 0.0412, wR2 = 0.0896	R1 = 0.1348, wR2 = 0.3642
Data/restraints/parameters	7767 / 0 / 493	6143 / 413 / 447
Largest diff. Peak and hole	0.373 and -0.662 $e.Å^{-3}$	3.028 and -1.011 $e.Å^{-3}$

3b.3.5 DFT based computational analysis

DFT study was utilized to assess the electronic structure and refine the geometries of the copper complexes. This computational approach offers important information regarding the complexes' bonding, energy levels and stability, enhancing the results obtained from experimental methods. A B3LYP/LANL2DZ basis set was utilized to optimize the copper complexes [19][21]. In addition to this basis set, the geometries of both complexes were also computed using the B3LYP/6-31G basis set [37][38]. The GaussView 6.0 software was employed to process the input files for both complexes. The optimization energies for complex-**3** and complex-**4** were observed at -65.6225 keV and -60.4222 keV, respectively, when using the B3LYP/LANL2DZ basis set. However, a notable change in optimization energy was observed when applying the B3LYP/6-31G basis set, with values of -139.7153 keV and -134.5150 keV for complex-**3** and complex-**4**, respectively. The optimization energies calculated for the copper complexes reveal significant differences based on the choice of basis set. This variation can be attributed to several factors, including the level of theory, stability and electronic configuration, and the nature of the basis sets. The B3LYP/LANL2DZ basis set utilizes effective core potentials (ECPs) tailored for transition metals like copper, providing a more precise representation of electron interactions near the metal center [39][21]. Conversely, the 6-31G basis set does not incorporate ECPs, which may limit its ability to accurately reflect the electronic behaviour of transition metals. Interestingly, the more negative energy value observed with the 6-31G basis set suggests greater stability in the electronic configuration of the copper complexes in this case. This may imply that the 6-31G basis set facilitates a more favourable distribution of electrons or geometric arrangement, despite its potential shortcomings in accurately describing transition metal characteristics. In summary, the variations in optimization energies observed between the two basis sets emphasize the importance of choosing the right computational method for the specific elements and interactions involved in the study. The B3LYP/LANL2DZ basis set is beneficial for its precision in modelling transition metals [20], while the 6-31G basis set demonstrates the flexibility and usefulness of alternative computational techniques in providing valuable insights. These differences highlight the need for thorough computational investigations, which can deepen our understanding of the stability and electronic characteristics of copper complexes, thereby informing future research and applications in coordination chemistry. The optimization energy value of both copper complexes is highly negative compared to that of respective ligands (Chapter **2**), which shows the stability of the

synthesized complexes over ligands. DFT analysis of ligands has already been stated in Chapter **2**. **Fig.3b.13** represents the optimized geometry of complex-**3** and complex-**4**.

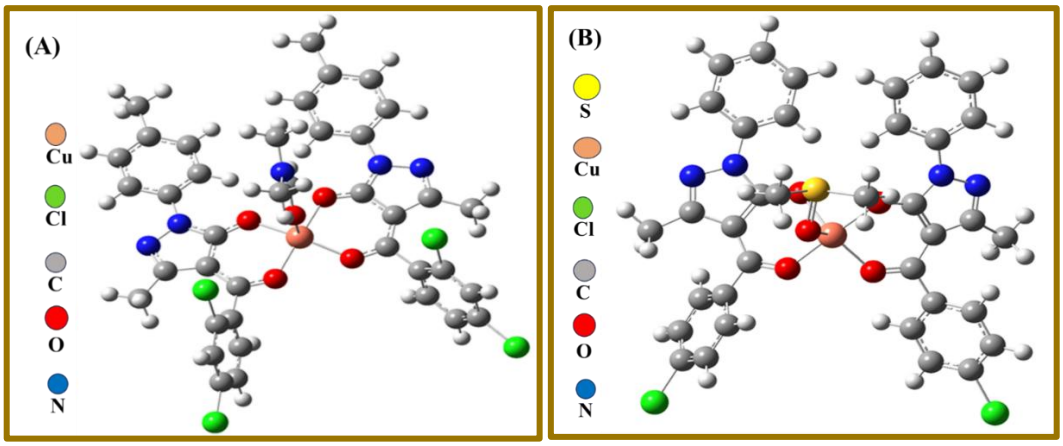

Fig.3b.13. DFT optimized Structures of (A) complex-3 and (B) complex-4

The HOMO-LUMO energies are crucial in determining the number of chemical interactions [40]. HOMO-LUMO analysis provides insights into the nature of a molecule, such as its hardness, softness, and reactivity. One theoretical method for estimating excitation energies involves calculating the difference between the lowest unoccupied molecular orbital (LUMO) and the highest occupied molecular orbital (HOMO) of a system. A reduction in the HOMO-LUMO energy gap highlights the charge transfer interactions within the molecule, reflecting the electron-accepting capacity of the acceptor group. The energy difference between the HOMO and LUMO directly influences a molecule's kinetic stability, chemical reactivity, optical polarizability, and hardness or softness. By analyzing the composition of these orbitals, we can estimate molecular properties that affect a compound's selectivity and reactivity. These properties can be approximated using Koopmans' theorem, which links HOMO and LUMO energies to ionization energy and electron affinity [41]. According to computational studies, the band gap (ΔE) for complex-**4** using the 6-31G basis set is found to be **3.612 eV,** while it is **3.846 eV** using the LANL2DZ basis set. For complex-3, the band gap (ΔE) is calculated as **3.941 eV** with the 6-31G basis set and **3.937 eV** with the LANL2DZ basis set. By analyzing the band gap values of both complexes, it can be concluded that there is minimal difference between the energy gaps. Consequently, both complexes are considered stable due to their relatively small energy gaps. The presence of an unpaired electron in HOMO supports the paramagnetic characteristic of both square pyramidal copper complexes.

Additionally, global parameters of copper complexes could be further anticipated by energy gap ΔE. The six frontier molecular orbitals (FMOs) and HOMO-LUMO energy

diagram of complex-**3** and complex-**4** using B3LYP level LANL2DZ and 6-31G basis set are shown in **Fig.3b.14** and **Fig.3b.15**, respectively. Global parameters for complex-**3** and complex-**4** are presented in **Tables 3b.9 and 3b.10,** respectively. **Table 3b.11** shows a comparison of the practical and theoretical bond parameters.

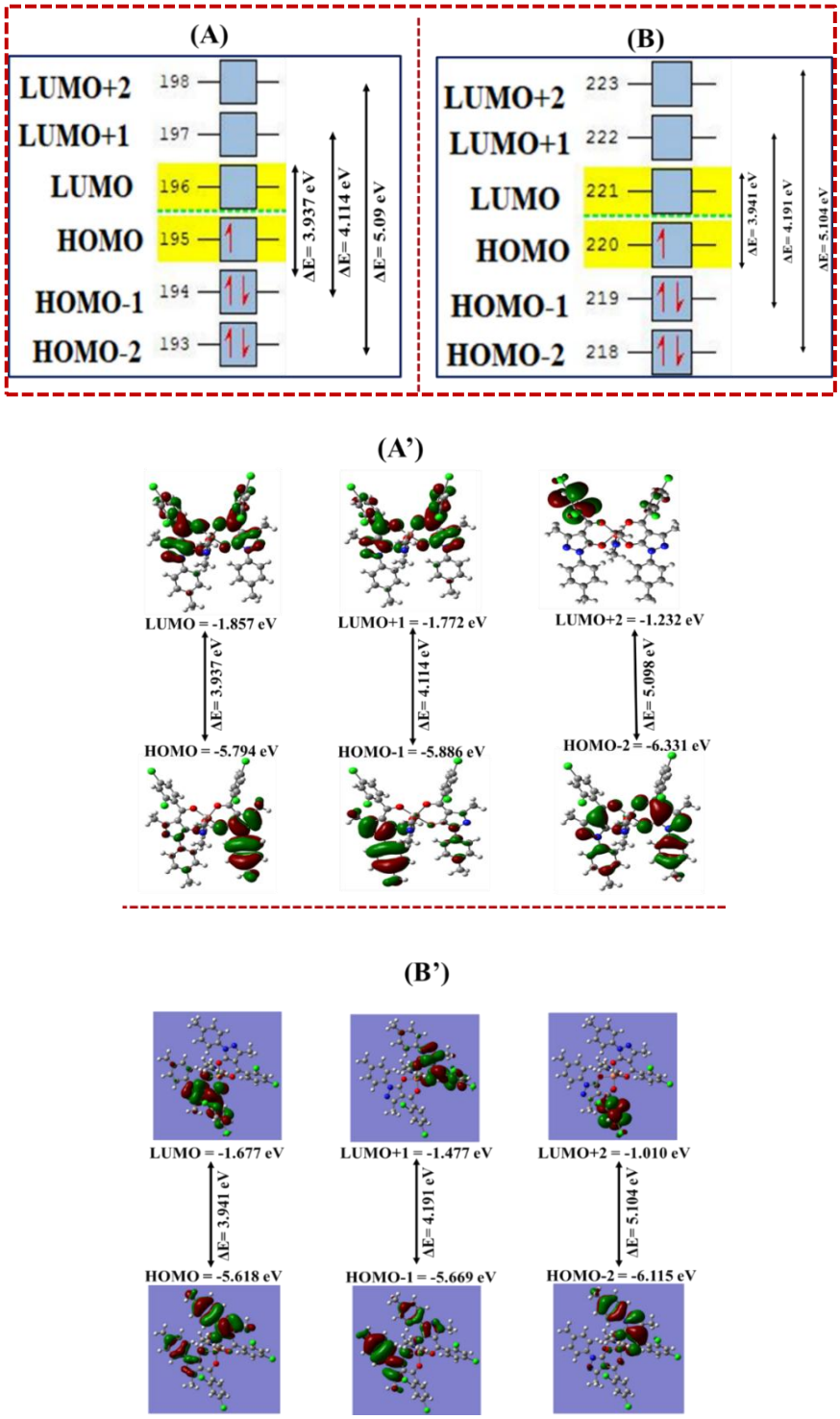

Fig.3b.14. HOMO-LUMO frontier orbital analysis energy molecular diagram of complex-3 using B3LYP/LanL2DZ (A &A') and B3LYP/6-31G (B &B') basis set, respectively

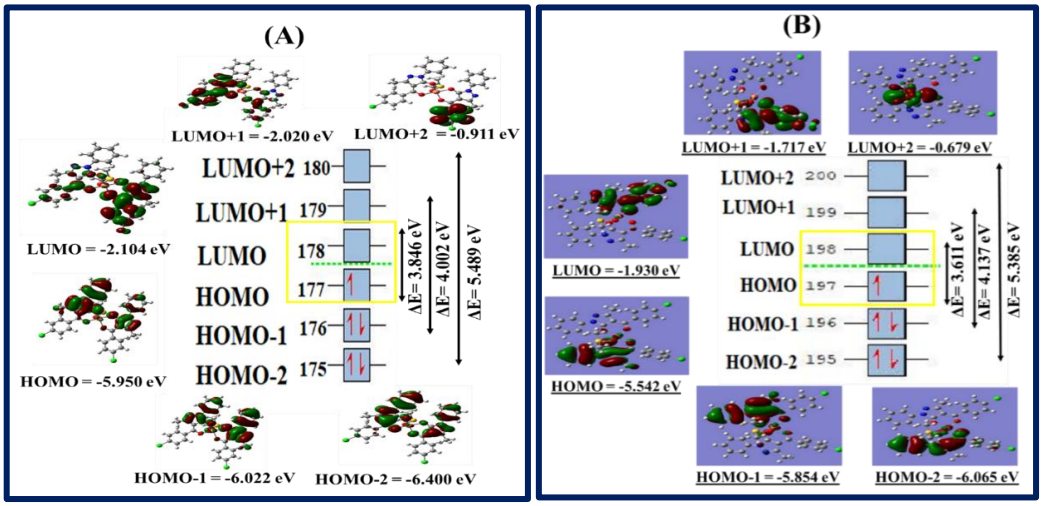

Fig.3b.15. HOMO-LUMO frontier orbital analysis energy molecular diagram of complex-4 using B3LYP/LanL2DZ (A) and B3LYP/6-31G (B) basis set, respectively

Table 3b.9. Global parameters of complex-3

Properties	Mathematical formula	Complex-3 (6-31G)	Complex-3 (LANL2DZ)
E_{HOMO}	E_{HOMO}	-5.618	-5.794
E_{LUMO}	E_{LUMO}	-1.677	-1.857
ΔE	$\Delta E = E_{LUMO} - E_{HOMO}$	3.941	3.937
Ionization potential (IP)	$IP = -E_{HOMO}$	5.618	5.794
Chemical Potential (μ)	$\mu = 1/2 (E_{HOMO} + E_{LUMO})$	-3.647	-3.825
Electron affinity (EA)	$EA = -E_{LUMO}$	1.677	1.857
Electronegativity (EN)	$EN = -1/2 (E_{HOMO} + E_{LUMO})$	3.647	3.825
Global Hardness (Ƞ)	$\eta = -1/2 (E_{HOMO} - E_{LUMO})$	1.970	1.968
Softness (S)	$S = 1/2\eta$	0.127	0.254
Electrophilicity index (ω)	$\omega = \mu^2/2\eta$	3.375	3.717

Table 3b.10. Global parameters of complex-4

Properties	Mathematical formula	Complex-4 (6-31G)	Complex-4 (LANL2DZ)
E_{HOMO}	E_{HOMO}	-5.542	-5.950
E_{LUMO}	E_{LUMO}	-1.930	-2.104
ΔE	$\Delta E = E_{LUMO} - E_{HOMO}$	3.612	3.846
Ionization potential (IP)	$IP = -E_{HOMO}$	5.542	5.950
Chemical Potential (μ)	$\mu = 1/2 (E_{HOMO} + E_{LUMO})$	-3.736	-4.027
Electron affinity (EA)	$EA = -E_{LUMO}$	1.930	2.104
Electronegativity (EN)	$EN = -1/2 (E_{HOMO} + E_{LUMO})$	3.736	1.923
Global Hardness (Ƞ)	$\eta = -1/2 (E_{HOMO} - E_{LUMO})$	1.806	4.027
Softness (S)	$S = 1/2\eta$	0.276	0.124
Electrophilicity index (ω)	$\omega = \mu^2/2\eta$	3.864	2.013

Table 3b.11. A comparison of the practical and theoretical bond parameters

Atoms	Practical bond length (Å)	Theoretical bond length (Å)	Atoms	Practical bond angles (°)	Theoretical bond angles (°)
[Cu(HL^{III})$_2$DMF] complex-3					
Cu(1)-O(1)	1.924(1)	1.981	O(1)-Cu-O(3)	83.86(7)	87.86
Cu(1)-O(2)	1.945(1)	1.993	O(1)-Cu-O(2)	93.14(7)	90.80
Cu(1)-O(3)	1.927(1)	1.979	O(3)-Cu-O(2)	166.84(8)	163.79
Cu(1)-O(4)	1.968(1)	1.979	O(1)-Cu-O(4)	176.01(8)	173.89
Cu(1)-O(5)	2.215(1)	2.230	O(3)-Cu-O(4)	94.35(7)	91.35
Cl(1)-C(14)	1.738(3)	1.819	O(2)-Cu-O(4)	87.81(7)	88.25
Cl(2)-C(16)	1.741(3)	1.816	O(3)-Cu-O(5)	97.99(8)	91.93
Cl(3)-C(32)	1.738(3)	1.820	O(2)-Cu-O(5)	95.06(8)	87.86
Cl(4)-C(34)	1.736(3)	1.830	O(4)-Cu-O(5)	88.10(7)	90.13
O(1)-C(1)	1.271(3)	1.301	C(1)-O(1)-Cu	122.49(16)	124.15
O(2)-C(12)	1.274(3)	1.298	C(12)-O(2)-Cu	128.31(17)	130.04
O(3)-C(19)	1.271(3)	1.300	C(19)-O(3)-Cu	120.52(15)	123.52
O(4)-C(30)	1.271(3)	1.300	C(30)-O(4)-Cu	124.93(16)	129.32
O(5)-C(37)	1.228(3)	1.266	C(37)-O(5)-Cu	126.06(18)	123.21
[Cu(HL^{IV})$_2$DMSO] complex-4					
Cu(1)-O(1)	1.926(9)	1.979	O(1)-Cu-O(3)	82.0(3)	88.57
Cu(1)-O(2)	1.938(8)	1.985	O(1)-Cu-O(4)	175.0(3)	180.01
Cu(1)-O(3)	1.948(9)	1.972	O(3)-Cu-O(4)	94.2(3)	95.55
Cu(1)-O(4)	1.984(8)	1.979	O(1)-Cu-O(2)	93.8(3)	96.76
Cu(1)-O(5)	2.243(9)	2.251	O(3)-Cu-O(2)	165.2(3)	170.75
S(1)-O(5)	1.508(8)	1.709	O(4)-Cu-O(2)	89.2(3)	92.54
S(1)-O(35)	1.774(15)	1.846	O(1)-Cu-O(5)	88.9(7)	90.13
S(1)-O(36)	1.793(14)	1.876	O(3)-Cu-O(5)	94.8(7)	95.55
C(1)-O(1)	1.260(16)	1.302	O(4)-Cu-O(5)	94.6(7)	95.89
C(11)-O(2)	1.248(15)	1.299	O(2)-Cu-O(5)	99.4(7)	105.24
C(18)-O(3)	1.288(14)	1.304	O(5)-S(1)-O(35)	108.4(6)	110.12
C(28)-O(4)	1.267(15)	1.301	O(5)-S(1)-O(36)	105.5(6)	110.25
N(1)-C(1)	1.348(16)	1.383	C(18)-O(3)-Cu	120.5(7)	125.90
N(1)-N(2)	1.408(15)	1.424	C(28)-O(4)-Cu	127.0(7)	130.53
N(1)-C(5)	1.423(15)	1.423	S(1)-O(5)-Cu	114.6(5)	120.54

Theoretical IR frequencies were obtained using DFT calculations after the complete optimization. Theoretical vibrations can be used to investigate the changes which occur during complexation. The optimized geometries of both complexes were used as inputs for vibrational frequency analysis. After achieving convergence, harmonic vibrational frequencies were calculated at the same theoretical level to confirm that the stationary points did not show any imaginary frequencies. Key theoretical vibrational frequencies and the corresponding experimental FTIR values are provided in **Table 3b.12.** The DFT-optimized IR spectra are pictured in **Figs.3b.16–3b.17.**

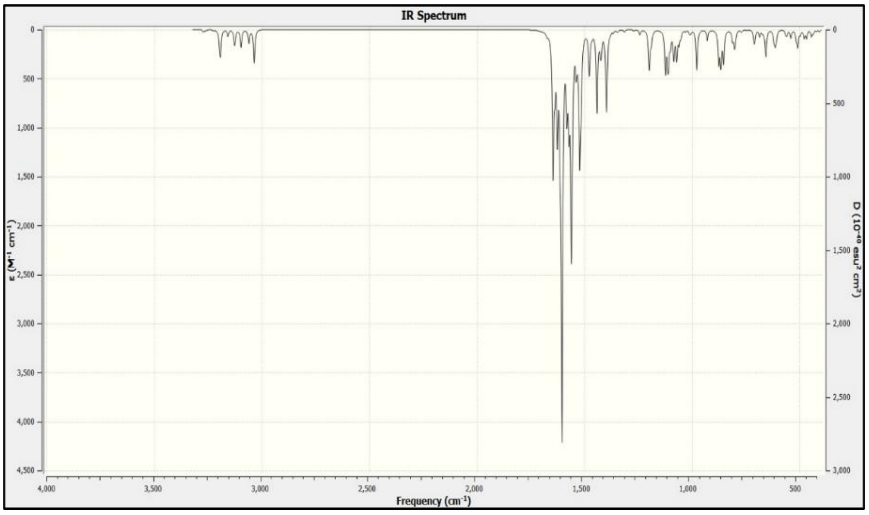

Fig.3b.16. FTIR spectrum of complex-3 through DFT computational analysis

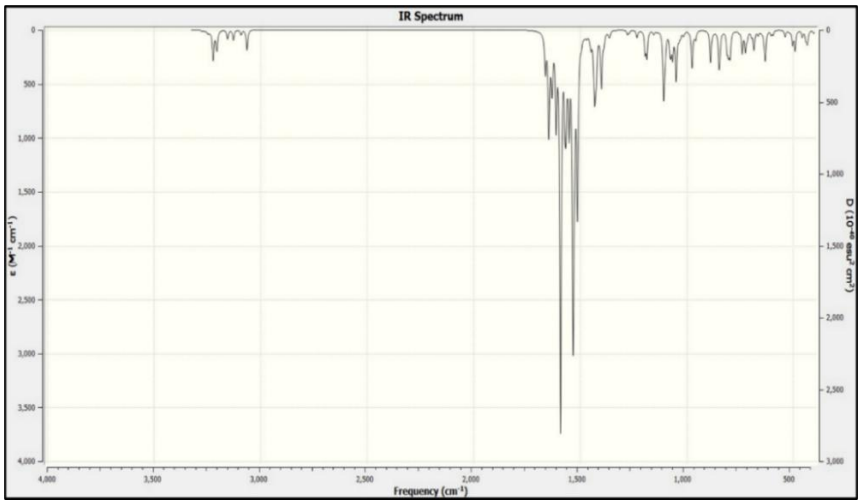

Fig.3b.17. FTIR spectrum of complex-4 through DFT computational analysis

Table 3b.12. Comparison of theoretical and practical FTIR vibrational data of complex-3 and complex-4

IR Frequencies (cm^{-1})	Complex-3		Complex-4	
	TH	PR	TH	PR
ν(C=O) of benzoyl chloride	1590	1577	1595	1586
ν(C=O) of Pyrazolone	1630	1602	1620	1601
Cyclic ν(C=N)	1450	1435	1480	1475
C–H in-plane deformation	1385	1379	1370	1360
ν_{M-O}	510	508	515	490

3b.3.5.1 Natural bond orbital (NBO) analysis

The delocalization of electron density, which is related to a stabilizing donor-acceptor interaction between occupied Lewis-type NBOs (donor) and unoccupied non-Lewis-type NBOs (acceptor/Rydberg), can be measured through NBO analysis. The related complexes'

natural bond orbital (NBO) analysis was performed using the B3LYP method with the LANL2DZ basis set. All interactions between the Cu(II) ion and the donor atom are considered to involve coordination bonds with oxygen atoms. This interaction results in a transfer of electron density from the lone pair (LP) of the oxygen atom in the acylpyrazolone ligand to the antibonding orbital LP*(Cu). The natural atomic charges on Cu^{2+} are 1.0782 and 1.1254 in complex-**3** and complex-**4**, respectively. Copper metal exhibits a natural electronic configuration of [core] 3d (9.29) 4s (0.25) 4p (0.37) in complex-**3** and [core] 3d (9.31) 4s (0.28) 4p (0.39) in complex-**4**. The number of electrons in the core is 17.9955, and the valence electron count is 9.9161 [42][23]. All the findings from DFT computational analysis ultimately support the square pyramidal geometry of both the synthesized copper acylpyrazolone complexes.

3b.3.6 Hirshfeld surface area analysis & 2D fingerprint plots

Hirshfeld surfaces are named after F.L. Hirshfeld, who developed the 'stockholder partitioning' method for determining atomic contributions within molecules, which influenced the characterization of molecules in a crystalline environment. Hirshfeld surface analysis serves as a crucial tool for investigating interactions in crystal structures by analyzing the electron density around a molecule [43][44]. CrystalExplorer17.5 software was used to carry out the Hirshfeld surface analysis and create the 2D fingerprint plots of the molecules to illustrate the structural relationships of the crystal structures in this group of closely related compounds [45]. Plotting the Hirshfeld surface (HS) using several characteristics, such as normalised distances (dnorm), de, di, shape index, curvedness, fragment patch etc., gives an idea about the interaction and hydrogen bonding. In hirshfeld surface analysis, the colours on various surfaces denote distinct types of intermolecular interactions and their characteristics. By defining different colours for short and long contacts, the HS displayed over dnorm enables the investigation of H-bonding interactions. The de and di represent the separation between the Hirshfeld surface and the closest external/internal atom. Short contacts exemplify the interactions involving H-bonds.

Red and blue patches, respectively, denote the short and long interactions on the HS [46]. A red patch on the HS of both complexes suggests that these atoms participate in H-bonding interactions. Intermolecular interactions that are shorter or longer than the van der Waals radius have a negative or positive value for dnorm, accordingly. By plotting the HS over the shape index and curvedness π···π, stacking interactions can be observed, which improve the crystal's stability [47]. An absence of red spots designates the absence of H-

bonds. The computed molecular moieties can be seen through the transparent surfaces. The fragment patches show the appropriate approach for identifying compounds' nearest neighbouring coordination environment. A more detailed explanation of all the surfaces has been given in Chapter **3a**. Using 2D fingerprint plots, non-covalent interactions that contribute to the stability of crystal packing can be quantitatively analyzed. In a fingerprint plot, the colour gradient typically reflects the density of interaction points. Cooler colours, such as blue and grey, indicate regions with weaker or less frequent interactions. The molecular hirshfeld surfaces and 2D fingerprint plots of complex-**3** and complex-**4** are demonstrated in **Figs.3b.18-3b.19,** respectively.

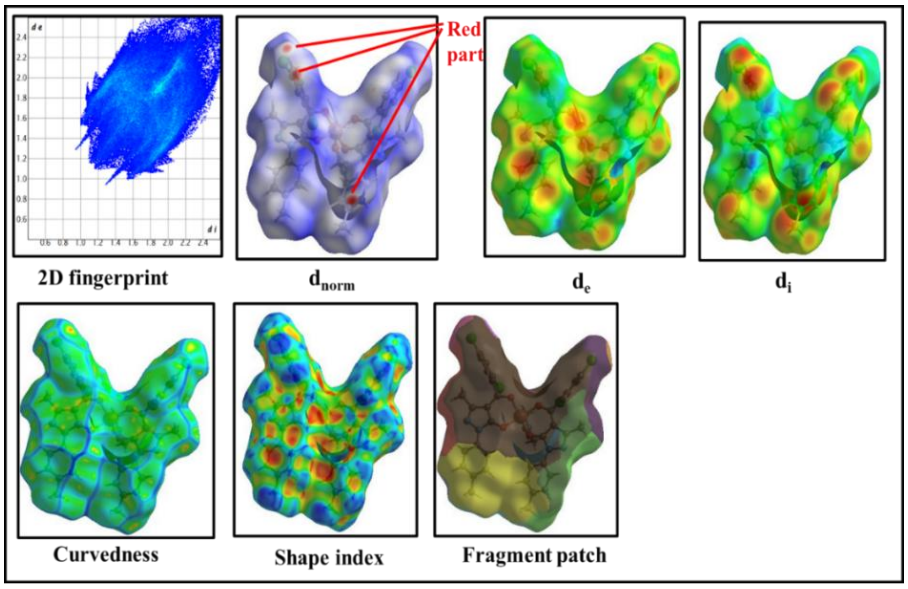

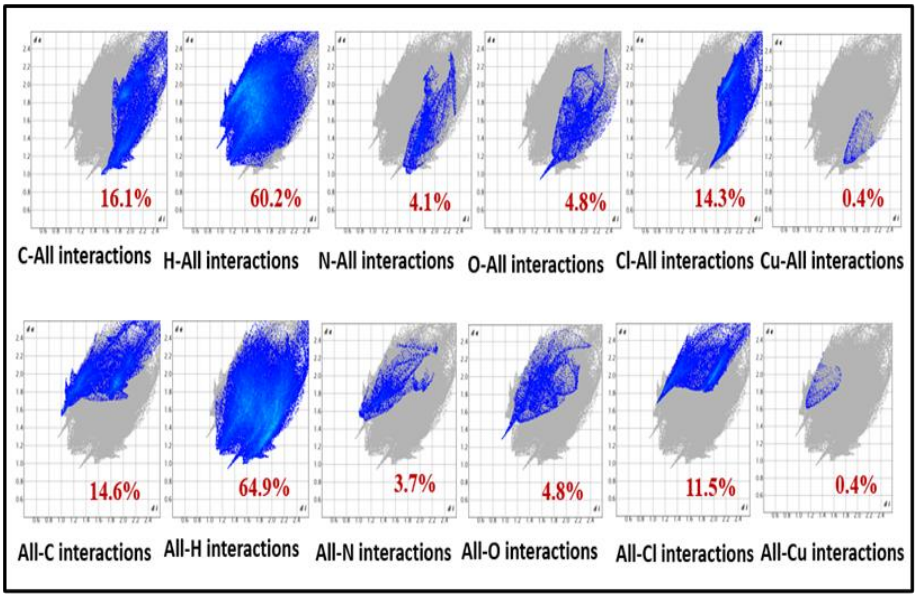

Fig.3b.18. Complex-3: The molecular Hirshfield (full fP diagram, dnorm, di, de, curvedness, shape index and fragment patch) and two-dimensional fingerprint plots

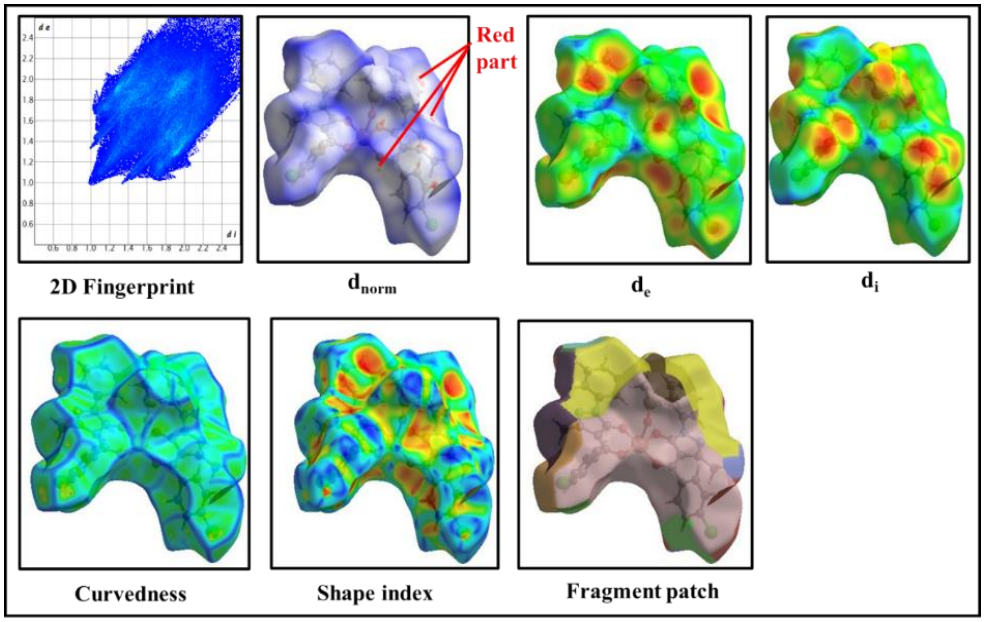

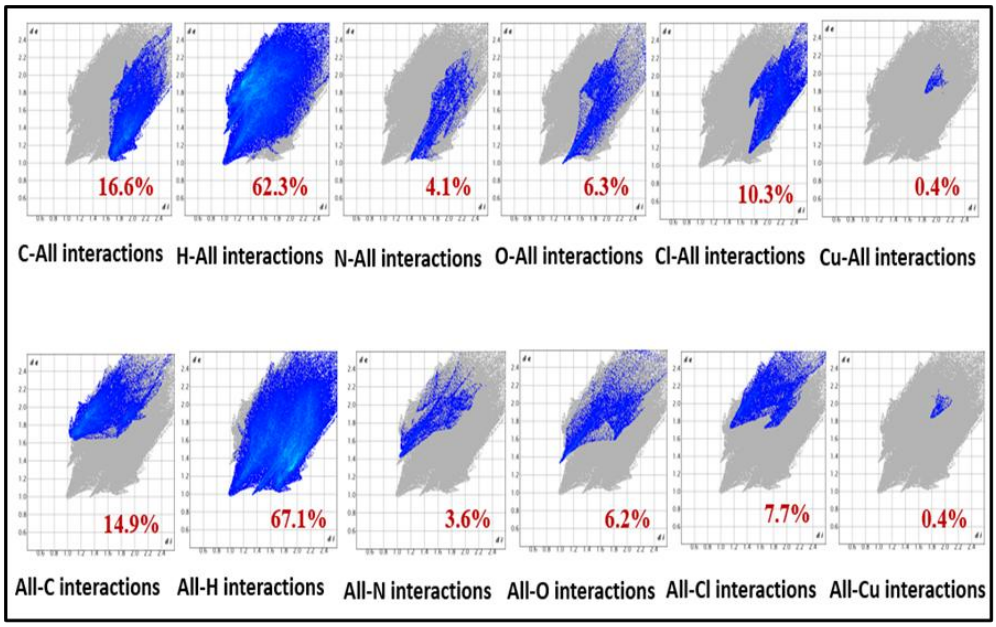

Fig.3b.19. Complex-4: The molecular Hirshfield (full fP diagram, dnorm, di, de, curvedness, shape index and fragment patch) and two-dimensional fingerprint plots

The packing efficiency of the compound can be evaluated by calculating the interaction percentages between all atoms and specific atom types. This method offers a deeper understanding of how atoms interact with their surrounding environment. “All-to-atom" interactions explain how the entire molecular environment affects a specific atom, whereas “atom-to-all" interactions describe the contribution of an individual atom within a molecule to the interactions with the surrounding crystal lattice. Both complexes have negligible or no interaction between Cu-All and All-Cu. This suggests that copper metal has no secondary interaction with other atoms surrounding it. The graphical presentation of the percentage interaction of atoms is presented in **Fig.3b.20.** No interaction between S-All

or all-S was observed in complex-**4**. Considerable H interaction could be observed in both complexes. 60% in complex-**3** and 62% in complex-**4.**

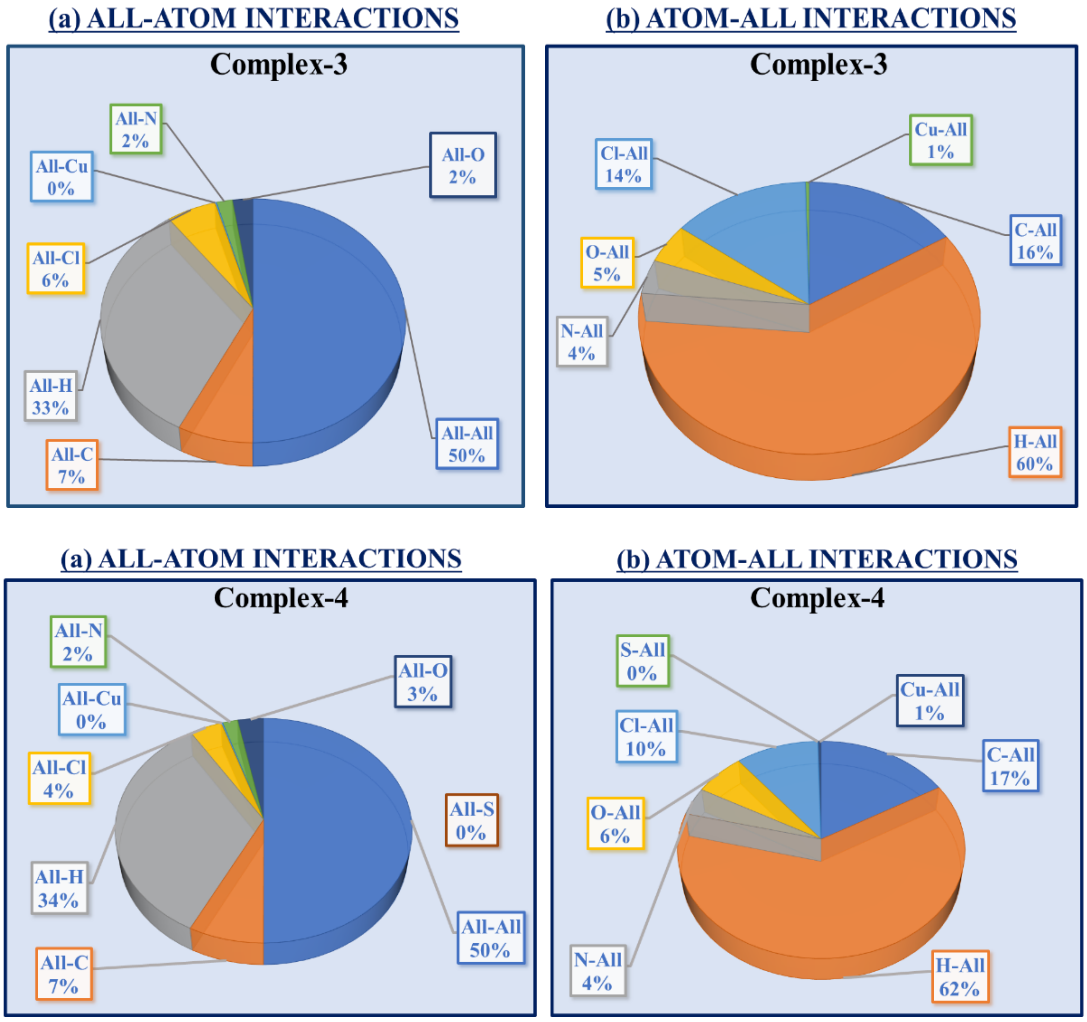

Fig.3b.20. Graphical presentation of percentage interactions between each inside and outside atoms of complex-3 and complex-4, respectively

3b.3.7 ESR analysis (magnetic behaviour)

ESR spectral analysis is a method utilized to explore the electronic structures of paramagnetic species by identifying unpaired electrons. This technique yields critical insights into these species' chemical environments and dynamics, aiding in understanding their magnetic properties and coordination geometries [48]. To explain the magnetic behaviour of the copper complexes, ESR analysis was performed using Tetracyanoethylene (TCNE) as a marker (g = 2.00277). The analysis was conducted with a JEOL spectrometer in the powder state at room temperature (RT) and in the solution state at low temperature (LNT). The graph displays four lines representing Cu(II). The graph displays four lines representing Cu(II) in the compound. The $g_{\parallel}$ value at RT is 2.545, while at LNT, it is 2.353

for complex-**3**. For complex-**4**, the $g_{\|}$ values are 2.281 at RT and 2.389 at LNT. The $g_{\perp}$ values are 2.083 for complex-**3** and 2.000 for complex-**4**, respectively. The g tensor values indicate that $g_{\|} > g_{\perp}$, which suggests the presence of an unpaired electron in the dx^2-y^2 orbital [34]. This finding implies that the ground state results from the dx^2-y^2 orbital, indicating that both complexes are axially symmetrical with a square pyramidal geometry. An average value is calculated using $|g|^a = 1/3\ (g_{\|}+2g_{\perp})$ and $|A|^a = 1/3\ (A_{\|}+2A_{\perp})$ [49]. All the ESR spectral data for both complexes are summarized in **Table 3b.13.** The ESR spectra of complex-**3** in solid and solution states are depicted in **Fig.3b.21.** The ESR spectra of complex-**4** in solid and solution states are depicted in **Fig.3b.22.**

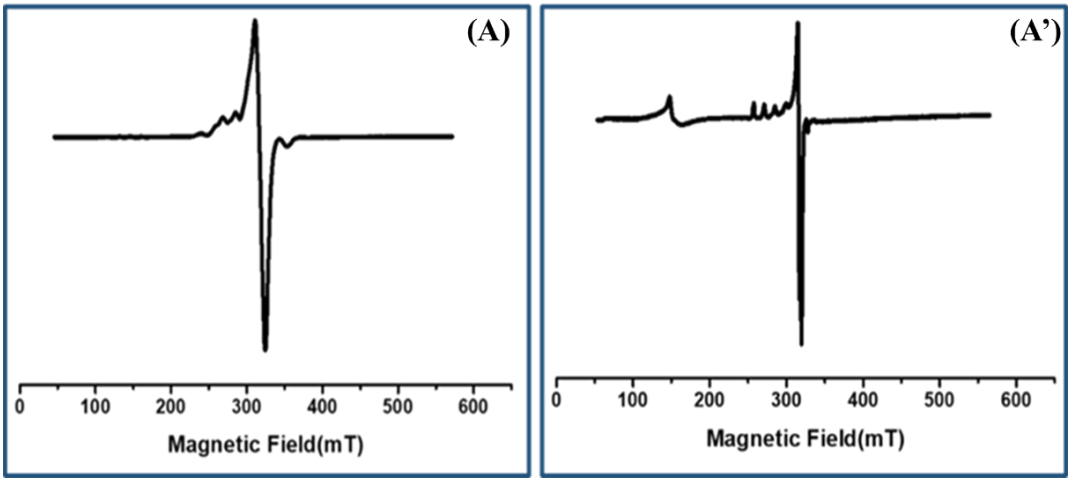

Fig.3b.21. Complex-3: X-band ESR spectra in (A) solid state at RT (A') solution state at LNT

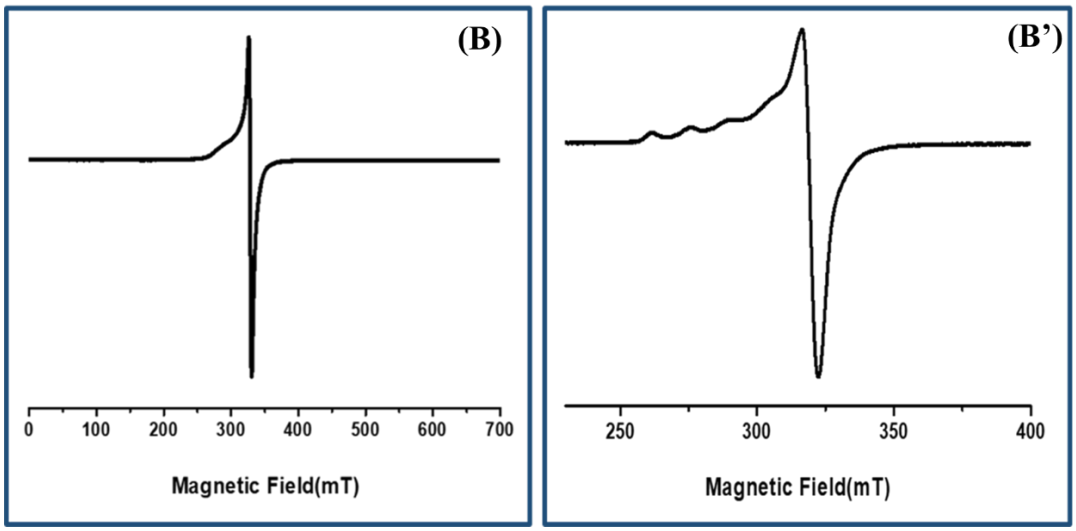

Fig.3b.22. Complex-4: X-band ESR spectra in (B) solid state at RT (B') solution state at LNT

Table 3b.13. ESR spectral data of complex-3 and complex-4

Complex-3			Complex-4		
	RT	LNT		RT	LNT
$g_{\|\|}$	2.545	2.353	$g_{\|\|}$	2.281	2.389
$g_{\perp}$	2.083	2.06	$g_{\perp}$	2.000	2.052
$\|g\|^a$	2.237	4.413	$\|g\|^a$	2.093	2.164
$A_{\|\|}$ (10^{-4} cm^{-1})	-	154	$A_{\|\|}$ (10^{-4} cm^{-1})	-	156
$A_{\perp}$ (10^{-4} cm^{-1})	-	29	$A_{\perp}$ (10^{-4} cm^{-1})	-	57
$\|A\|^a$ (10^{-4} cm^{-1})	-	106	$\|A\|^a$ (10^{-4} cm^{-1})	-	90

3b.3.8 *In vitro* anticancer activity

3b.3.8.1 MTT assay

Both copper complexes were evaluated against three cancer cell lines: NCI-H23, SH-SY5Y, and HepG2. The inhibition concentration 50 (IC_{50}) values were determined for each. Analysis of the IC_{50} values revealed that complex-**3** exhibited greater anticancer efficacy across all three cancer cell lines, while complex-**4** was more effective against SH-SY5Y cells. To further demonstrate the superior performance of complex-**3**, we conducted both a live/dead assay and a scratch (wound healing) assay using complex-**3** on the NCI-H23 cell line. Cisplatin was also evaluated against the SH-SY5Y cells alongside complex-**4** and against NCI-H23 cells treated with complex-**3**. After 24 hours of exposure, the compounds investigated showed significant cytotoxic effects [34]. Cisplatin was taken as a reference compound for Comparison. The IC_{50} values of complex-**3**, complex-**4** and cisplatin are presented in **Table 3b.14.** Percent cell viability of HepG2 and SH-SY5Y cells exposed to indicated doses of complex-3 is provided in **Fig.3b.23.** The comparative effects of complex-**3** versus cisplatin on the NCI-H23 cell line are presented in **Fig.3b.24.** Additionally, **Fig.3b.25** depicts the comparison of % cell viability in SH-SY5Y cells exposed to complex-**4** and cisplatin. Cisplatin is a commonly used chemotherapy drug recognized for its efficacy against multiple types of cancer; however, it frequently causes severe side effects and can lead to resistance in some patients. In contrast, the synthesized compounds showed enhanced anticancer activity in vitro, suggesting it may be a more effective and safer alternative to cisplatin for cancer treatment. Both complexes exhibited significant cytotoxicity.

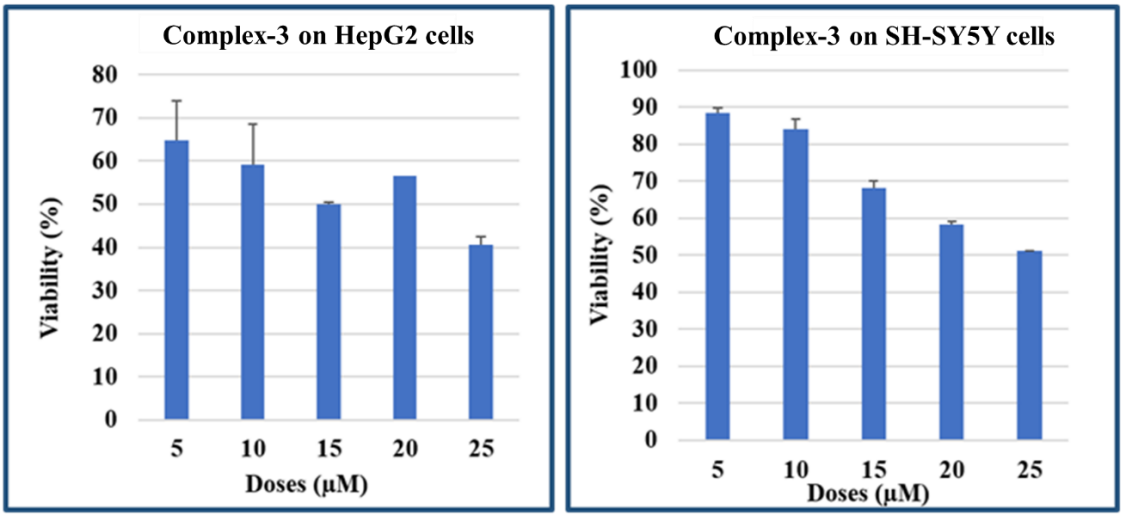

Fig.3b.23. Percent cell viability of HepG2 and SH-SY5Y cells exposed to indicated doses of complex-3

Table 3b.14. Percent inhibition (IC_{50} values) of complex-3 and complex-4 against NCI-H23, SH-SY5Y and HepG2 Cells

Percent inhibition (IC_{50} values)			
Compounds	**Complex-3**	**Complex-4**	**Cisplatin**
NCI-H23	4.8 µM	-	17.65 µM
SH-SY5Y	11.41 µM	10.8 µM	44.94 µM
HepG2	11.07 µM	-	-

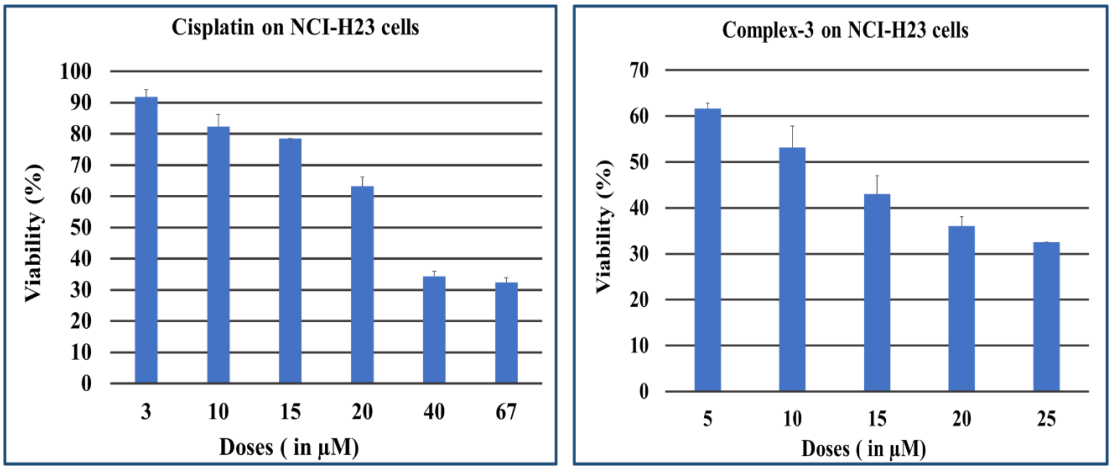

Fig.3b.24. A comparison of % cell viability of NCI-H23 cells exposed to an indicated dose of complex-3 and cisplatin

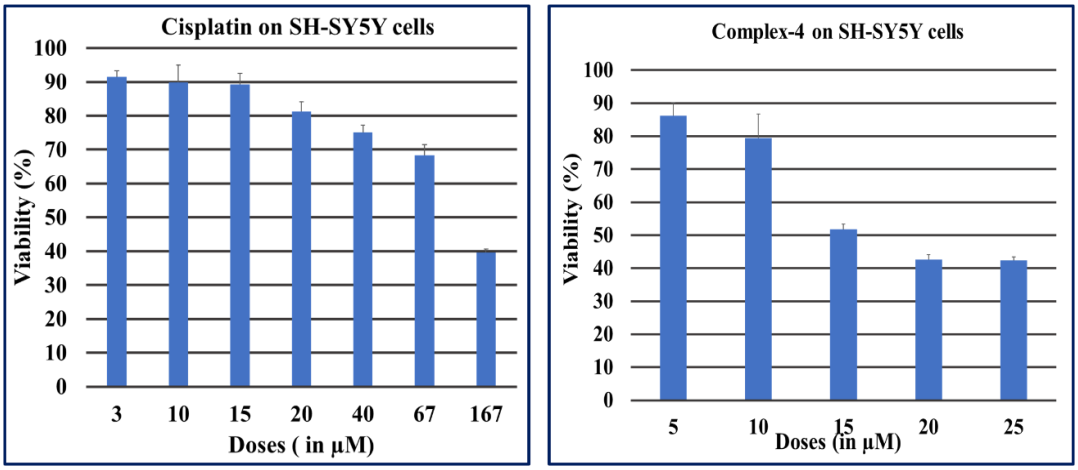

Fig.3b.25. A comparison of % cell viability of SH-SY5Y cells exposed to an indicated dose of complex-4 and cisplatin

3b.3.8.2 Live/Dead assay (Cell death analysis)

The live/dead assay was used to count both live and dead cells. Calcein dye produces green fluorescence, indicating living cells, while Ethidium homodimer-1 (EthD-1) generates red fluorescence, marking apoptotic and dead cells [28]. The prominent red fluorescence observed reflects significant cell death. While cell death occurred in the control media, treatment with the synthetic complex-**3** led to a noticeable increase in apoptotic cell death. The results demonstrate that complex-**3** is more effective against NCI-H23 cells [50]. Dual staining of NCI-H23 cells is shown in **Fig.3b.26,** and **Fig.3b.27** illustrates the percentage of dead NCI-H23 cells.

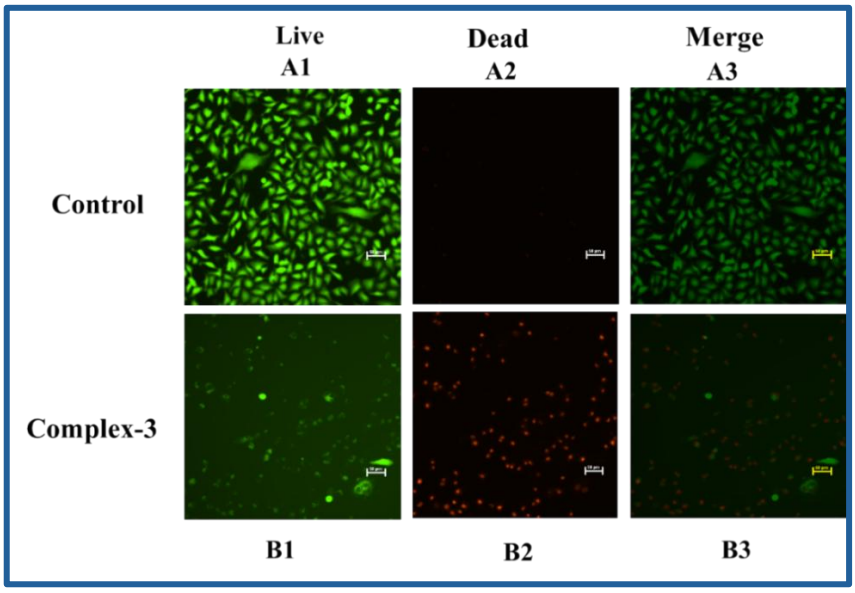

Fig.3b.26. Dual staining of NCI-H23 cells exposed to complex3 for 24h
(A1&A2) = Untreated cells stained by Calcein and EthD-1 dyes, respectively
(B1&B2) = Treated cells stained by Calcein and EthD-1 dyes, respectively

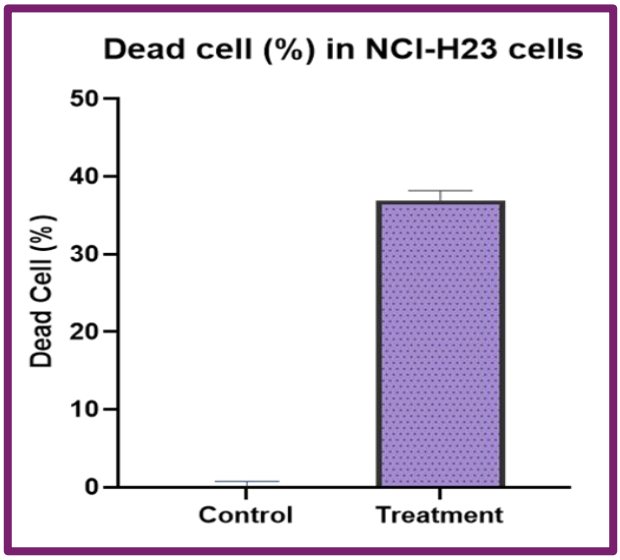

Fig.3b.27. Percentage of dead cells of NCI-H23 exposed to complex-3, calculated by ImageJ Analysis

3b.3.8.3 Scratch Assay

Wound closure is a useful technique to evaluate cell migration at different time intervals: 0 h, 24 h, and 48 h. After 24 h, treated cells showed 26% wound closure, compared to 41% in the control group. By 48 h, wound closure reached 75% in treated cells and 40% in the untreated group. These results indicate that the synthesized copper pyrazolone complex (complex-**3**) significantly inhibits the migratory ability of NCI-H23 lung cancer cells [29][51]. A detailed explanation of this analysis has been provided in chapter **3a**. Wound closure was analyzed using ImageJ software, with results depicted in **Fig.3b.28** and the percentage of closure shown in **Fig.3b.29.**

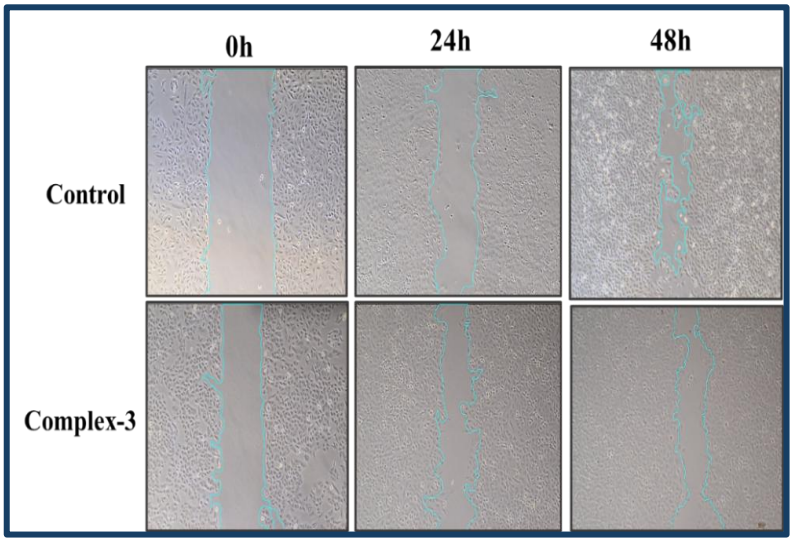

Fig.3b.28. Scratch assay of NCI-H23 cells exposed to complex-3 in the control and treated conditions at 0h, 24h and 48h

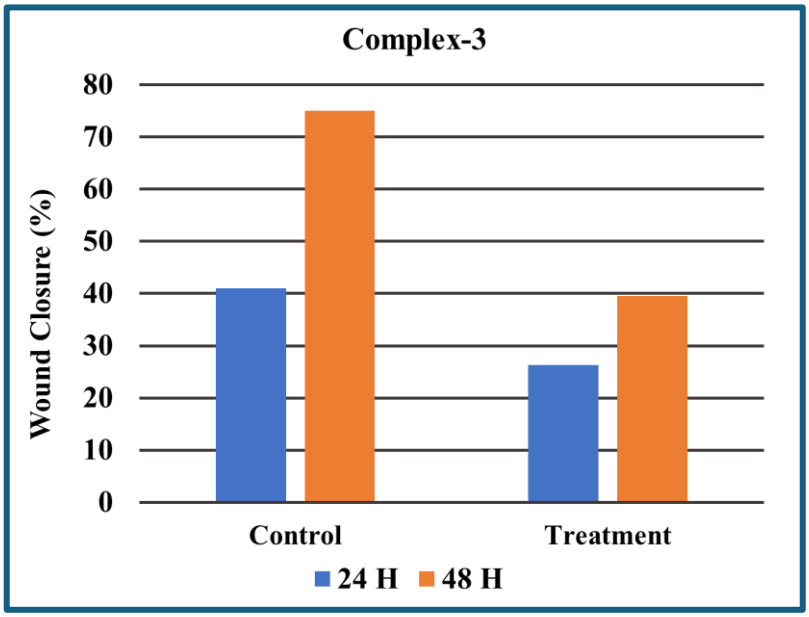

Fig.3b.29. Complex-3: Wound closer (%) of NCI-H23 cells in untreated and treated conditions at 24 h and 48 h, calculated by ImageJ software

3b.4 Conclusion

The design and synthesis of pyrazoles is a promising research topic since they are an important pharmacophore with diverse biological characteristics, and their derivatives are pharmacologically very strong. In this chapter, we discussed synthesising and characterising two square pyramidal Cu(II) complexes. Single-crystal X-ray diffraction confirmed the square-pyramidal geometry of both complexes. In complex-**3** and complex-**4**, four ligand oxygen atoms occupy equatorial positions, while DMF and DMSO oxygen atoms coordinate axially, respectively. The **τ** value (**0.15–0.3)** further supports the square-pyramidal geometry. Various analytical methods were employed for the characterization. The B3LYP/6-31G and B3LYP/LANL2DZ, two different basis sets, were used to optimize the geometry of both complexes. The HOMO-LUMO energy calculations were made using DFT analysis. The practical and theoretical bond lengths and angles match each other well. The ESR analysis was done to check the paramagnetic behaviour of both complexes. Hirshfeld surface analysis was employed for intermolecular interactions. *In vitro,* anticancer activity indicates the positive application of both complexes. A **complex-3** effectively inhibits cell viability and lung adenocarcinoma (NCI-H23) cell migration. We found that the compound can inhibit lung cancer cells' ability to survive and spread.

References

[1] R.K. Sodhi, Metal Complexes in Medicine: An Overview and Update from Drug Design Perspective, Cancer Ther. Oncol. Int. J. 14 (2019). https://doi.org/10.19080/ctoij.2019.14.555883.

[2] Y. Zhang, L.C. Feng, X.X. Li, W.K. Dong, Synthesis, Crystal Structure, and Theoretical Calculations of a μ-Dichloro-Bridged Tetranuclear Cu(II) Bis(salamo)-Type Complex, Russ. J. Gen. Chem. 93 (2023) 1486–1497. https://doi.org/10.1134/S107036322306021X.

[3] S. Abdolmaleki, M. Ghadermazi, A. Aliabadi, Study on electrochemical behavior and in vitro anticancer effect of Co(II) and Zn(II) complexes containing pyridine-2,6-dicarboxylate, Inorganica Chim. Acta. 527 (2021) 120549. https://doi.org/10.1016/j.ica.2021.120549.

[4] S. Kumar, B. Bag, D. Kumar, V. Gramlich, Y. Li, Synthesis and Characterization of Copper (II) and Zinc (II) Complexes Containing 1-Phenyl-3-methyl-4-benzoyl-5-pyrazolone, (2003) 1009–1014.

[5] E.D. Ilieva, G.P. Petrova, R.D. Nikolova, G.N. Vayssilov, Computational elucidation of the reaction mechanism for synthesis of pyrrolidinedione derivatives: Via Nef-Type rearrangement-cyclization reaction, RSC Adv. 8 (2018) 3178–3188. https://doi.org/10.1039/c7ra11908a.

[6] Ikechukwu P. Ejidik, Cu (II) Complexes of, (2018) 1–18. https://doi.org/10.3390/molecules23071581.

[7] K. Karrouchi, S. Radi, Y.R. Id, J. Taoufik, Synthesis and Pharmacological Activities of Pyrazole Derivatives : A Review, n.d. https://doi.org/10.3390/molecules23010134.

[8] F. Marchetti, C. Pettinari, C. Di Nicola, A. Tombesi, R. Pettinari, Coordination chemistry of pyrazolone-based ligands and applications of their metal complexes, Coord. Chem. Rev. 401 (2019) 213069. https://doi.org/10.1016/j.ccr.2019.213069.

[9] F. Marchetti, R. Pettinari, C. Di Nicola, C. Pettinari, J. Palmucci, R. Scopelliti, T. Riedel, B. Therrien, A. Galindo, P.J. Dyson, Synthesis, characterization and cytotoxicity of arene-ruthenium(II) complexes with acylpyrazolones functionalized with aromatic groups in the acyl moiety, Dalt. Trans. 47 (2018) 868–878. https://doi.org/10.1039/c7dt04249c.

[10] F. Marchetti, R. Pettinari, C. Pettinari, Recent advances in acylpyrazolone metal complexes and their potential applications, Coord. Chem. Rev. 303 (2015) 1–31. https://doi.org/10.1016/j.ccr.2015.05.003.

[11] K. Jana, T. Maity, T.S. Mahapatra, P.K. Das Mohapatra, S.C. Debnath, S. Das, M. Hossain, B.C. Samanta, A square pyramidal copper(II) complex of a Schiff base ligand: synthesis, crystal structure, antibacterial and DNA interaction studies, Transit. Met. Chem. 42 (2017) 69–78. https://doi.org/10.1007/s11243-016-0108-6.

[12] K.M. Vyas, R.N. Jadeja, D. Patel, R. V. Devkar, V.K. Gupta, A new pyrazolone based ternary Cu(II) complex: Synthesis, characterization, crystal structure, DNA binding, protein binding and anti-cancer activity towards A549 human lung carcinoma cells with a minimum cytotoxicity to non-cancerous cells, Polyhedron. 65 (2013) 262–274. https://doi.org/10.1016/j.poly.2013.08.051.

[13] K.M. Vyas, R.N. Jadeja, D. Patel, R. V. Devkar, V.K. Gupta, Effect of ligand substitution in pyrazolone based binary and ternary Cu(II) complexes on DNA binding, protein binding and anti-cancer activity on A549 lung carcinoma cell lines, Polyhedron. 80 (2014) 20–33. https://doi.org/10.1016/j.poly.2013.12.037.

[14] I.U. Shaikh, Synthesis , Characterization and Studies on d^{10} Metal Complexes derived from Acyl Pyrazolones, (2020).

[15] G.M. Sheldrick, SHELXT - Integrated space-group and crystal-structure determination, Acta Crystallogr. Sect. A Found. Crystallogr. 71 (2015) 3–8. https://doi.org/10.1107/S2053273314026370.

[16] G.M. Sheldrick, Crystal structure refinement with SHELXL, Acta Crystallogr. Sect. C Struct. Chem. 71 (2015) 3–8. https://doi.org/10.1107/S2053229614024218.

[17] O. V. Dolomanov, L.J. Bourhis, R.J. Gildea, J.A.K. Howard, H. Puschmann, OLEX2: A complete structure solution, refinement and analysis program, J. Appl. Crystallogr. 42 (2009) 339–341. https://doi.org/10.1107/S0021889808042726.

[18] C.F. Macrae, P.R. Edgington, P. McCabe, E. Pidcock, G.P. Shields, R. Taylor, M. Towler, J. Van De Streek, Mercury: Visualization and analysis of crystal structures, J. Appl. Crystallogr. 39 (2006) 453–457. https://doi.org/10.1107/S002188980600731X.

[19] P.J. Hay, W.R. Wadt, Ab initio effective core potentials for molecular calculations. Potentials for the transition metal atoms Sc to Hg, J. Chem. Phys. 82 (1985) 270–283. https://doi.org/10.1063/1.448799.

[20] S. Chiodo, N. Russo, E. Sicilia, LANL2DZ basis sets recontracted in the framework of density functional theory, J. Chem. Phys. 125 (2006). https://doi.org/10.1063/1.2345197.

[21] L. Chen, T. Liu, J.-Z. Chen, A density functional theory study on the electronic structures and properties of methylenediaminetetraacetate complexes (M=Co, Ni, Cu, Zn, Cd), Acta Chim. Sin. 66 (2008) 1187–1195.

[22] S. Lehtola, I observed researchers are using different basis set to optimize and calculate HOMO-LUMO of organometallics. Which one is appropiate?, (2018).

[23] J.M.M. and R.C.M. PRADEEP KUMAR VISHWAKARMA, Pyrone-based Cu (II) complexes , their characterization , DFT based conformational drift from square planar to square pyramidal geometry, 128 (2016) 511–522. https://doi.org/10.1007/s12039-016-1048-6.

[24] A.K. Patel, R.N. Jadeja, H. Roy, R.N. Patel, S.K. Patel, R.J. Butcher, Pseudo-tetrahedral copper(II) complex derived from N'-[(2E,3Z)-4-hydroxy-4-phenylbut-3-en-2-ylidene]acetohydrazide: Synthesis, molecular structure, quantum chemical investigations, antioxidant and antiproliferative properties, J. Mol. Struct. 1185 (2019) 341–350. https://doi.org/10.1016/j.molstruc.2019.03.004.

[25] A.K. Patel, R.N. Jadeja, H. Roy, R.N. Patel, S.K. Patel, R.J. Butcher, M. Cortijo, S. Herrero, Copper(II) hydrazone complexes with different nuclearities and geometries: Synthesis, structural characterization, antioxidant SOD activity and antiproliferative properties, Polyhedron. 186 (2020) 114624. https://doi.org/10.1016/j.poly.2020.114624.

[26] T. Mosmann, Rapid Colorimetric Assay for Cellular Growth and Survival: Application to Proliferation and Cytotoxicity Assays, RSC Adv. 65 (1983) 55–63. https://doi.org/10.1039/c6ra17788c.

[27] K.M. Vyas, R. V. Devkar, A. Prajapati, R.N. Jadeja, Pyrazolone incorporating bipyridyl metallointercalators as effective DNA, protein and lung cancer targets: Synthesis, characterization and in vitro biocidal evaluation, Chem. Biol. Interact. 240 (2015) 250–266. https://doi.org/10.1016/j.cbi.2015.08.022.

[28] C. Hu, S. He, Y.J. Lee, Y. He, E.M. Kong, H. Li, M.A. Anastasio, G. Popescu, Live-dead assay on unlabeled cells using phase imaging with computational specificity, Nat. Commun. 13 (2022). https://doi.org/10.1038/s41467-022-28214-x.

[29] A.V.P. Bobadilla, J. Arévalo, E. Sarró, H.M. Byrne, P.K. Maini, T. Carraro, S. Balocco, A. Meseguer, T. Alarcón, In vitro cell migration quantification method for scratch assays, J. R. Soc. Interface. 16 (2019). https://doi.org/10.1098/rsif.2018.0709.

[30] R.N. Jadeja, K.M. Vyas, V.K. Gupta, R.G. Joshi, C. Ratna Prabha, Syntheses, characterization and molecular structures of calcium(II) and copper(II) complexes bearing O2-chelate ligands: DNA binding, DNA cleavage and anti-microbial study, Polyhedron. 31 (2012) 767–778. https://doi.org/10.1016/j.poly.2011.11.004.

[31] S. Parihar, S. Pathan, R.N. Jadeja, A. Patel, V.K. Gupta, Synthesis and Crystal Structure of an Oxovanadium(IV) Complex with a Pyrazolone Ligand and Its Use as a Heterogeneous Catalyst for the Oxidation of Styrene under Mild Conditions, Inorg. Chem. 51 (2012) 1152–1161. https://doi.org/10.1021/ic202396q.

[32] W. Maalej, P. Guionneau, Z. Elaoud, A new square pyramidal copper(II) complex [Cu(C10H24N4)Br]Br: Crystal structure, thermal analysis, Hirschfeld surfaces, electrical and semiconducting properties, J. Mol. Struct. 1241 (2021) 130630. https://doi.org/10.1016/j.molstruc.2021.130630.

[33] DR. S. VALARSELVAN, Electronic Spectra of Transition metal complexes Spectroscopic ground states , spectral terms , R-S coupling and J-J couplings- term symbol – selection rules — microstates — Pigeon hole diagram for p2 and d2 configuration . Orgel and Tanabe – sugano diagr, n.d.

[34] S. Roy, P. Mitra, A.K. Patra, Cu(II) complexes with square pyramidal (N2S)CuCl2 chromophore: Jahn-Teller distortion and subsequent effect on spectral and structural properties, Inorganica Chim. Acta. 370 (2011) 247–253. https://doi.org/10.1016/j.ica.2011.01.068.

[35] L. Tong, L.-L. Gan, H.-W. Zhang, Y.-X. Sun, H.-Y. Niu, W.-K. Dong, Synthesis, structure, theoretical studies, and properties of dinuclear Cu(II) and novel trinuclear Co(II) complexes with a more flexible 3-MeOsalamo-like ligand, J. Mol. Struct. 1294 (2023) 136465. https://doi.org/10.1016/j.molstruc.2023.136465.

[36] S.J. Munshi, M. Guin, S. Kundu, S.B. Kumar, Synthesis, structures and Hirshfeld surface analysis of Ni(II) and Co(III) complexes with N2O donor Schiff base ligand, J. Indian Chem. Soc. 98 (2021) 100080. https://doi.org/10.1016/j.jics.2021.100080.

[37] E. Aljuhani, M.M. Aljohani, A. Alsoliemy, R. Shah, H.M. Abumelha, F.A. Saad, A. Hossan, Z.A. Al-Ahmed, A. Alharbi, N.M. El-Metwaly, Synthesis and characterization of Cu(II)-pyrazole complexes for possible anticancer agents; conformational studies as well as compatible in-silico and in-vitro assays, Heliyon. 7 (2021) e08485. https://doi.org/10.1016/j.heliyon.2021.e08485.

[38] D. Shoba, S. Periandy, M. Karabacak, S. Ramalingam, Vibrational spectroscopy (FT-IR and FT-Raman) investigation, and hybrid computational (HF and DFT) analysis on the structure of 2,3-naphthalenediol, Spectrochim. Acta - Part A Mol. Biomol. Spectrosc. 83 (2011) 540–552. https://doi.org/10.1016/j.saa.2011.09.002.

[39] C. Ravi, S. Kumar, Approach of Density Functional Theory to Molecules Using Gaussian, Int. J. Pure Appl. Phys. 15 (2019) 1–13. http://www.ripublication.com.

[40] D. Karaka, K. Sayin, DFT and TD-DFT studies on copper (II) complexes with tripodal tetramine ligands, 52 (2013) 480–485.

[41] O. V Gritsenko, Koopmans’ theorem and its density-functional-theory analog assessed in evaluation of the red shift of vertical ionization potential upon complexation, Chem. Phys. Lett. (2017). https://doi.org/10.1016/j.cplett.2017.11.019.

[42] M. Sithambaresan, M.R.P. Kurup, G. Serdaroğlu, S. Kaya, Copper(II) chelates derived from an N,N,O-tridentate 2-pyridinecarboxaldehyde-N4-phenylsemicarbazone: Synthesis, spectral aspects, crystal structure, FMO and NBO analysis, J. Mol. Struct. 12[1] M. S (2023) 134866. https://doi.org/10.1016/j.molstruc.2022.134866.

[43] M.A. Spackman, D. Jayatilaka, Hirshfeld surface analysis, CrystEngComm. 11 (2009) 19–32. https://doi.org/10.1039/b818330a.

[44] P.R. Spackman, M.J. Turner, J.J. McKinnon, S.K. Wolff, D.J. Grimwood, D. Jayatilaka, M.A. Spackman, CrystalExplorer: A program for Hirshfeld surface analysis, visualization and quantitative analysis of molecular crystals, J. Appl. Crystallogr. 54 (2021) 1006–1011. https://doi.org/10.1107/S1600576721002910.

[45] M. Zarif, M. Zubir, N.S. Jamaludin, S. Nadiah, A. Halim, Hirshfeld surface analysis of some new heteroleptic Copper (I) complexes, J. Mol. Struct. 1193 (2019) 141–150. https://doi.org/10.1016/j.molstruc.2019.05.011.

[46] S.S. Hasanova, E.A. Yolchueva, A.Q. Mashadi, S. Muhammad, M. Ashfaq, M.E. Muhammed, K.S. Munawar, M.N. Tahir, A.G. Al-sehemi, S.S. Alarfaji, Synthesis , Characterization , Crystal Structures , and Supramolecular Assembly of Copper Complexes Derived from Nitroterephthalic Acid along with Hirshfeld Surface Analysis and Quantum Chemical Studies, (2023). https://doi.org/10.1021/acsomega.2c07686.

[47] Y.X. Wei, S.Z. Li, Y. Huang, L. Wang, W.K. Dong, Synthesis, structures, and computational studies of methoxydisubstituted bis(salamo)-type homopolynuclear Cu(II) and Co(II) complexes, J. Coord. Chem. 76 (2023) 1157–1172. https://doi.org/10.1080/00958972.2023.2229482.

[48] M. Kohno, Applications of electron spin resonance spectrometry for reactive oxygen species and reactive nitrogen species research, J. Clin. Biochem. Nutr. 47 (2010) 1–11. https://doi.org/10.3164/jcbn.10-13R.

[49] M. Valko, P. Pelikan, S. Biskupic, M. Mazur, ESR spectra of copper(II) complexes in the solids, Chem. Pap. 44 (1990) 805–813. https://www.chemicalpapers.com/file_access.php?file=446a805.pdf.

[50] P.N. Tawakoli, A. Al-Ahmad, W. Hoth-Hannig, M. Hannig, C. Hannig, Comparison of different live/dead stainings for detection and quantification of adherent microorganisms in the initial oral biofilm, Clin. Oral Investig. 17 (2013) 841–850. https://doi.org/10.1007/s00784-012-0792-3.

[51] X. Wang, C.C. Decker, L. Zechner, S. Krstin, M. Wink, In vitro wound healing of tumor cells: Inhibition of cell migration by selected cytotoxic alkaloids, BMC Pharmacol. Toxicol. 20 (2019) 1–12. https://doi.org/10.1186/s40360-018-0284-4.

Published Paper

Inorganica Chimica Acta 559 (2024) 121794

Contents lists available at ScienceDirect

Inorganica Chimica Acta

journal homepage: www.elsevier.com/locate/ica

Acylpyrazolone based Square pyramidal Cu(II) complexes: Synthesis, Structural characterization, DFT and antiproliferative properties

Sapna Barad [a], Kaushalkumar Chaudhari [b], H. Roy [b], Ray J. Butcher [c], R.N. Jadeja [a,*]

[a] Department of Chemistry, Faculty of Science, The Maharaja Sayajirao University of Baroda, Vadodara 390002, India
[b] Department of Zoology, Faculty of Science, The Maharaja Sayajirao University of Baroda, Vadodara 390002, India
[c] Department of Inorganic & Structural Chemistry, Howard University, Washington, DC 22031, USA

ARTICLE INFO

Keywords:
Acylpyrazolone ligand
Live-dead assay
Square Pyramidal Copper complex Wound healing assay

ABSTRACT

σ-donating acylpyarazolone HL^b ligand and its Copper complex $[Cu(HL^b)_2(DMF)]$ were synthesized. $[Cu(HL^a)_2(DMSO)]$ complex is synthesized from the previously reported HL^a ligand. Single crystal analysis revealed the Square Pyramidal geometry of both the complexes with one oxygen from DMF and DMSO attached at an apical site in the $[Cu(HL^b)_2(DMF)]$ and $[Cu(HL^a)_2(DMSO)]$ complexes, respectively and four oxygens of the ligand coordinated to the central copper metal at an equatorial position. The electronic spectra of both the complexes have been analyzed using UV–visible spectroscopy. The study investigated the molecular specification utilising the B3LYP/6-31G and B3LYP/LANL2DZ basis set formalism for DFT computational analysis to provide a perfect correlation and comparison with all the experimental values. The Hirshfeld surface area analysis was done to investigate the intermolecular interactions or secondary molecular interaction. The magnetic behaviour of both the synthesized complexes was identified by ESR spectral analysis. Using three different cancer cell lines NCI-H23 (Lung adenocarcinoma cells), HepG2 (Hepatocellular carcinoma) and SH-SY5Y (Neuroblastoma cells), cytotoxicity of both the copper complexes was examined and wound healing assay on $[Cu(HL^b)_2(DMF)]$ complex was done to check the cell migration.

1. Introduction

The biological activities that are essential to life processes are linked to transition metals. In biology, metal ions are necessary for their function as drugs and as diagnostic tools. Transition metals, such as copper, iron, and manganese, among others, have structural and functional roles in numerous biological processes, including electron transfer, catalysis, and enzyme and protein active sites. Metal complexes can now be used as medicinal agents more effectively because of developments in inorganic chemistry [1]. Since the beginning, coordination chemistry has evolved for >300 years, establishing a vibrant new science. Its theory has also been consistently improved [2].

Inorganic substances have made a substantial contribution to the expansion and development of medical science, and subsequently human health [3]. Complexes containing copper(II) have attracted a lot of interest because of their exceptional biological and catalytic abilities. It has been noticed that copper(II) complexes are frequently more effective as anti-inflammatory medications than the parent ligands themselves [4,5]. In terms of biological and pharmacological applications, metal complexes with certain bioactive ligands can prove more efficient than those with those ligands in their free state [6]. Five-membered heterocycles known as pyrazoles are a type of molecule that are particularly helpful in the synthesis of organic compounds. They are one of the azole family's most explored categories of chemical substances. Numerous applications in industries including technology, health, and agriculture are made possible by various arrangements of the pyrazole nucleus. They are referred to precisely as antibacterial, antifungal, anticancer, antidepressant, anti-inflammatory, anti-tuberculosis, antioxidant, and antiviral drugs, as well as protein glycation inhibitors [7].

The advantages of pyrazolone based metal complexes, such as stability, ease of synthesis, ease of modification, and abundance of bioactivity, have attracted attention [8]. Because of their selectivity, flexibility in synthesis and numerous biological uses Schiff bases have been the subject of a wide range of studies. Numerous medicines and bioactive natural alkaloids contain pyrazolone scaffolds [9,10].

Abbreviations: DFT, density functional theory; MTT, 3-[4,5-dimethylthiazol-2-yl; −2–5, diphenyl tetrazolium bromide.

* Corresponding author.
E-mail address: rjadeja-chem@msubaroda.ac.in (R.N. Jadeja).

https://doi.org/10.1016/j.ica.2023.121794
Received 19 August 2023; Received in revised form 3 October 2023; Accepted 3 October 2023
Available online 5 October 2023